2005

ACCOMPLISHMENTS AND OPPORTUNITIES

NIST CENTER FOR NEUTRON RESEARCH

NIST SP 1045

NIST
National Institute of Standards and Technology
Technology Administration, U.S. Department of Commerce

The Double Crystal Analyzer Linkage (DXAL) is one of 20 being installed in the Multi-Axis Crystal Spectrometer (MACS). Visible are two curved panels holding pyrolytic graphite crystals and collimating blades between them. The design features a single mechanical linkage that allows rotation of each crystal panel by 2θ and each blade by θ while maintaining parallel entering and exiting beam paths.

2005 NIST Center for Neutron Research

ACCOMPLISHMENTS AND OPPORTUNITIES

NIST Special Publication 1045

Patrick D. Gallagher , Director

Ronald L. Cappelletti, Editor

September 2005

National Institute of Standards and Technology
William A. Jeffrey, Director

Technology Administration
Michelle O'Neill,
Acting Under Secretary of
Commerce for Technology

U.S. Department of Commerce
Carlos M. Gutierrez, Secretary

DISCLAIMER

Certain commercial entities, equipment, or materials may be identified in this document in order to describe an experimental procedure or concept adequately. Such identification is not intended to imply recommendation or endorsement by the National Institute of Standards and Technology, nor is it intended to imply that the entities, materials, or equipment are necessarily the best available for the purpose.

National Institute of Standards
and Technology Special Publication 1045

Natl. Inst. Stand. Technol. Spec. Publ. 1045, 72 pages
(September 2005)

CODEN: NSPUE2

U.S. GOVERNMENT PRINTING OFFICE - WASHINGTON: 2005

For sale by the Superintendent of Documents,
U.S. Government Printing Office

Internet: bookstore.gpo.gov ■ Phone: 202.512.1800
Fax: 202.512.2250 ■ Mail: Stop SSOP, Washington, DC 20402-0001

Table of Contents

Foreword

It is with pleasure that I share with you the record of accomplishments for the NIST Center for Neutron Research for this past year, which brought us major progress, significant changes, and new opportunities. The year began with the completion of a scheduled three-month shutdown to replace the cadmium control assemblies ("shim arms") for the reactor and to replace the heavy water in order to reduce the concentration of tritium in the reactor primary cooling circuit. Our staff took advantage of the outage to perform a large number of maintenance projects and upgrades to the reactor, the beam systems, and the instruments. In spite of the long list of tasks, all work was completed on time and the reactor and cold source performed flawlessly for the remainder of the year, during which it operated 197 full power days. This year has also seen enormous progress made on the installation of two major new instruments: a thermal triple-axis spectrometer located at BT-7 and a cold neutron multi-analyzer crystal spectrometer at NG-0. Both instruments are in the advanced stages of construction and will provide major advances in capability when completed.

The budget setback that so adversely affected the NCNR in 2004 was reversed in dramatic fashion with the passage of the 2005 budget. Not only was lost funding restored, but significant new funds were added to expand the user program and instrument development programs at the NCNR. The success of this budget initiative, originally proposed in 2002, was due to the strong and vocal support of the NCNR by its many users who lobbied and wrote to the Administration and to Congress. Their show of support is deeply gratifying and appreciated by all of us here at the NCNR. For our part, we are already working hard to develop new and improved instruments and to increase access to these instruments through a stronger user program.

This year saw the National Science Foundation renew critical funding for the Center for High Resolution Neutron Scattering, (CHRNS). This Center, which is one of the pillars of the NCNR scattering program, is a partnership between NIST and the NSF that was created to operate a suite of instruments through a robust national user program tailored to meet the needs of the U.S. academic research community.

In a major change for the NCNR organization, Jack Rush retired from the NCNR after 39 years at the National Bureau of Standards/NIST, 34 of those years as head of the science effort at the NCNR. Three years before formally joining NBS, Jack worked on projects with the designers of the NBS Reactor. His career thus spans the entire history of this facility from its construction to its growth into today's leading U.S. neutron facility; his strong leadership and steady presence have guided us the whole way. Jack's wisdom and friendship have also benefited the careers of all of us here and of the thousands of researchers who have used the facility. His knowledge and advice have strongly influenced the development of neutron science in the United States. Dan Neumann has taken over as leader of the Neutron Condensed Matter Science group, and Jack has resumed an active research program at the NCNR.

In another significant change, Sy Weiss announced his retirement from federal service this year. Sy came to NIST in 1999 and has served as Chief of Reactor Operations and Engineering since 2002 with responsibility for the operation of the reactor and for the process to renew our reactor operating license. However Sy's influence over the NCNR began long before he came to NIST. As Director of the Non-power Reactor and Decommissioning Project at the Nuclear Regulatory Commission, Sy was responsible for establishing and implementing a new regulatory policy for research and test reactors, which includes the NCNR, that draws clear and important distinctions between non-power and power reactors. Wade Richards, who joined NIST in 2003 will assume Sy's management duties for Reactor Operations and Engineering at the NCNR.

With this brief synopsis of the major "news" of the past year, I leave you to enjoy the following summaries of research highlights. Drawn from the many results of the past year, they reflect the high quality and amazing breadth of the research performed at the NCNR. For our part, this is what makes all of the other efforts worthwhile!

Pat Gallagher

The NIST Center for Neutron Research (NCNR)

Neutrons are powerful probes of the structure and dynamics of materials ranging from molecules inserted into membranes that mimic cell walls to protons migrating through fuel cells. The unique properties of neutrons (discussed below) can be exploited using a variety of measurement techniques to provide information not available by other means. They are particularly well suited to investigate all forms of magnetic materials such as those used in computer memory storage and retrieval. Atomic motion, especially that of hydrogen, can be measured and monitored, like that of water during the setting of cement. Residual stresses such as those inside stamped steel automobile parts can be mapped. Neutron-based research covers a broad spectrum of disciplines, including engineering, biology, materials science, polymers, chemistry, and physics.

The NCNR's neutron source provides the intense beams of neutrons required for these types of measurements. In addition to the thermal neutron beams from the heavy water or graphite moderators, the NCNR has a large area liquid hydrogen moderator, or cold source, that provides intense neutron beams for the only dedicated cold neutron facility presently operating in the U.S.

There are currently 29 experiment stations: four provide high neutron flux positions for irradiation and 25 are beam facilities most of which are used for neutron scattering research. The following pages show a schematic layout of the beam facilities. More complete descriptions of the instruments can be found at www.ncnr.nist.gov.

The NCNR supports important NIST research needs, but is also operated as a major national user facility with merit-based access made available to the entire U.S. technological community. Each year, about 2000 research participants from all areas of the country, from industry, academia, and government use the facility for measurements. Beam time for research to be published in the open literature is without cost to the user, but full operating costs are recovered for proprietary research. Access is gained mainly through a peer-reviewed, web-based proposal system with beam time allocated by a Program Advisory Committee twice a year. For details see www.ncnr.nist.gov/beamtime.html. The National Science Foundation and NIST co-fund the Center for High Resolution Neutron Scattering (CHRNS) that operates six of the world's most advanced instruments and provides time on CHRNS instruments through the proposal system. Some access to beam time for collaborative measurements with the NIST science staff can also be arranged on other instruments.

WHY NEUTRONS?

Neutrons reveal properties not available to other probes. They can behave like microscopic magnets, they can diffract like waves, they can set particles into motion losing or gaining energy and momentum in the process, and they can be absorbed.

WAVELENGTHS—range from 0.1 Å to 100 Å (1 Å = 0.1 nm), allowing them to form observable ripple patterns from structures as small as atoms to as large as proteins. At the NCNR, incident neutron wavelengths range from ~ 0.5 Å to ~ 20 Å.

ENERGIES—of millielectronvolts, of the same order as those of motions of atoms in solids or liquids, waves in magnetic materials, and vibrations in molecules. Exchanges of energy between neutrons and matter as small as nanoelectronvolts and as large as tenths of electronvolts can be detected.

SELECTIVITY—in scattering power varies from nucleus to nucleus somewhat randomly. Specific isotopes can stand out from other isotopes. Specific light atoms, difficult to observe with x-rays, are revealed by neutrons. Hydrogen, especially, can be distinguished from chemically equivalent deuterium.

MAGNETISM—makes the neutron sensitive to the magnetic spins of both nuclei and electrons, allowing the behavior of ordinary and exotic magnets to be detailed precisely.

NEUTRALITY—of the uncharged neutrons allows them to penetrate deeply without destroying samples, and pass through walls controlling a sample's environment allowing measurements under extreme conditions. Properties ranging from the residual stresses in steel girders to the unfolding motions of proteins are amenable to measurement by neutrons, and water moving within fuel cells can be imaged.

CAPTURE—characteristic radiation emanating from specific nuclei capturing incident neutrons can be used to identify and quantify minute amounts of material in pollutants or ancient pottery shards.

NIST Center for Neutron Research Layout

1. NG-0 Shown is MACS, a cold neutron Triple Axis Crystal Spectrometer under construction, with double focusing monochromator and multiple crystal analyzer/detectors that can be flexibly configured for several energies simultaneously or for high throughput at one energy.
2. BT-6 (temporary location) Neutron Imaging Facility for imaging hydrogenous matter in large components such as water in fuel cells or lubricants in engines.
3. BT-7 Thermal Triple Axis Spectrometer with large double focusing monochromator, and interchangable analyzer/detector systems (being installed).
4. BT-8 Residual Stress Diffractometer optimized for depth profiling of residual stress in large components.
5. BT-9 Triple Axis Crystal Spectrometer for measurements of excitations and structure.

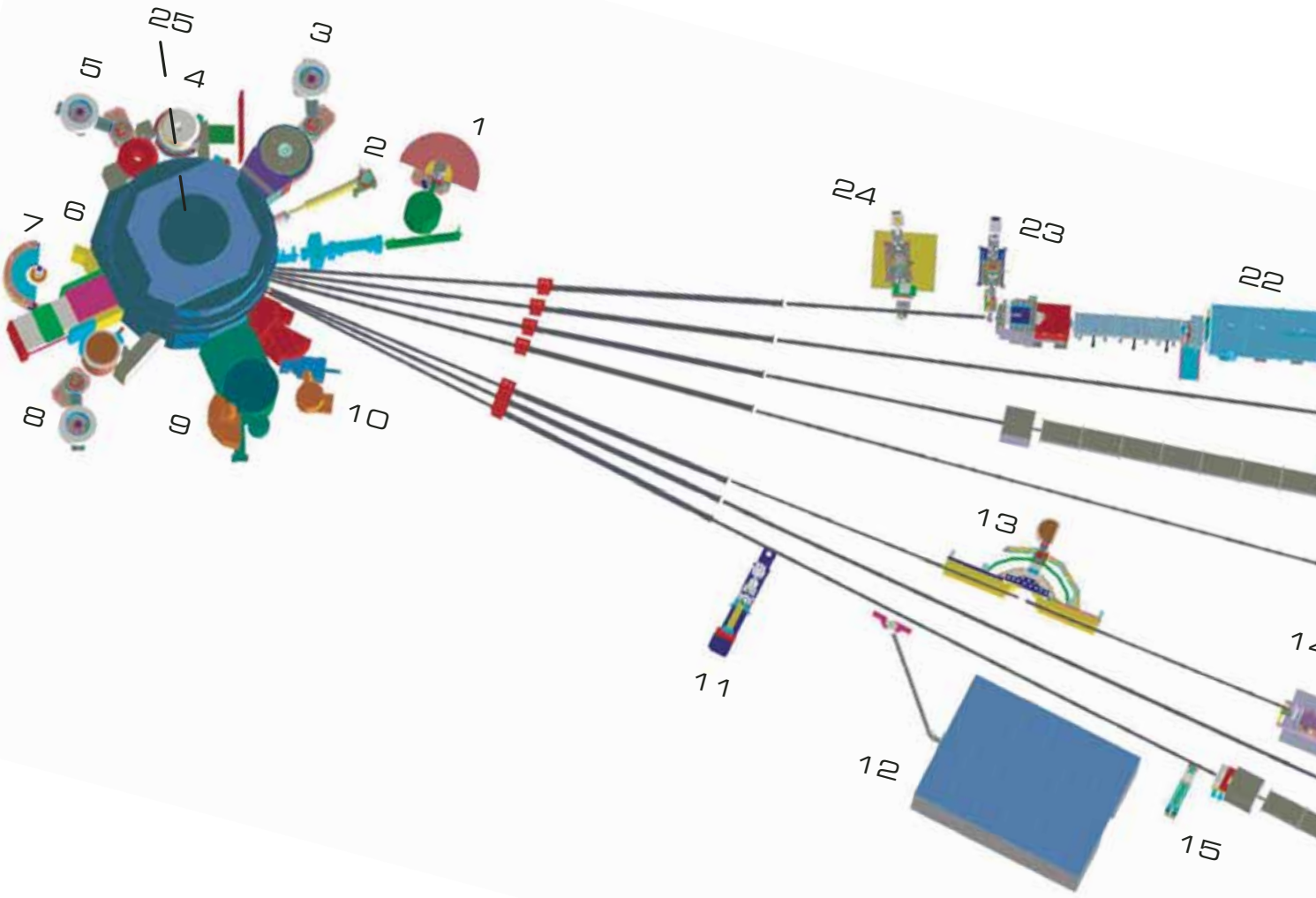

6. Thermal Column: a very well-thermalized beam of neutrons used for radiography, tomography, dosimetry and other experiments.

7. BT-1 Powder Diffractometer with 32 detectors; incident wavelengths of 0.208 nm, 0.154 nm, and 0.159 nm, with highest resolution of $\delta d/d = 8 \times 10^{-4}$.

8. BT-2 Triple Axis Crystal Spectrometer with polarized beam capability for measurement of magnetic dynamics and structure.

9. BT-4 Filter Analyzer Neutron Spectrometer with cooled Be/Graphite filter analyzer for chemical spectroscopy.

10. BT-5 Perfect Crystal Diffractometer SANS small angle neutron scattering instrument for microstructure up to 10^4 nm, sponsored by the National Science Foundation and NIST, part of the Center for High Resolution Neutron Scattering (CHRNS).

11. NG-7 Horizontal Sample Reflectometer allows reflectivity measurements of free surfaces, liquid vapor interfaces, as well as polymer coatings.

12. Neutron Interferometry and Optics Station with perfect silicon interferometer; vibration isolation system provides exceptional phase stability and fringe visibility.

13. Spin Polarized Triple Axis Spectrometer (SPINS) using cold neutrons with position sensitive detector capability for high-resolution studies—part of CHRNS.

14. Spin Echo Spectrometer for measuring dynamics from 100 ns to 10 ps, in partnership with ExxonMobil—part of CHRNS.

15. Prompt Gamma Activation Analysis cold neutron fluxes allow detection limit for H of 1 μg to 10 μg. Focused beams are available for profiling.

16. NG-7 30 m SANS for microstructure measurements, in partnership with NIST, ExxonMobil, and the Cold Neutrons for Biology and Technology program.

17. Neutron Physics Station offering three cold neutron beams having wavelengths of 0.5 nm, 0.9 nm, and "white" that are available for fundamental neutron physics experiments.

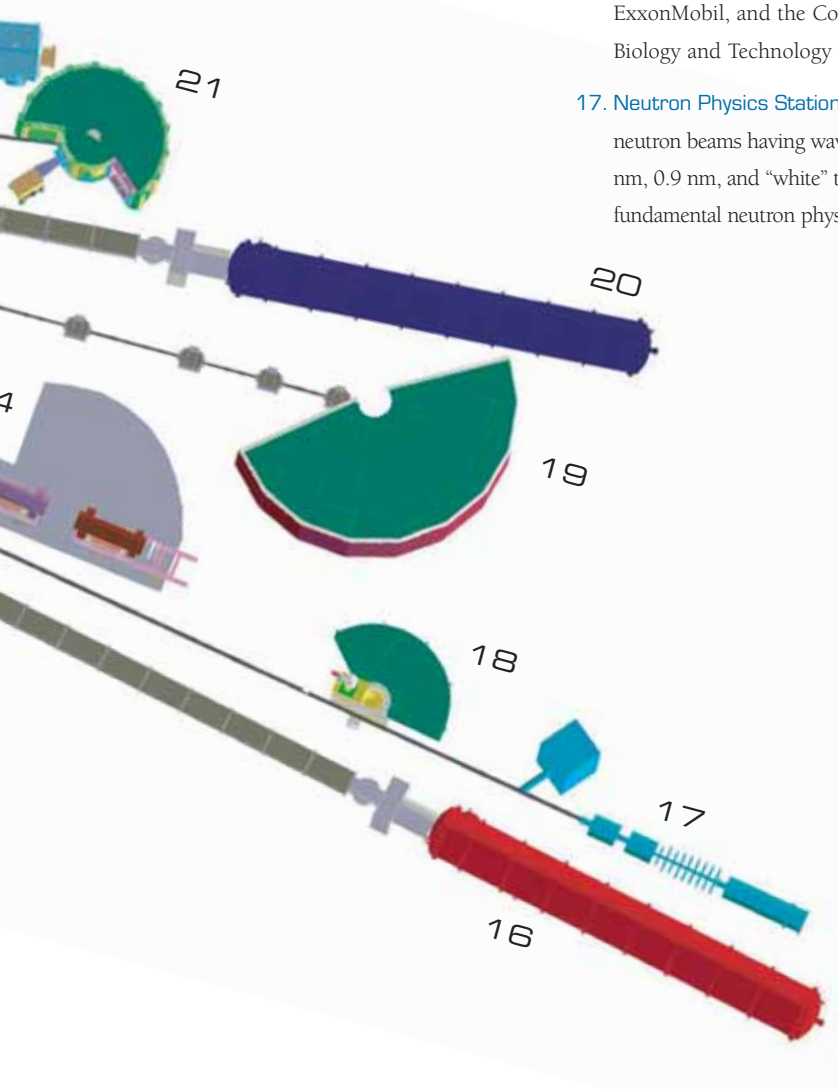

18. Fermi Chopper hybrid time-of-flight (TOF) Spectrometer for inelastic scattering with selected incident wavelengths between 0.23 nm and 0.61 nm.

19. Disk Chopper TOF Spectrometer, for studies of diffusive motions and low energy dynamics of materials. Wavelengths from ≈ 0.18 nm to > 2.0 nm give corresponding energy resolutions from ≈ 2 meV to < 10 μeV —part of CHRNS.

20. NG-3 30 m SANS for microstructure measurements sponsored by the National Science Foundation and NIST—part of CHRNS.

21. Backscattering Spectrometer high intensity inelastic scattering instrument with energy resolution < 1 μeV, for studies of motion in molecular and biological systems—part of CHRNS.

22. A Cold Neutron Depth Profiling instrument (not shown) for quantitative profiling of subsurface impurities currently at this site will be moved to another position. Shown is the NG-1 10 m SANS which is under construction.

23. Vertical Sample Reflectometer instrument with polarization analysis capability for measuring reflectivities down to 10^{-8} to determine subsurface structure.

24. Advanced Neutron Diffractometer/ Reflectometer (AND/R), a vertical sample reflectometer with polarization analysis and off-specular reflection capabilities for measuring reflectivities down to 10^{-8}. Part of the Cold Neutrons for Biology and Technology program committed to studies of biological membrane systems.

25. Thermal Neutron Capture Prompt Gamma-ray Activation Analysis Instrument at VT-5 with a neutron fluence rate of 3×10^8 /cm^2/s used for quantitative elemental analysis of bulk materials. Generally used for the analysis of highly hydrogenous materials (≈ 1 % H) such as foods, oils, and biological materials.

NCNR Images 2005

[1] NCNR's Hye-Jung Kang, Ying Chen, and William Ratcliff II at the new BT-7 spectrometer shakedown run.

[2] Chuck Majkrzak (NCNR) and Mike Fitzsimmons (LANL) celebrate a reflectometry result.

[3] NCNR's John Copley (left) guides 2005 summer workshop participants.

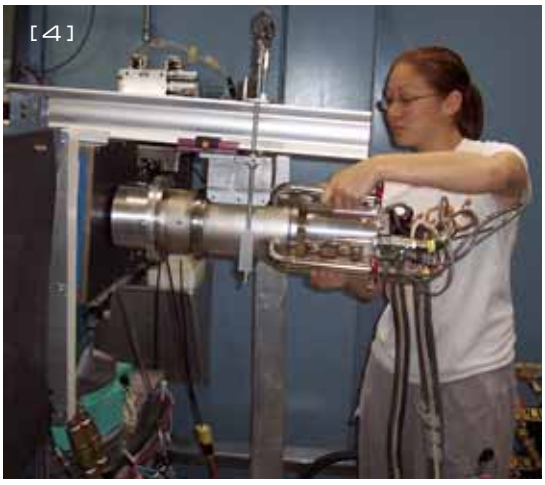

[4] SURF student Stephanie Moyerman prepares to mount a displex refrigerator.

[5] Confident Richard Azuah, Larry Kneller, and Rob Dimeo of the DAVE team.

[6] 2005 SURF students: Andrew Gardner, SUNY at Binghamton, Atiq Chowdhury, George Washington U., Stephanie Moyerman, Harvey Mudd Coll., Teresa Jacques, Smith Coll., Veronica Rodriguez, U. of Puerto Rico, and Daniel Miller, Bucknell U.

[7] NCNR's Julie Borchers takes joy in a thing of beauty: data.

[8] NCNR's Wang Chun Chen adjusts his ^{3}He cell neutron polarizer.

[9] Victoria Garcia-Sakai (NCNR) and Cecile Malardier-Jugroot (UC-Bkly) exult in a HFBS result.

[10] Amnon Aharony and Ora Entin-Wohlman (Tel Aviv) ponder a point with Brooks Harris (Penn).

[11] Olivier Isnard (CNRS) and Tobias Futterer (Rhodia) model neutron scattering on the lawn.

[12] Collaborators Thomas Hauet (Nancy), Philippe Mangin (LLB), and Julie Borchers (NCNR) caught off guard working.

[13] Bruce Gaulin, Jacob Ruff, Kirrily Rule, and Pat Clancy, all of McMaster U., happily pursue magnetic frustration at the DCS.

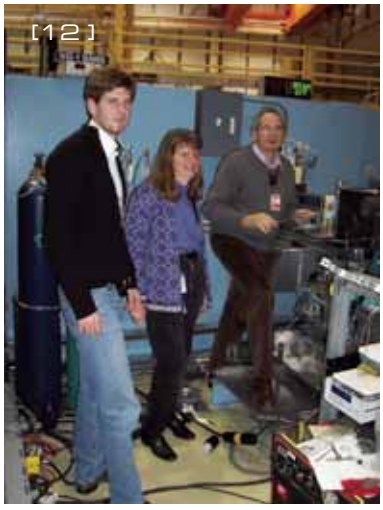

Hydrogen Adsorption Sites and Nanocage Formation in Metal-Organic Frameworks

T. Yildirim and M. R. Hartman
NIST Center for Neutron Research
National Institute of Standards and Technology
Gaithersburg, MD 20899-8562

The success of future hydrogen and fuel cell technologies is critically dependent upon the discovery of new materials that can store large amounts of hydrogen under ambient conditions. Metal-organic framework (MOF) compounds, which consist of metal-oxide clusters connected by organic linkers, are a relatively new class of nano-porous material that show promise for hydrogen storage applications because of their tunable pore size and functionality. Yet despite numerous experimental studies of hydrogen adsorption in MOF materials, the nature of the MOF-hydrogen interaction and the manner in which hydrogen molecules are adsorbed onto the structure are still unknown. Answers to these questions hold the key to optimizing these materials for practical hydrogen storage applications.

Here we use the difference-Fourier analysis of neutron powder diffraction data together with first-principles total-energy calculations[1,2], to directly determine the H_2 adsorption sites in MOF5 (the most widely studied MOF material, which consists of ZnO_4 clusters linked by 1,4-benzenedicarboxylate (BDC)). Surprisingly, we find that the MOF5 host lattice has enough space available to hold many hydrogen molecules, up to a mass fraction of ≈ 11 % at low temperatures. The ZnO_4-cluster is responsible for most of the adsorption while the organic linker plays only a secondary role. Equally important, we discover that at high concentration loadings hydrogen molecules form 3-dimensional (3D) networks of H_2 nano-clusters with intermolecular distances of 3.0 Å, which is significantly shorter than the intermolecular distances of 3.6 Å in pure solid hydrogen. These findings [1,2] suggest that MOF materials can also be used as templates to create artificial, interlinked hydrogen nanocages. Such materials could exhibit very unexpected properties due to confinement effects and small intermolecular separation, such as metallic behavior.

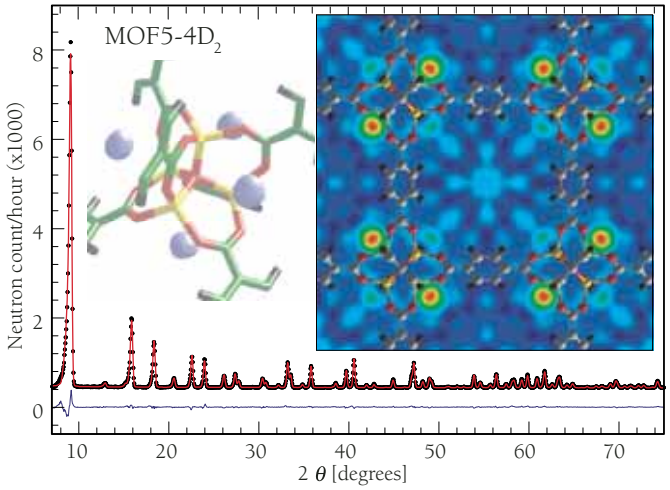

FIGURE 1: The neutron powder diffraction pattern (λ = 2.08 Å) of the MOF5-4D_2 at 3.5 K (dots) plus the Rietveld refinement (solid red line) with space group *Fm3m* and *a* = 25.91 Å, and difference plot (solid blue line). The inset shows the real-space difference-Fourier scattering-length density superimposed on the MOF5 structure, indicating the location of cup-sites for the first hydrogen adsorption (red-yellow-green region).

Due to the large incoherent cross section of H_2, the neutron diffraction data were collected on a MOF5 sample with the linker H atoms replaced with D atoms, which was synthesized as described in detail in Ref [1]. The diffraction data from this MOF5 host lattice obtained on BT-1 is in excellent agreement with the refinement and allows the deuterium atom positions of the BDC linker to be determined for the first time. Having characterized the MOF5 host lattice, we studied the adsorption of deuterium in MOF5 as a function of D_2 concentration, *n*, per formula unit (i.e., per 4Zn). The sample was loaded with nD_2 at the following concentrations: *n* = 4, 8, 14, 26, 34, and 44 D_2. We note that one H_2/4Zn corresponds to a mass fraction hydrogen uptake of about 0.26 %. None of the structural refinements of the deuterium loaded-samples showed any evidence of solid D_2, indicating that the deuterium was adsorbed onto the MOF5.

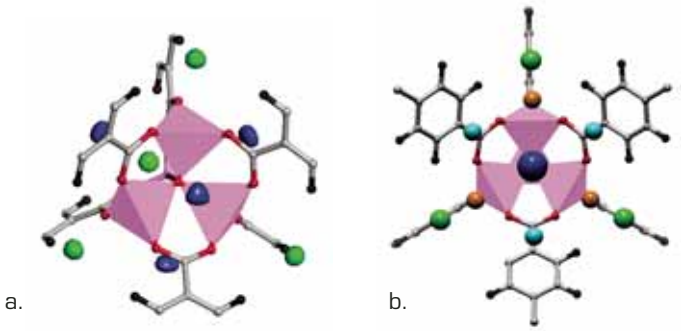

FIGURE 2: The hydrogen adsorption sites obtained from difference-Fourier analysis. (a) the first (blue) and second (green) absorption sites, respectively. (b) a view along the 3-fold axis, showing the four adsorption sites together. Also shown are the ZnO_2 -sites (brown) and Hex-sites (light-blue).

Figure 1 shows the diffraction pattern from MOF5 that was loaded with 4 D_2/4Zn. In order to locate the hydrogen adsorption sites, we first performed a Rietveld structural refinement using the model for the MOF5 host structure, ignoring the adsorbed D_2 molecules. The difference-Fourier scattering length density based upon this model, shown in the inset to Fig.1, was then used to locate the adsorbed D_2 molecules. The Fourier plot clearly shows where the hydrogen molecules are adsorbed (red-yellow-green region). The first adsorption sites (blue) are the positions at the center of the three ZnO_3 triangular faces, which resemble a cup shape and were termed the "cup-sites". There are four such sites, forming a tetrahedral cluster (blue region in Fig. 2(a)). Having determined the location of the first-adsorption sites, we further refined the structural model, explicitly including the D_2 molecules at the first adsorption site. The positions, isotropic thermal factors, and fractional occupancies of the adsorbed D_2 molecules were refined. The deuterium molecules were treated as point scatterers with double occupancy. The final refinement for a deuterium loading of 4D_2/4Zn is shown in Fig.1. For the 4D_2/4Zn loading, we also observed a small amount of D_2 (i.e., 10 %) adsorbed at a secondary adsorption site (green isosurface in Fig. 2(a)). For 8D_2/4Zn loading, these two adsorption sites are almost fully occupied. Unlike the cup-sites, the second adsorption sites are on top of single ZnO_3 triangles and were hence denoted as "ZnO_3-sites".

We observed that with further hydrogen loading (i.e., 14 and 26 D_2/4Zn), there are two additional adsorption sites that start to populate in almost equal proportion. These sites are shown in Fig. 2(b) as light-blue and brown spheres. The adsorption sites just above the two oxygen ions are called the "ZnO_2-sites". The fourth adsorption site is basically the top of the hexagonal linkers, which we termed the "Hex-site". The refined fractional-occupancy positions of these four sites are summarized in Fig. 2. At 26 D_2/4Zn loading, structural refinement indicates that these four adsorption sites are almost totally occupied yielding a H_2-uptake mass fraction of 6.8 %.

The difference Fourier analysis also indicated that at high concentrations such as 34 and 44 D_2/4Zn, hydrogen molecules start to form interesting nanocages in the cubic-cavities of the MOF5 structure as shown in Fig.3. Due to the hydrogen atoms on the organic linker, the cubic nanocage shown in Fig. 3(a) is slightly bent along the edges. For 34 D_2/4Zn loading, these two cage structures have about equal population; indicating some disorder. However, with increasing the hydrogen loading up to 44 D_2/4Zn we observed that the cubic cage is destabilized with respect to the more symmetric and exotic looking cage shown in Fig. 3(b). The intermolecular distances in these nanocages are on the order of 3.0 Å, much shorter than those found in solid H_2. At the maximum concentration of 44 D_2/4Zn, we also determined three additional hydrogen sites. These hydrogen atoms basically sit on the top of the square faces of the nanocage shown in Fig. 3(b), creating quite remarkable 3D interlinked nanocage structures. These results suggest that the MOF host lattices may be used as templates to build new artificial hydrogen nano-structures, which could have interesting properties due to the quantum nature of the molecules, confinement effects, and small intermolecular distances.

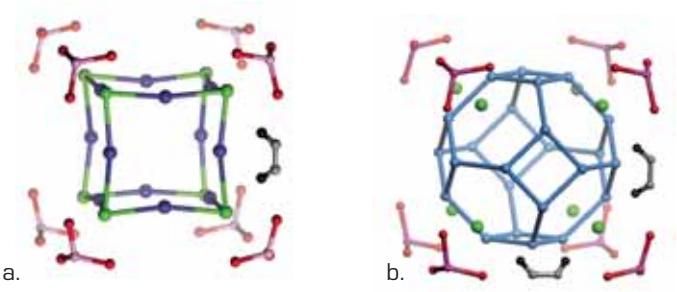

FIGURE 3: Two different hydrogen nanocages (blue and green spheres) obtained from Rietveld refinements at (a) 34 and (b) 46 D_2/4Zn loading, respectively. For clarity, only some of the ZnO_3 (red-pink) and CH bonds (grey-black) are shown.

In conclusion, using Rietveld structural refinement of neutron powder diffraction data in conjunction with difference-Fourier analysis and first-principles calculations, we have determined the hydrogen adsorption sites and binding energies in MOF5 as a function of hydrogen loading [1,2]. The results not only hold the key to optimizing MOF materials for hydrogen storage applications but also suggest that MOFs can be used as templates to create artificial interlinked hydrogen nanocages with novel properties.

REFERENCES

[1] For more information see http://www.ncnr.nist.gov/staff/taner/h2.

[2] T. Yildirim and M. R. Hartman, Phys. Rev. Lett. (cond-mat/0507220).

Ti-decorated Carbon Nanostructures for Potential High-Capacity Hydrogen Storage

T. Yildirim
NIST Center for Neutron Research, National Institute of Standards and Technology, Gaithersburg, MD 20899-8562

S. Ciraci
Bilkent University
Bilkent, Ankara, Turkey

Developing safe, cost-effective, and practical means of storing hydrogen is crucial for the advancement of fuel-cell technologies. The current state-of-the-art is at an impasse in providing any materials that meet a ≥ 6 % mass fraction hydrogen storage capacity required for practical applications. Much effort has been focused on the engineering of carbon-based materials such as nanotubes and transition metal hydrides without success. It is found that while the hydrogen-carbon interaction is too weak [1], the metal-hydrogen interaction is too strong for room temperature reversible storage. Using state-of-the-art first-principles calculations, we show here a novel way [1-4] to overcome this difficulty by forming artificial metal-carbide like structures on nanotubes [2] and C_{60} molecules [3].

Recent experiments and calculations suggest that it may be possible to coat carbon nanotubes uniformly with certain transition metals. A single Ti atom on an (8,0) single-wall nanotube (SWNT) has a magnetic ground state with S = 1 and a binding energy of 2.2 eV; this will serve as our reference system, denoted **t80Ti**. Figure 1a shows the energy variation as a single H_2 molecule approaches **t80Ti**. The energy first decreases slowly as the hydrogen gets closer to the nanotube and Ti. However, as the charge overlap gets large, the H_2 molecule is attracted towards the Ti atom with a sudden decrease in the energy. At this point, the H_2 molecule is still intact. The second sudden decrease in energy is achieved by dissociating the H_2 molecule into two H atoms. The interaction between H_2 and **t80Ti** is always attractive and therefore H_2 is absorbed onto a Ti atom without any energy barrier. The energy gain through this dissociative adsorption is about 0.83 eV with respect to spin-polarized calculations for the isolated H_2 and **t80Ti** systems.

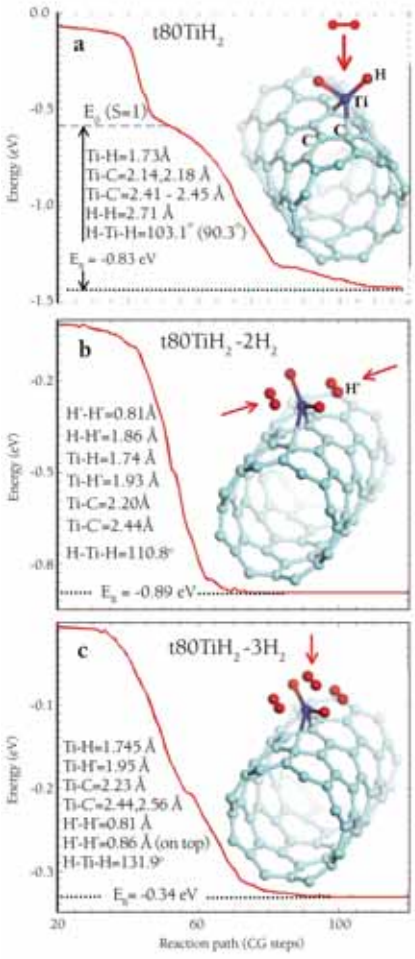

FIGURE 1: Energy vs. reaction paths for successive dissociative and molecular adsorption of H_2 over a single Ti-coated (8,0) nanotube.

Remarkably, it is also energetically favorable for the TiH_2 group to complex with additional hydrogen molecules. Figure 1b shows the energy variation as two hydrogen molecules approach the Ti atom; one from each side of the TiH_2 group. As in the case of single adsorption, the energy always decreases, first slowly and later very rapidly at which point both hydrogen molecules are strongly attached to the **t80TiH2** system.

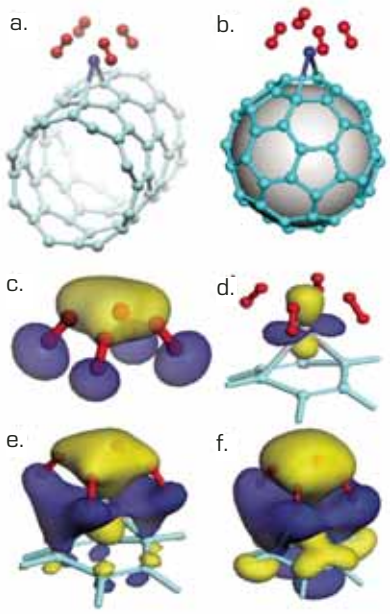

FIGURE 2: The symmetric and the most energetically the most stable configurations of four H_2 molecules absorbed on a (a) Ti-coated nanotube and (b) C_{60}. (c) The antibonding orbital of the four H_2 complex; (d)-(f) Isosurfaces of the bonding orbital at three different values, indicating the involvement of H-antibonding, Ti d-orbitals, and C π-orbitals in the bonding mechanism.

We denote the final product as **t80TiH$_2$- 2H$_2$**. The total energy change upon adsorption is about 0.89 eV (*i.e.*, 0.45 eV/H_2). Unlike the first adsorption, the two hydrogen molecules are intact but with a rather elongated bond length of 0.81 Å.

Figure 1c shows the energy evolution when a fourth hydrogen molecule approaches the **t80TiH$_2$-2H$_2$** system from the top. The energy again decreases continuously, indicating a zero-energy barrier. The final product, denoted as **t80TiH$_2$-3H$_2$**, is shown in the inset. The energy gained by the fourth adsorption, 0.34 eV/H_2, is slightly smaller than for the other cases but is still substantial. The H-H distance of the top H_2 is 0.86 Å. Several attempts to add a fifth hydrogen molecule at a variety of positions failed, suggesting a limit of 4 H_2/Ti.

The final optimized structures shown in Fig.1 need not be the global minimum. Among many different isomers tried for the four-H_2 system, we found a very symmetric configuration (denoted as **t80Ti- 4H$_2$**) that is 0.1 eV lower in energy than **t80TiH$_2$- 3H$_2$** (Fig. 2a). Here all four hydrogen molecules stay intact and benefit equally from bonding with the Ti atom. The average H-H bond distance is about 0.84 Å and each molecule has a charge of about 0.32 e. The average binding energy per H_2 molecule is 0.54 eV, which suggests that the bonding is an unusual combination of chemisorption and physisorption. Also note that each of the four H_2 molecules is located just above one of the four carbons of the hexagon over which the Ti atom is bonded. This suggests that carbon atoms also play an important role in the binding. These results can be explained by a simple Dewar-Chatt-Duncanson model where the interaction is caused by donation of charge from the highest occupied orbital of the ligand to the metal empty states and a subsequent back donation from filled *d*-orbitals to the lowest unoccupied orbital of the ligand. The analysis of the molecular orbitals shown in Fig. 2b supports this mechanism.

Next we show that a similar phenomenon occurs in light transition-metal decorated C_{60} [3]. Briefly, we find that while Sc and Ti prefer the hexagon (H) sites with a binding energy of 2.1 eV, V and Cr prefer double-bond (D) sites with binding energies of 1.3 and 0.8 eV, respectively. Heavier metals such as Mn, Fe, and Co do not bond on C_{60}. Once the metals are adsorbed on C_{60}, each can bind up to four hydrogen molecules with an average binding energy of 0.3 eV/H_2 to 0.5 eV/H_2.

To this point we have discussed the interaction of H_2 with a single Ti atom bonded to a nanotube, but clearly one can imagine attaching more Ti to a nanotube or C_{60}, thereby increasing the hydrogen storage capacity. Figure 3 shows two such high Ti-coverage cases for SWNT and C_{60}, respectively. The optimized bond-lengths and other parameters of the structures shown in Fig. 3 are very similar to those in the single-Ti case, indicating that the system has the capacity to accommodate many Ti and hydrogen atoms. In fact, these configurations, which have the chemical formulas, C_4TiH_8 and $C_{60}Ti_{14}H_{56}$, store hydrogen mass fractions of approximately 8 % and 7.5 %, respectively.

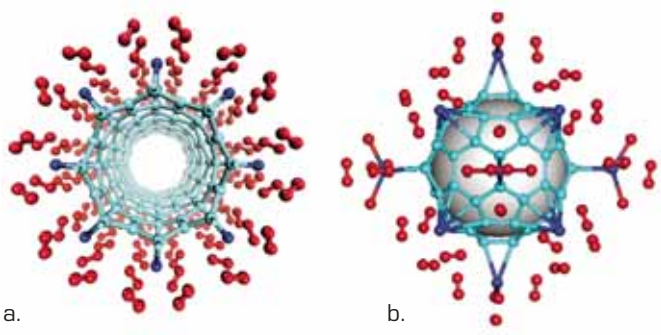

FIGURE 3: High-density hydrogen (red) coverage on (a) a Ti (blue)-coated nanotube and (b) C_{60} .

In conclusion, using accurate first-principles total-energy calculations we have shown that light transition metals such as a Ti atom adsorbed on a small diameter nanotube/C_{60} can bind up to four hydrogen molecules, a remarkable and totally unanticipated finding. At high metal coverages, it is possible to store hydrogen reversibly up to a mass fraction of 8 %. These results advance our fundamental understanding of dissociative and molecular chemisorptions of hydrogen in nanostructures and suggest a possible method of engineering new nanostructures for high-capacity storage and catalyst materials.

REFERENCES

[1] S.Dag, Y. Ozturk, S. Ciraci, and T. Yildirim, Phys. Rev. B (cond-mat/0504694).

[2] T. Yildirim and S. Ciraci, Phys. Rev. Lett. **94**, 175501 (2005).

[3] T. Yildirim, J., and S. Ciraci, Phys. Rev. B (cond-mat/0505046).

[4] For more information see http://www.ncnr.nist.gov/staff/taner/h2.

Pressure Dependence of Transitions in Supercooled, Confined Liquid Water

L. Liu and S-H. Chen
Massachusetts Institute of Technology
Cambridge, MA, 02139

A. Faraone
NIST Center for Neutron Research
National Institute of Standards and Technology
Gaithersburg, Maryland 20899-8562
and
University of Maryland
College Park, Maryland 20742-2115

C-W. Yen and C-Y. Mou
National Taiwan University
Taipei 106, Taiwan

Water is essential for all living systems and its properties impact our daily lives and environment directly. Therefore its counterintuitive behavior in the supercooled state stimulates interest in the scientific community. For example, some thermodynamic response functions and transport coefficients show a tendency to diverge at a singular temperature of 228 K. However, to date this supercooling behavior has been inaccessible because water inevitably freezes into ice before reaching this temperature. By confining water in nano-pores of mesoporous silica, we have succeeded in suppressing freezing and entering the supercooled region in this temperature range. Using the dynamic neutron scattering method we discovered a series of fragile-to-strong transitions in deeply supercooled water under pressure. We present new experimental findings that shed light on the nature of the liquid-liquid transition line and its end point, the anticipated second critical point much discussed in recent literature.

One of the most intriguing questions related to the unusual properties of supercooled water is whether two critical points exist in a single-component liquid [1]. The anomalies of the thermodynamic quantities become plausible if one postulates the existence of a second low-temperature critical point at about 228 K and at somewhat elevated pressure. Search for the existence of the predicted first-order liquid-liquid transition line [2] and its end point, the second low-temperature critical point [1] in water, has been hampered by intervention of the homogenous nucleation process which takes place at 235 K at ambient pressure. However, by confining water in nano-pores of mesoporous silica MCM-41-S with cylindrical pores of 14 Å diameter, we have been able to study the dynamical behavior of water in a temperature range down to 160 K without crystallization. Using the high-resolution quasi-elastic neutron scattering (QENS) method, with the Backscattering and Disc-Chopper spectrometers at the NCNR [3,4], we have determined the temperature and pressure dependences of the average translational relaxation time, $<\tau_T>$, for confined supercooled water using the Relaxing-Cage Model (RCM) [5] for the spectral analysis. $<\tau_T>$ essentially gives a measure of the structural relaxation time of the hydrogen-bond cage surrounding a typical water molecule.

The behavior of the shear viscosity η or equivalently the structural relaxation time τ of a supercooled liquid approaching its glass transition temperature is called 'fragile' when it varies according to the so-called Vogel-Fulcher-Tammann (VFT) law; and the behavior is called 'strong' when η or τ obeys the Arrhenius law. For water, a fragile liquid at room temperature and at moderately supercooled temperatures, Ito and coworkers [6] proposed that a 'fragile-to-strong' transition would occur at around 228 K, based on a thermodynamic argument.

In Fig. 1, we report the temperature variation of $<\tau_T>$ for water molecules as a function of pressure. Fig. 1 A, B, C and D clearly show a transition from a VFT law to an Arrhenius law. This transition of non-Arrhenius to Arrhenius behavior, previously observed at ambient pressure [5], is the signature of a fragile-to-strong dynamic transition predicted by Ito *et al.* [6]. However, in Fig. 1 E and F, the cusp-like transition becomes rounded off and it is no longer possible to define the fragile-to-strong transition temperature.

We show in Fig. 2 the observed pressure dependence of the fragile-to-strong transition temperature, T_L. Also depicted in the figure are the T_H and TMD lines. One should note that the T_L line has a negative slope, parallel to the TMD line, indicating a lower density for the low temperature phase. This T_L line also approximately tracks the T_H line, and terminates at the upper end by intersecting the T_H line at 1600 bar and 200 K.

Since what we observe experimentally is a dynamic transition, it is natural to ask whether T_L is also a liquid-liquid transition, and if so, what are

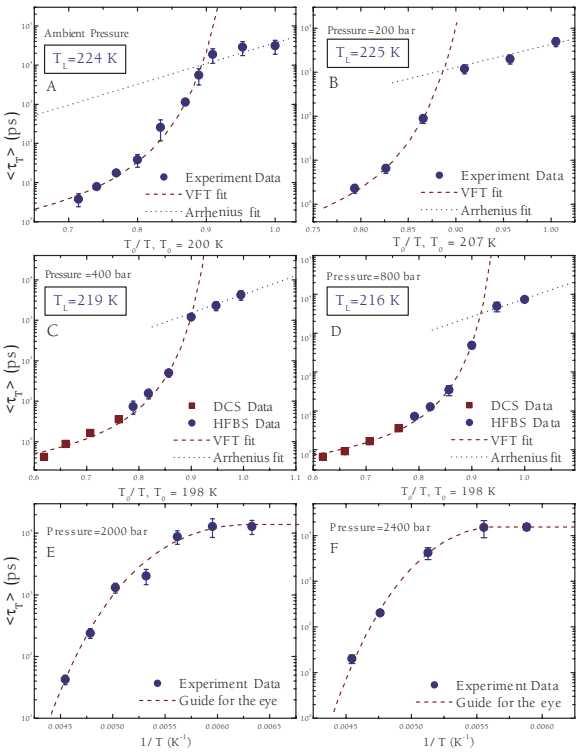

FIGURE 1: Temperature dependence of the average translational relaxation time plotted as $\log(<\tau_T>)$ vs T_0/T, where T_0 is the ideal glass transition temperature in the VFT law: ($\tau = \tau_0 \exp[DT_0/(T - T_0)]$). Data at ambient pressure, 200 bar, 400 bar, 800 bar, 2000 bar, and 2400 bar are shown in panels A, B, C, D, E, and F, respectively. In panels A, B, C, and D, there is a clear and abrupt transition from a VFT law at high temperature to an Arrhenius law ($\tau = \tau_0 \exp[E_A/k_BT]$) at low temperature, with the fitted transition temperature T_L indicated in the figure. In panels E and F, the temperature dependence follows neither the VFT law nor the Arrhenius law, and there is no clearly identifiable transition point.

the natures of the high-temperature and low-temperature liquids? According to our separate inelastic neutron scattering experiments, which measure the librational density of states of water contained in 18 Å pore size MCM-41-S, water remains in a disordered liquid state both above and below the fragile-to-strong transition at ambient pressure. Furthermore, our analysis indicates that the activation energy barrier for initiating the local structural relaxation is E_A = 20.5 kJ/mol for the low-temperature phase. On the other hand, our previous inelastic scattering experiments of the stretch-vibrational band of water [7] indicated that the effective activation energy for breaking a hydrogen bond at 258 K (in the high-temperature phase) is 13.4 kJ/mol. Combining these two observations, it is reasonable to conclude that the high-temperature liquid corresponds to the high-density liquid (HDL) where the locally tetrahedrally-coordinated hydrogen bond network is not fully developed, while the low-temperature liquid corresponds to the low-density liquid (LDL) where the more open, locally ice-like hydrogen bond network is fully developed.

Finally, it is important to address the location of the suggested second critical point [2]. We did not observe a clear evidence of critical slowing down near the low-pressure end of the T_L line. However, we did find that T_L ceases to change below 200 bar. An alternative scenario may be that the second liquid-liquid critical point lies in the negative pressure range as was found in the case of molecular dynamics (MD) simulated liquid silicon [8].

By confining water in nano-pores of silica glass, we are able to bypass crystallization and to study the effect of pressure on the dynamical behavior of deeply supercooled water using QENS. We observe clear evidence of a cusp-like fragile-to-strong dynamic transition. The transition temperature (T_L) decreases steadily with increasing pressure, following a line that tracks the homogenous nucleation temperature (T_H) line of bulk water until they intersect at a pressure of 1600 bar. Above this pressure, it is no longer possible to discern the characteristic cusp of the fragile-to-strong transition. We give reasons for identifying the T_L line as the first-order liquid-liquid transition line predicted by MD simulation.

Technical supports in measurements from E. Mamontov, J. Leao, I. Peral, J.R.D. Copley, and C. Brown at NIST NCNR are greatly appreciated.

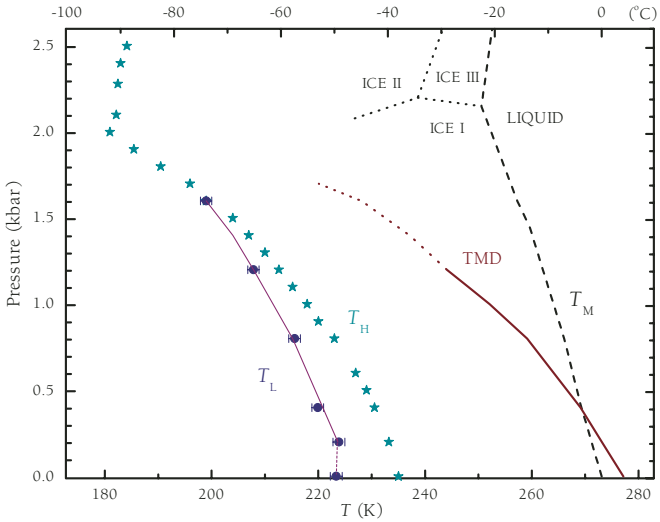

FIGURE 2: Summary of the pressure dependence of the fragile-to-strong dynamic transition temperature, T_L, plotted in the *P-T* plane (solid circles). Also shown are the homogeneous nucleation temperature line, denoted as T_H, and the temperature of maximum density line, denoted as TMD. Our experiment indicates that the T_L line terminates on the upper end when it crosses the T_H line. Note that we would like to identify the T_L the this line as the predicted liquid-liquid transition line in supercooled water [2].

REFERENCES:

[1] P. G. Debenedetti, H. E. Stanley, Physics Today **56**, 40 (June 2003).

[2] P. H. Poole, F. Sciortino, U. Essmann, H. E. Stanley, Nature **360**, 324 (1992).

[3] A. Meyer et al, Rev. Sci. Instrum. **74**, 2759 (2003).

[4] J. R. D. Copley, J. C. Cook, Chem. Phys. **292**, 477 (2003).

[5] A. Faraone et al, J. Chem. Phys. **121**, 10843 (2004).

[6] K. Ito, C. T. Moynihan, C. A. Angell, Nature **398**, 492 (1999).

[7] M. A. Ricci, S.-H. Chen, Phys. Rev. A **34**, 1714 (1986).

[8] S. Sastry, C. A. Angell, Nature Materials **2**, 739 (2003).

Diffusion of Water on Zirconia Nanoparticles

E. Mamontov
NIST Center for Neutron Research
National Institute of Standards and Technology
Gaithersburg, MD 20899-8562
and
University of Maryland
College Park, MD 20742

Because doped or undoped forms of zirconium oxide can be tailored to adjust the properties of robust catalyst supports with respect to surface area stability, porosity, and surface activity, they have come into increasing use in catalyst systems. As with any technologically important nano-particulate oxides having high specific surface areas, adsorbed water exerts a great influence on the surface properties of these materials. In particular, surface hydroxyl groups and undissociated water molecules play an important role in many reactions over zirconia, such as methanol synthesis and the isosynthesis reaction of $CO/H_2/H_2O$. In automotive catalysis, zirconia is an important additive to ceria, which is a catalyst for the water-gas shift reaction, $CO + H_2O \rightarrow CO_2 + H_2$.

In order to elucidate the key dynamics of surface water in nano-powder oxides, we performed a quasielastic neutron scattering (QENS) study of the dynamics of surface water on zirconium oxide nano-particles using the time-of-flight and backscattering neutron spectrometers at the NCNR. The results are described in terms of the "slow" dynamics of an inner layer of water, more tightly bound to the oxide surface, and the "fast" dynamics of a more mobile outer layer.

The hydration of nano-powder ZrO_2 was achieved simply by storing the sample under ambient conditions. The resulting sample had about two layers of mobile water molecules on top of the immobile surface hydroxyl groups. The Disc Chopper Spectrometer (DCS) was used with an incident neutron wavelength of λ = 9.0 Å yielding a resolution of about 19 μeV full-width at half-maximum (FWHM). This allowed us to access the dynamics of the outer hydration layer on the time scale of 1 ps to 100 ps. In order to access the longer time scales relevant to the dynamics of the inner hydration layer, we utilized the High Flux Backscattering Spectrometer (HFBS). This instrument provides an energy resolution of 0.85 μeV (FWHM) allowing one to probe time-scales over the range of about 100 ps to 1000 ps.

The significant dynamic range of the DCS experiment resulted in both the rotational (faster) and translational (slower) components contributing to the QENS signal. Thus, the spectra were fitted using a model scattering function that incorporated a sum of broader and narrower Lorentzians averaged over the random orientations of the local areas of the surface of the nano-particles with respect to the scattering vector Q [1]. The two-dimensionality of the surface diffusion process manifests itself in a scattering function for the translational diffusion component that is more sharply peaked than is a Lorentzian.

The rotational correlation time for the outer layer exhibits Arrhenius behavior, $\tau_R = 0.341[\text{ps}] \times \exp(E_{AR}/RT)$, with the activation energy E_{AR} = 4.5 kJ/mol, which is lower than the corresponding E_{AR} = 7.7 kJ/mol for bulk water. The rotational diffusion at room temperature is slower by about a factor of 2 compared to bulk water, whereas the translational diffusion slows down by a factor of 40.

The correlation time for the translational diffusion of the outer hydration layer exhibits an Arrhenius-type temperature dependence with an activation energy E_{AT} = 11.4 kJ/mol [1], in contrast with both bulk water, which is known to be strongly non-Arrhenius [3], and the inner hydration layer, discussed below, which also demonstrates non-Arrhenius behavior [2]. We found that the water molecules of the outer hydration layer perform two-dimensional jumps at a well-defined, almost temperature-independent distance of 4.2 Å to 4.3 Å in the course of a thermally-activated surface jump diffusion process. We propose that an Arrhenius-type temperature dependence of the translational correlation time, which is typically observed for the rotational, but not the translational diffusion component, is due to the fact that the number of hydrogen bonds formed by the molecules of the outer hydration layer with the nearest neighbors is less

than four. Thus, similar to a rotational diffusion jump, a translational diffusion jump may involve thermally activated breaking of a single hydrogen bond.

With the much smaller dynamic range of the HFBS, only the translational dynamics of the inner hydration layer is accessible. The backscattering spectra were Fourier transformed into the time regime and fitted using a model scattering function in the form of a stretched exponential. Stretch factors between 0.8 and 0.9 were obtained, indicating a distribution of the translational relaxation times. We have demonstrated that stretching of the exponential relaxation function and two-dimensionality of the surface diffusion process have different effects on the translational scattering function, and the stretch factors obtained from fitting are not affected by the two-dimensional nature of the surface diffusion [2].

The temperature dependence of the average residence time measured on HFBS was non-Arrhenius, suggesting that the translational motion of the water molecules of the inner hydration layer is more complex than surface jump diffusion observed for the molecules of the outer hydration layer. This is likely because the inner layer molecules form more hydrogen bonds with the nearest neighbors compared to the molecules of the outer hydration layer. The non-Arrhenius temperature dependence of the residence time suggests the presence of a singularity in the dynamics of the inner hydration layer. Fitting with the Vogel-Fulcher-Tamman (VFT) law, $\tau = \tau_0 \exp(DT_0/(T\text{-}T_0))$, yields the singularity temperature $T_0 = (189 \pm 1)$ K. The quality of the fit is demonstrated in Fig. 1. Existence of such a singularity indicates the importance of cooperative effects in the dynamics of the inner hydration layer as opposed to the outer hydration layer.

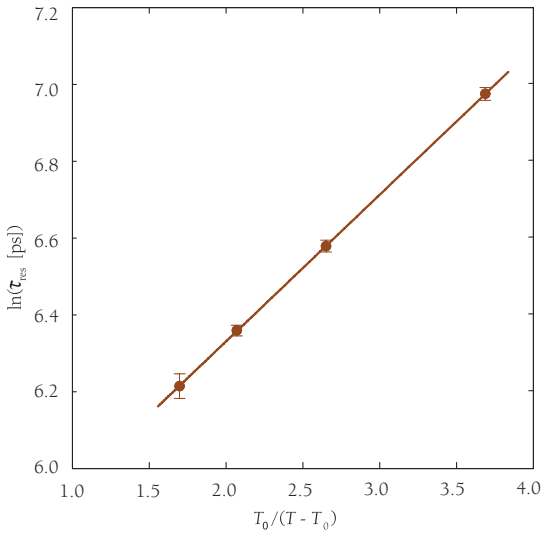

FIGURE 1: The temperature dependence of the residence time for the translational diffusion component of "slow" (inner layer) surface water in ZrO_2 fitted with a VFT law, $\tau = \tau_0 \exp(DT_0/(T\text{-}T_0))$, and plotted as a function of $T_0/(T\text{-}T_0)$, with $T_0 = 189$ K.

Interestingly, despite being slower by two orders of magnitude, the translational motion of the molecules of the inner hydration layer may have more in common with bulk water compared to the outer hydration layer, the dynamics of which is slower than that of bulk water by just one order of magnitude.

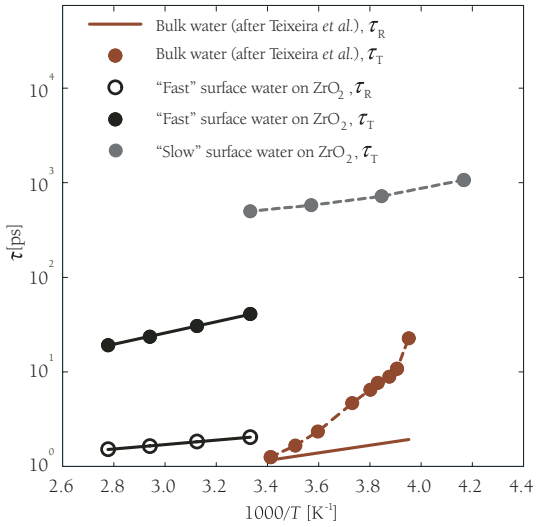

FIGURE 2: The temperature dependence of the residence times for the translational (τ_T) and rotational (τ_R) diffusion of surface water in ZrO_2. The "slow" surface water is interpreted as an inner layer more tightly bound to the oxide, and the "fast" water as an outer layer atop the inner one. The data for bulk water (after Teixeira *et al*. [3]) are shown for comparison.

To summarize, our QENS study of surface water in ZrO_2 has revealed the dynamics of "slow" and "fast" hydration water as shown in Fig. 2. The former was ascribed to the water molecules in direct contact with the surface hydroxyl groups (that is, the inner hydration layer), while the latter was associated with the water molecules in contact with the molecular surface water (that is, the outer hydration layer). At room temperature, the translational dynamics of the outer and inner hydration layers is slower than that of bulk water by a factor of 40 and 500, respectively, compared to that of bulk water, whereas the rotational dynamics of the surface water is only slightly slower than that of bulk water.

REFERENCES

[1] E. Mamontov, J. Chem. Phys. **121**, 9087 (2004).

[2] E. Mamontov, J. Chem. Phys., **123** 024706 (2005).

[3] J. Teixeira, M.-C. Bellisent-Funel, S.-H. Chen, A. J. Dianoux, Phys. Rev. A **31**, 1913 (1985).

Cement: The Hydration of Tricalcium and Dicalcium Silicate Mixtures

V. K. Peterson
NIST Center for Neutron Research
National Institute of Standards and Technology
Gaithersburg, MD 20899-8562
and
University of Maryland
College Park, MD 20742-2115

D. A. Neumann
NIST Center for Neutron Research
National Institute of Standards and Technology
Gaithersburg, MD 20899-8562

R. A. Livingston
Federal Highway Administration
McLean, VA 22101-HRDI-05

Portland cement is the world's most important construction material, with annual production currently exceeding 800 million metric tons. The structure, molecular composition, and physical properties of cement vary immensely during hydration, changing from a material that can be poured and worked to one that is literally hard as rock. The details of this metamorphosis depend on the structure and composition of the starting cement, as well as the hydration conditions. Correlating the original composition and hydration kinetics with the final properties is the aim of this research. With better understanding of these processes, we improve our ability to control and design the final product properties. Neutrons are well suited for the investigation of the structure and reaction mechanisms of cement, as they are particularly sensitive to hydrogen (and thus water), and are highly penetrating, so they can sample larger volumes than other methods. This research reveals complexities of the hydration of cement, and suggests ways to exploit these results to improve cement performance.

The initial cement powder is a complex mixture of several calcium silicates, calcium aluminates, calcium alumino-ferrites, as well as other phases. Tricalcium silicate is the most abundant phase in Portland cement and is primarily responsible for giving cement its strength in the crucial first 24 hours of hydration. Thus, its hydration has been extensively studied. Dicalcium silicate, the second most abundant component, is much less reactive than tricalcium silicate and as such was not expected to contribute significantly to the overall hydration in the critical first 24 hours. Although it was recognized that the hydration of cement involves the *interaction* of the different components, very little is known about combined reactions. In this highlight we report the results of quasielastic and inelastic neutron scattering (QENS and INS) studies of hydration in mixtures of only tricalcium and dicalcium silicate that correlate well with the strengths of mortars of mixtures of these components.

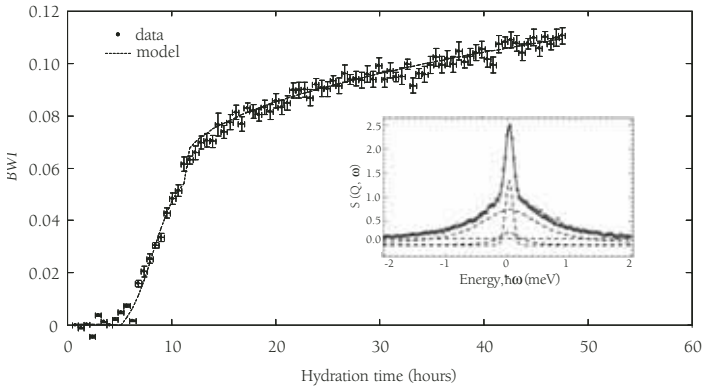

FIGURE 1: Diffusion models and *BWI* curve for a mixture containing a mass fraction of 50 % tricalcium silicate. Errors are absolute. The inset shows a snapshot of QENS data fitting at 5 hours hydration time, detailing the Gaussian and three Lorentzian profiles used to differentiate H in various states (dotted lines). The solid line indicates the overall fit.

QENS data were obtained using the NIST Fermi chopper time-of-flight neutron spectrometer (FCS). The kinetics of the hydration reaction were characterized using the "Bound Water Index" (*BWI*) which was determined from the ratio of the amount of less mobile (bound) hydrogen (H) relative to the total H in the system. As H is initially only present in the water and is transferred to the reaction products during the hydration of tricalcium and dicalcium silicate, the *BWI* is essentially a measure of the amount of product. Thus, a plot of *BWI* versus time describes the kinetics of the hydration reaction. A typical *BWI* curve is shown in Fig. 1. After an initial dormant period, two hydration mechanisms can be identified: (a) the nucleation and growth of products, when the cement starts to set, and (b) diffusion- limited hydration, occurring when the permeability of the reaction products limits the ability of water to reach the hydrating particles.

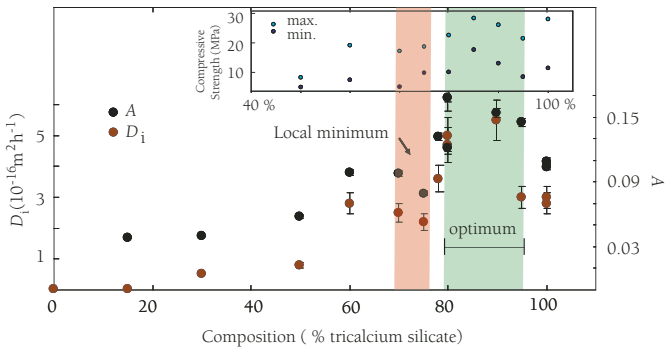

FIGURE 2: Variation of predicted amount of product (A, •) and diffusion coefficient (D_i, •) with mixture composition. Error bars in D and A are 1 standard deviation, and in composition are smaller than the points. The inset shows the compressive strengths for mortars of the same components after 28 days hydration.

Comparison of the *BWI* curves for various tricalcium and dicalcium silicate mixtures indicates that the reaction at intermediate compositions cannot be simply described as a linear combination of the end points. Fitting of the hydration curves to a kinetic model allows this difference in the hydration to be quantified by extracting several parameters related to the kinetics. For example, the parameter A can be determined, which represents the expected *BWI* after infinite time if the nucleation and growth mechanics had not been interrupted. A is useful for predicting early strength development, as the amount of product (as well as type) correlates with cement strength. Parameter A exhibits a maximum between 80 and 95 % as a function of the starting mass fraction of tricalcium silicate in the mixture. Figure 2 displays A versus starting tricalcium silicate mass fraction, along with the effective diffusion constant of water, D_i, which limits the reaction rate in the diffusion-limited regime. The trend of D_i correlates well with that observed for the parameter A. Compressive strength (shown inset in Fig. 2) of mortars of these mixtures after 28 days hydration also correlates with the quasielastic neutron scattering results.

In order to quantify the amount of $Ca(OH)_2$ produced during the reaction, INS data were obtained using the NIST filter analyzer neutron spectrometer (FANS). The amount of $Ca(OH)_2$, an important hydration product, present at any time during hydration, was determined by comparing the intensity of a vibrational mode at 42 meV to one in a reference sample of $Ca(OH)_2$. The results displayed in Fig. 3 reveal a clear maximum in the amount of $Ca(OH)_2$ produced at a mass fraction of 90 % tricalcium silicate.

The quasielastic and inelastic neutron scattering data clearly indicate that the reaction products formed during the nucleation and growth regime for mixtures containing 80 % to 95 % tricalcium silicate differ significantly from those produced by other mixtures. Moreover, these results demonstrate that more products form during early hydration times in this composition range. This is particularly surprising for calcium hydroxide since there is less total Ca in mixtures containing dicalcium silicate than in tricalcium silicate alone. These results also suggest that the interaction affects the microstructure, and therefore the strength, of the product. In fact, the strengths of mortars of these mixtures cured for 28 days display a peak at 85% tricalcium silicate.

This study has shown that the overall hydration reaction of cement is more complex than a simple linear combination of the reactions for the individual components and has demonstrated that tricalcium and dicalcium silicates interact during the hydration reaction of mixtures of these two crucial components of cement clinker. Unexpectedly, favorable reaction mechanics occur when a mass fraction of 80 % to 95 % tricalcium silicate mixture is used, where it was previously thought that dicalcium silicate played no role during early hydration. Industrial cement clinker contains a mass fraction of approximately 70 % to 80 % tricalcium silicate out of the total calcium silicate phases, less than the amount determined from this work of 80 % to 95 % for optimal hydration mechanics, and alarmingly close to the local minimum for hydration mechanics, and strength, between 70 % and 75 %. This suggests that increasing the tricalcium silicate content by 5 % to 15 % may lead to improved cement. However, there are many other components in cement clinker and other interactions could also affect the performance of the final material.

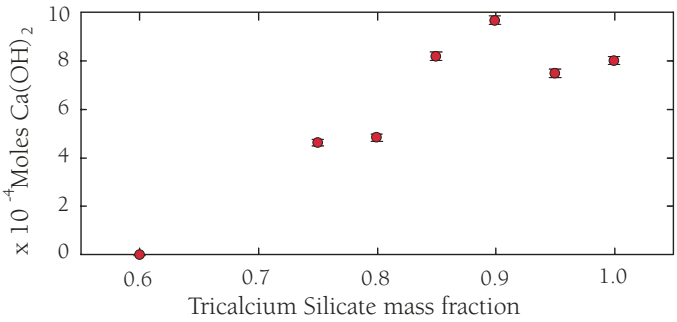

FIGURE 3: Amount of $Ca(OH)_2$ produced at 22 hours by various tricalcium and dicalcium silicate mixtures, determined by INS. Errors in amount are 1 standard deviation, and in composition are smaller than the points.

REFERENCES

[1]. V. K. Peterson, D. A. Neumann, R. A. Livingston, J. Phys. Chem. B. (submitted 2005).

[2] V. K. Peterson, D. A. Neumann, R. A. Livingston in *Neutron and X-Ray Scattering as Probes of Multiscale Phenomena*, ed. S.R. Bhatia, P.G. Khalifah, D. Pochan, and P. Radaelli (Mater. Res. Soc. Symp. Proc. **840**, Boston, MA, 2004).

Phase Behavior and Local Dynamics of Concentrated Triblock Copolymer Micelles

H. Yardimci, B. Chung, J. L. Harden, and R. L. Leheny
Johns Hopkins University
Baltimore, MD, 21218

Polymer solutions and colloidal suspensions are representative complex fluids. For block copolymers in selective solvents, microphase separation can lead to the formation of spherical structures called micelles in which both the polymeric and colloidal nature of the structures figure significantly. For example, at high concentrations, interactions between micelles become important and the micelles can undergo order-disorder transitions akin to the crystallization of spherical colloids. However, because of the polymeric nature of these micelles, the characteristics of this phase behavior are expected to differ considerably from hard-sphere colloids. Similarly, the dynamical behavior of the micelles within these concentrated phases should reflect both colloidal and polymeric aspects of the system. We have conducted a neutron scattering study of concentrated triblock copolymer micelle solutions that addresses these issues. The study includes small angle neutron scattering (SANS) to characterize the structure and phase behavior of the micelles and neutron spin echo (NSE) experiments to examine the local dynamics and their dependence on micelle structure and phase.

The micelle-forming copolymer under study is Pluronic, an ABA-type triblock with outer blocks of polyethylene oxide (PEO) and a central block of polypropylene oxide (PPO). Due to the relative hydrophobicity of PPO, Pluronic in aqueous solution with appropriate ratios of PPO to PEO forms spherical micelles over a broad range of concentration and temperature, with PPO cores and swollen PEO coronas. Our study involves two species of Pluronic, F68 and F108, that have the same PPO to PEO ratio; in each case, the chains have a mass fraction of 80 % PEO. However, the overall chain length of F108 is larger than that of F68 by roughly a factor of two. Specifically, the average molecular weight of F108 is 14 600 g/mol while that of F68 is 8400 g/mol. Comparing the species provides insight into how the phase behavior and local dynamics vary with chain length.

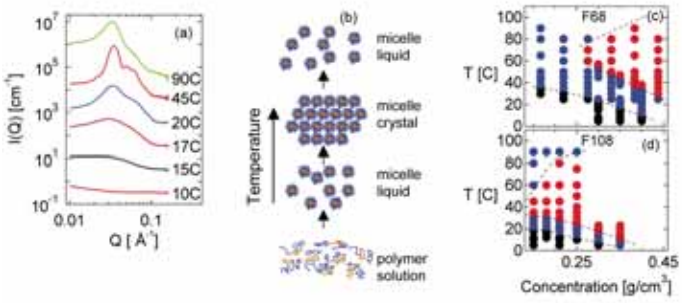

FIGURE 1: (a) SANS intensity of 0.21 g/cm^3 F108 Pluronic solution at several temperatures. (b) Schematic pictures of the polymer structure implied by the SANS. (c) and (d) Phase diagrams for F68 and F108 Pluronic solutions as determined by SANS. Three phases are identified: polymers dissolved in solution (black), micelles with liquid-like order (blue), and micelles with crystalline order (red).

Figure 1(a) displays the SANS intensity $I(Q)$ for 0.21 g/cm^3 F108 in D_2O at several temperatures. Consistent with previous studies of Pluronic [1], the lineshape indicates a sequence of phase transformations with increasing temperature starting from a dissolved polymer solution at low temperature and proceeding to micelles with liquid-like order, followed by a micelle crystal, and then finally back to a micelle liquid, as shown schematically in Fig. 1(b). Phase diagrams constructed from SANS for F108 and F68 solutions, shown in Figs. 1(c) and 1(d), reveal two significant differences between the species. First, the minimum concentration for crystalline order is at higher concentration for the shorter-chain F68. Second, the temperature range of the low-temperature micelle liquid region is larger for F68 than for the longer-chain F108 (approximately 30º C for F68 compared with about 10º C for F108). These differences indicate a stabilization of the micelle liquid against crystallization for the shorter-chain copolymer. We associate this trend with similar chain-length dependent effects observed in highly asymmetric block copolymer melts that microphase separate into spherical domains. In the melts, a liquid-like packing of spheres is often observed over an extended temperature range between the disordered phase, in which the blocks are fully mixed and a crystalline phase.

Recent self-consistent field theory [2] has identified the liquid-like micellar order in melts with strong, localized composition fluctuations within the disordered phase, and has concluded that the only true thermodynamic transition is between the disordered and crystal states. The theory further predicts that the temperature range of the liquid-like population of micelles decreases with increasing chain length, like in Figs. 1(c) and (d), indicating that chain-length dependent compositional fluctuations play an important role in determining the Pluronic phase behavior as well. However, since the presence of solvent in the Pluronic solutions complicates comparison with these predictions, additional theoretical work would be valuable in understanding the importance of such chain-length dependent fluctuations to the phase behavior of micellar solutions.

Turning to the dynamical properties of the micelles, Fig. 2(a) displays the intermediate scattering function $S(Q,t)/S(Q,0)$ of 0.3 g/cm^3 F68 in D_2O measured with NSE in the low-temperature micelle liquid phase at various wave vectors near and above the interparticle peak in $I(Q)$. The measurements reveal a strongly Q-dependent lineshape that deviates from a single relaxation. The inset of Fig. 2(b) shows $S(Q,t)/S(Q,0)$ of 0.21 g/cm^3 F108 in the micelle liquid and crystalline phases. The dynamics are remarkably insensitive to phase and hence to the local micellar packing.

To characterize these dynamics more precisely, we have performed additional measurements on solutions of F68 with deuterated PEO. The deuterated PEO blocks have a scattering length density that closely matches that of D_2O; hence the hydrogenated PPO in the micelle cores dominates the signal. Figure 2(b) shows a comparison of the intermediate scattering functions for F68 solutions with deuterated and hydrogenated PEO in the low-temperature micelle liquid phase. A stretched-exponential lineshape with stretching exponent near 0.5 describes accurately the intermediate scattering function for the micelle solutions with deuterated corona at all temperatures and wave vectors, as illustrated by the solid line in Fig. 2(b). Figure 2(c) displays results for the correlation time τ_{PPO} extracted from such fits in the low-temperature micelle liquid phase. The solid line through the data is the relation $\tau_{PPO} \sim Q^{-4}$. Such a stretched correlation function with $\tau \sim Q^{-4}$ is a signature of Rouse modes [3]. Thus, we conclude that NSE captures the segmental chain dynamics of the PPO in the micelle cores. In particular, translational diffusion is not observed (see dashed line in Fig. 2(c)) presumably due to slowing by hydrodynamic interactions [4] among the concentrated micelles.

Armed with these results, we analyze the NSE measurements for the solutions of fully hydrogenated F68 by assuming that the PPO dynamics are identical to those determined for the solutions with deuterated PEO. Specifically, we fit the results for the hydrogenated Pluronic with a two-component lineshape that includes a term identical to that obtained for the Rouse modes in the core and a term that is a simple exponential designed to account for the contribution from the corona. The success of this fitting, illustrated by the dashed line in Fig. 2(b), implies a clean separation of segmental dynamics between core and corona. The correlation times for the PEO dynamics, τ_{PEO}, extracted from these fits vary with wave vector as $\tau_{PEO} \sim Q^{-2}$, as shown in Fig. 2(c), indicating that the NSE measurements capture the diffusive motion in the corona. The corresponding diffusion coefficient matches quantitatively that expected for

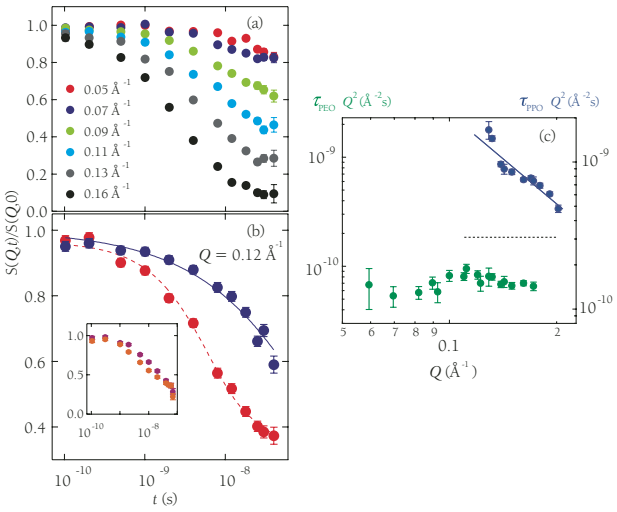

FIGURE 2: (a) The intermediate scattering function measured with neutron spin echo for 0.30 g/cm^3 F68 at 30° C in the low-temperature micelle liquid phase at several wave vectors. (b) The intermediate scattering function at Q = 0.12 Å^{-1} for fully hydrogenated F68 (red) and for F68 with deuterated PEO blocks (blue) in the low-temperature micelle liquid phase. The solid line is the result of a fit to a stretched exponential form. The dashed line is the result of a fit to the sum of an exponential and a stretched exponential. The inset to (b) shows a comparison of the intermediate scattering functions for 0.21 g/cm^3 F108 in the micelle liquid (purple) and micelle crystal (orange) phases. (c) The characteristic relaxation times for dynamics in the PPO core (blue) and the PEO corona (green) of 0.30 g/cm^3 F68 in the micelle liquid phase.The solid line is the relation $\tau_{PPO} \sim Q^{-4}$ expected for Rouse modes. τ_{PEO} follows a form $\tau_{PEO} \sim Q^{-2}$ expected for longitudinal diffusion modes of a polymer brush. The dashed line shows translational diffusion times based on an extrapolation of the behavior in dilute suspensions [5].

the longitudinal diffusive modes of polymer brush layers in good solvents [6,7]. Thus, we interpret that the PEO blocks in the corona behave dynamically just like a polymer brush, despite the large curvature of the interface separating core and corona.

In conclusion, this combined SANS and NSE study of Pluronic has highlighted several features of polymer micelle solutions. The phase behavior of the solutions indicates chain-length dependent composition fluctuations. The segmental dynamics probed with NSE, however, while strongly reflecting the microphase separated micellar environment, remain largely insensitive to the micellar phase behavior.

REFERENCES

[1] R. K. Prud'homme, G. Wu, D. K. Schneider, Langmuir **12**, 1651 (1996).

[2] J. Wang, Z.-G. Wang, Y. Yang, Macromolecules **38**, 1979 (2005).

[3] B. Ewen, D. Richter, Adv. Polym. Sci. **134**, 1 (1997).

[4] P. N. Segré, P. N. Pusey, Phys. Rev. Lett. **77**, 771 (1996).

[5] Z. Zhou, B. Chu, J. Colloid Interface Sci. **126**, 171 (1988).

[6] P. G. de Gennes, Adv. Colloid Interface Sci. **27**, 189 (1987).

[7] G. E. Yakubov *et al.*, Phys. Rev. Lett. **92**, 115501 (2004).

Rheo-SANS: Gap-Resolved SANS of Shear-Induced Alignment of Wormlike Micelles

M. Liberatore, F. Nettesheim and N. J. Wagner
University of Delaware
Newark, DE 19716

L. Porcar
NIST Center for Neutron Research
National Institute of Standards and Technology
Gaithersburg, MD 20899-8562
and
University of Maryland
College Park, MD 20742

Wormlike micellar solutions formed by self-assembled surfactants exhibit rheological properties such as shear thinning and suppression of turbulent flow that are related to the flow-induced changes in their structural conformations or orientations. These flow properties are of relevance in such applications as thickeners, drag reducers and flow improvers in the food and cosmetics industries.

In this highlight we report measurements of the microstructure of a shear-induced phase separating (SIPS) wormlike micellar solution by performing small angle neutron scattering (SANS) measurement using a novel shear cell capable of gap-resolved measurement in the **1-2** (velocity velocity-gradient) plane. Quantitative results show evidence for shear-induced microphase separation accompanied by shear banding. The results suggest that both concentration fluctuations and gradients in segmental alignment occur during SIPS.

The nonlinear rheological behavior of complex fluids includes rich phenomena such as shear-induced phase separation (SIPS). Although many polymeric and self-assembled systems show a wide variety of related phenomena, self-assembled solutions of surfactants forming wormlike micelles [1] have proven to be especially robust in exhibiting clear signatures of SIPS and as such, are of significant scientific interest [2–4]. A rheological signature of SIPS in wormlike micelles is a stress plateau. Models suggest this corresponds to a multi-phase flow regime composed of a low shear micellar solution and a high-shear, highly aligned wormlike fluid state. While global rheological response is important in characterizing these wormlike micellar solutions, local velocity and concentration profiles provide a greater understanding of the phase separation/shear banding phenomena.

A variety of techniques, employed in previous studies, such as dynamic light scattering and NMR, have provided local velocity profiles of the shear-banded state. More recently, particle-tracking velocimetry [4] provided spatial and temporal information. However, there is little information provided about the microstructure of the high shear band due to optical turbidity. Therefore, SANS investigations under shear are of great value, especially a combination of studies in all three planes of the flow field, i.e., the flow-vorticity (radial beam configuration) velocity gradient-vorticity (tangential configuration), and the flow-velocity gradient (**1-2** plane) planes.

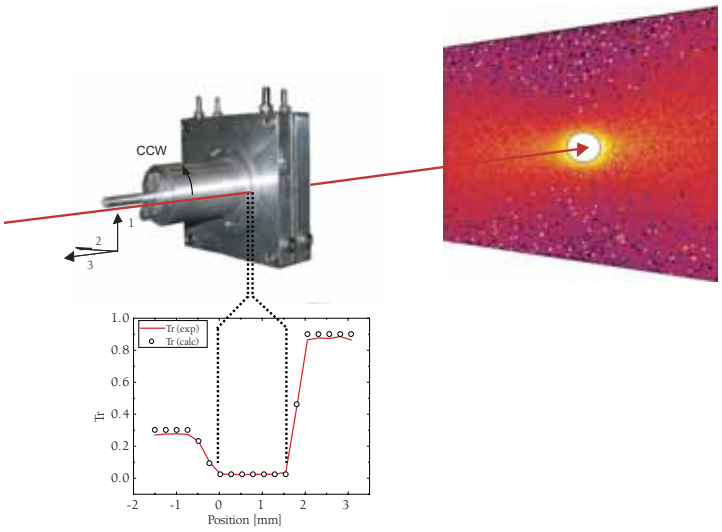

FIGURE 1: Illustration of the **1-2** plane shear cell in the neutron beam allowing for gap-resolved studies. The graph shows the recorded and predicted transmission as a function of beam position along the **2** axis using the 0.6 mm slit.

Small angle neutron scattering patterns collected in the **1-2** plane employed a newly designed aluminum Couette cell (15 mm inner radius, 2 mm gap and 10 mm path length) that is illustrated in Fig. 1. A slit preceding the cell reduced the neutron beam to 0.6 mm in width by 2.0 mm in height. The center of the narrowed beam could be positioned

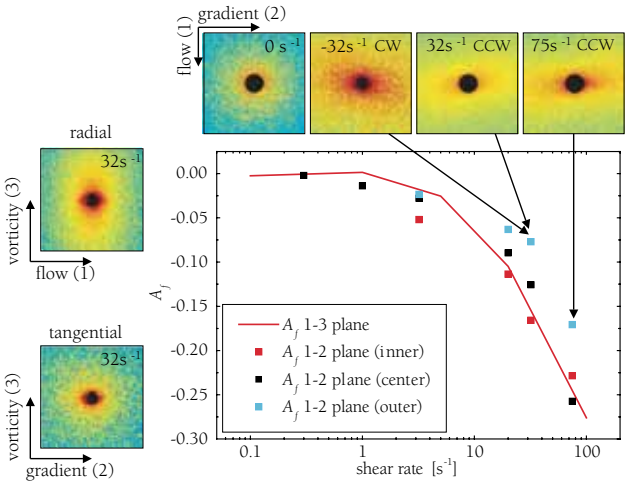

FIGURE 2: Scattering from 40mM EHAC and 300mM NaSal. Top: Scattering images from the **1-2** plane at shear rates 0, -32 s^{-1}, +32 s^{-1} and +75 s^{-1} from left to right. Left: Radial and tangential beam scattering images at 32 s^{-1}. Bottom right: Alignment factors of the radial and **1-2** plane experiments as a function of shear rate. Alignment A_f proceeds from zero at rest toward flow alignment at -1 with increasing shear rate. Beam position within the gap in the **1-2** plane is coded by color.

at 0.5 mm, 1 mm and 1.5 mm from the inner (rotating) wall. A stepper motor could attain shear rates from 0.1 s^{-1} to 100 s^{-1}, where positive shear rates correspond to rotation of the inner cylinder in a counterclockwise sense, looking through the cell toward the detector.

Figure 2 shows data recorded in all three planes of the flow field. The "radial" and "tangential" data were recorded in a conventional Couette cell with the rotation axis perpendicular to the beam. The radial scattering pattern displays a clear anisotropy along the vorticity axis while the tangential beam is isotropic. Hence the micelles are aligned parallel to the flow axis. The data from the **1-2** plane clearly demonstrate that micelles orient with a finite angle (between 0° and 45°) to the flow axis, and flow reversals demonstrate that this orientation changes sign, as expected. Note that data from the **1-2** plane are required to quantify both the degree and the angle of alignment. Indeed, the **1-2** plane SANS results are in quantitative agreement with independent flow birefringence measurements.

Segmental alignment factors A_f, are calculated from the scattering patterns, where $-1 < A_f < 0$ with 0 isotropic and -1 flow-aligned. As shown in Fig. 2, good agreement is observed for the alignment from both rheo-SANS devices, further validating the new **1-2** plane flow cell. However, the gap-resolved **1-2** plane data reveal important new information concerning the micellar structure in the shear banding state. Namely, there is increasing alignment closer to the rotating wall of the shear cell. This is expected as independent flow velocimetry measurements indicate that the shear rate is higher near the inner cylinder as a consequence of the flow kinematics and the shear thinning properties of the micelle solutions [5]. As nominal shear rates in the stress plateau region are probed, distinct bands form. The outer band has a shear rate of approximately 10 s^{-1} to 20 s^{-1}. An inner band exhibiting velocity fluctuations has shear rates higher than the nominal shear rates probed. At the start of the stress plateau, the enhanced degree of segmental alignment near the inner cylinder can be understood as a consequence of the higher local shear rate.

The true advantage of SANS over the other techniques is its ability to resolve microstructural information in the flowing, turbid region corresponding to SIPS. Sector averages oriented parallel and perpendicular to the nematic director are presented in Fig. 3 for two shear rates. At low shear rates no discernible differences in the intensity distributions at different gap positions are observed. At shear rates well into the shear-thinning region, however, the anisotropy and differences between both directions of the flow field and the different gap positions evolve. Most striking is the appearance of a q^{-4} decrease of the intensity at low q, referred to as Porod scattering. This behavior is usually attributed to scattering of a sharp interface and corresponds to fluctuations in scattering length density on length scales longer than the entanglement length of the wormlike micellar network, i.e., microphase separated domains are observed on these length scales in accordance with the observation of optical turbidity at high shear rates.

This study provides new evidence linking shear banding in wormlike micellar solutions to a shear-induced phase separation. Further analysis of these patterns is being undertaken to resolve the microstructure changes during SIPS.

Funding from Unilever and the Alexander von Humboldt Foundation is gratefully acknowledged.

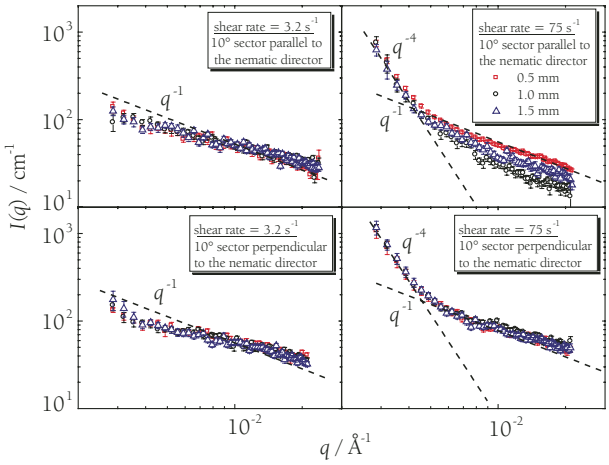

FIGURE 2: Radial intensity distributions in the zero shear plateau (left) and the shear-thinning regime (right) at three different gap positions along and perpendicular to the primary axis of micellar orientation. The q^{-4} regime corresponds to the onset of turbidity at high shear rates.

REFERENCES

[1] H. Rehage and H. Hoffmann, Mol. Phys. **74**, 933 (1991).

[2] M. E. Cates, J. Phys.-Condens. Mat. **8**, 9167 (1996).

[4] Y. T. Hu and A. Lips, J. Rheol., submitted.

[5] M. W. Liberatore, F. Nettesheim, L. Porcar and N. J. Wagner, Phys. Rev. Lett., submitted.

Segregation in Polymer Blend Film Interfaces: Effects of Chain Ends and Node Points

J. S. Lee, N-H. Lee, A. P. Sokolov, R. P. Quirk and M. D. Foster
The University of Akron,
Akron, Ohio 44325

C. F. Majkrzak
NIST Center for Neutron Research
National Institute of Standards and Technology
Gaithersburg, MD 20899-8562

Thin polymer films are finding increasing use as coatings in a variety of settings, including the electronics industry. Fine-tuning of surface properties for these uses, as well as fine tuning of processing behavior, can be accomplished by blending polymers of different architectures, e.g., linear and branched. In this highlight we consider blends in which model polymers of well-defined architecture are used. In general, the composition of an interface of a polymer binary blend film differs from the composition of the bulk because one component is preferred at the interface [1]. Neutron reflectometry (NR) measurements of interfacial segregation in architecturally asymmetric blends of long-branched and linear polystyrene chains allow separation of the influence of the number of chain ends from the influence of the number of node points on interfacial segregation. Complementing the NR measurements with Surface-Enhanced Raman Spectrometry (SERS) measurements strengthens the analysis.

Key to the study was the design and anionic synthesis of two groups of novel, well-defined, highly branched polystyrenes (PS) shown in Fig. 1 [2]. In group I the number of node points in a molecule was varied from 1 to 2 to 4 while the number of ends (branches) was fixed at 6. In group II the number of node points in each molecule was fixed at 4 and the number of ends varied among 6, 9, and 13.

The polydispersities for all polymers were below 1.05 and the overall molecular weight of each polymer was controlled to be about 36 kg/mol to exclude the possibility that interfacial segregation could be driven by molecular weight differences [2]. Films of approximately 950 Å thickness with a 20 % volume fraction branched *h*-PS, blended with *d*-PS (36 kg/mol), were spun cast from solution directly onto clean silicon wafers from which the native oxide had been etched using HF solution. The samples were annealed in high vacuum at 180 °C for 12 h and NR measurements performed on the NG-1 reflectometer.

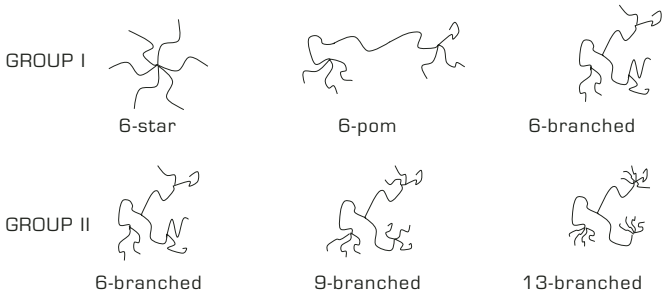

FIGURE 1: Structures of the branched polystyrenes and their abbreviated names. In group I the number of branches is fixed at 6 and the number of node points varied from 1 to 4. In group II the number of branches is varied from 6 to 13 and the number of node points fixed at 4.

Concentration depth profiles of the films were inferred from the NR data by fitting a model depth profile to the experimental reflectivity. An example analysis for the blend with the 6-pom chain is shown in Fig. 2. The composition depth profile (inset in Fig. 2) from fitting the NR data displayed substantial segregation of the pom-pom molecule at both the surface and substrate interfaces. This was observed despite the fact that the isotopic effect favors segregation of the deuterated linear material to the surface.

The strength of the interfacial segregation for the different blends is summarized in Table 1 by reporting the interfacial excess, Γ, given by: $\Gamma = \int_0^{z_c} [\phi(z) - \phi_c] dz$, where $\phi(z)$ is the volume fraction of the hydrogenous component at a depth z for the annealed sample and ϕ_c is the corresponding concentration in the center of the film, z_c. The results for the blend of two linear isotopes quantify the magnitude of the driving force for segregation due to the isotopic difference alone. The linear *d*-PS was enriched at the surface and depleted at the substrate interface. Notwithstanding this fact, in all five blends of linear *d*-PS with branched *h*-PS, the driving force for segregation due to architectural differences is strong enough that the composition of the branched component was enriched at *both* film interfaces. The excess at the surface increased monotonically, but slowly, with the number of node points among the blends in which the number of chain ends (branches) was fixed.

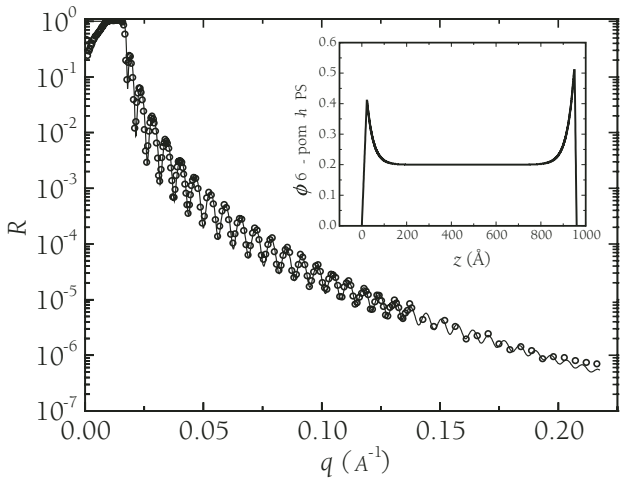

FIGURE 2: Neutron Reflectivity, R, as a function of scattering wavevector, q, for a blend of 20 % volume fraction of 6-pom *h*-PS with linear *d*-PS spun cast onto a Si wafer and annealed for 12 h at 180°C. The solid line in the main graph represents the reflectivity calculated from the model concentration depth profile shown in the inset (note pom-pom concentration at interfaces.)

TABLE 1: Surface and interface excesses of the hydrogenous component in annealed blend films determined by NR

Blend	Surface Excess[a] (Å)	Interface Excess[a] (Å)
Linear *h*-PS/*d*-PS	-2	5
6-star *h*-PS/*d*-PS	6	15
6-pom *h*-PS/*d*-PS	8	12
6-branch *h*-PS/*d*-PS	11	19
9-branch *h*-PS/*d*-PS	22	28
13-branch *h*-PS/*d*-PS	38	29

[a]The uncertainties are ±1 Å.

The excess at the substrate interface behaved quite differently, being roughly twice that at the surface for the blends containing the star and the 6-branch chains, but smaller for the blend containing the 6-pom chain. Both the isotopic effect and architecture effects drive the branched chain to the substrate interface, while at the air surface one driving force counteracts the other.

For the group of three samples in which the number of node points is held constant at 4, the surface excess increases sharply with the number of chain ends, while the excess at the substrate varies little. This observation is consistent with the contention that the number of chain ends plays a bigger role at the substrate interface for which the chemistry of the chain ends is more important. Due to the manner in which in the chains were synthesized, the ends all have butyl initiator fragments and the surface energy of those end groups is somewhat lower than that of a styrene repeat unit. The general overall impression is that the number of node points and precise topology play bigger roles at the substrate interface than at the air interface (surface). The number of chain ends is more important at the air surface than at the substrate interface.

Surface composition (as distinct from surface excess) was probed independently using SERS by thermally evaporating a thin layer of silver onto annealed samples used for NR measurements to enhance the Raman scattering. Using unannealed samples of known composition, the near-surface composition of *h*-PS was related to the ratio of the benzene ring breathing mode SERS peaks for *h*-PS and *d*-PS [3]. Since the strength of the enhanced electric field exciting the Raman scattering dies away exponentially with depth, the composition ratio inferred from a SERS measurement represents a near-surface composition of the *h*-PS component that is a weighted average over a small depth [4]. The compositions of *h*-PS inferred from the SERS measurements are compared to the corresponding compositions inferred from NR in Fig. 3. (The latter were calculated by integrating the NR composition profile over the near-surface region.) As can be seen, the compositions clearly increase with the number of node points and number of chain ends in branched *h*-PS.

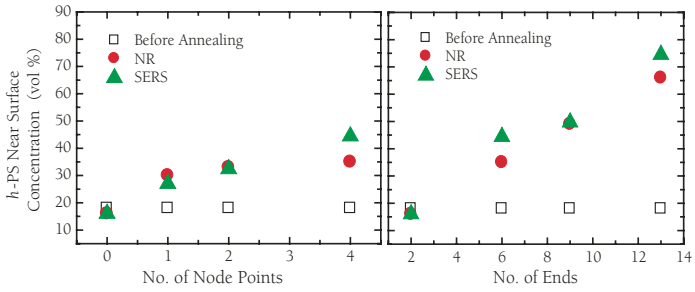

FIGURE 3: Comparison of the variation in surface composition with number of node points and number of chain ends in the hydrogenous component of the blend for unannealed samples measured with NR (open squares), annealed samples measured with NR (circles), and annealed samples measured with SERS (triangles).

In summary, complementary NR and SERS measurements of the segregation at the surface and substrate interface of blends containing well-defined branched polystyrenes demonstrate unambiguously that the strength of the segregation is not simply a function of the number of chain ends, but rather is sensitive to the details of the chain topology. We are currently pursuing a comparison of the experimental results with the theory of Wu and Fredrickson [5].

This research was supported by The American Chemical Society Petroleum Research Fund (#38915-AC7), an Ohio Board of Regents challenge grant, and the Collaborative Center for Polymer Photonics, which is jointly funded by UA, AFRL, and AFOSR.

REFERENCES:

[1] R. A. L. Jones, E. J. Kramer, M. H. Rafailovich, J. Sokolov, S. A. Schwarz, Phys. Rev. Lett. **62** (3), 280 (1989).

[2] J. S. Lee, R. P. Quirk, M. D. Foster, Macromolecules **38** (13), 5381 (2005).

[3] P. P. Hong, F. J. Boerio, S. D. Smith, Macromolecules **27** (2), 596 (1994).

[4] Y. W. Alsmeyer, R. L. McCreery, Anal. Chem. **63** (13), 1289 (1991).

[5] D. Wu, G. Fredrickson, Macromolecules **29** (24), 7919 (1996).

Protein Incorporation in Solid-Supported Model Lipid Membranes

D. J. McGillivray and M. Lösche
Johns Hopkins University,
Baltimore, MD 21218
and
NIST Center for Neutron Research
National Institute of Standards and Technology
Gaithersburg, MD 20899-8562

D. J. Vanderah and J. J. Kasianowicz
Biotechnology Division
National Institute of Standards and Technology
Gaithersburg, MD 20899

G. Valincius
Institute of Biochemistry and
Vilnius Gedimino Technical University
Vilnius, Lithuania

The interaction of proteins with membranes is an important part of many cellular processes, but is poorly understood partly due to the difficulty of producing a biomimetic environment that is suited to comprehensive measurement. Solid-supported lipid membranes provide robust systems, which can be studied using several complementary techniques, including neutron reflectometry – a technique that provides structural information in the sub-molecular size range. Our work, using the CNBT Advanced Neutron Diffractometer / Reflectometer (AND/R), has focused on the optimization and characterization of model systems for the reconstitution of pore-forming membrane proteins. We have produced a synthetically straightforward bilayer membrane system, which is tethered above a gold-substrate and contains a sub-membrane solvent reservoir that is now beginning to be used to probe the details of membrane-active proteins.

Membrane proteins, *i.e.*, proteins that interact with cell membranes or are integral parts of membranes, play an essential part in mediating the relationship between a cell and its surroundings, and display a rich variety of structures and functions. However, a cell membrane is an intrinsically highly disordered system, which relies on this disorder for its physiological functioning, and thus is not well suited to crystallography studies. Furthermore only a small number of membrane-integral proteins have been crystallized and this number is growing much more slowly than for soluble proteins [1]. Solid support allows membranes to be investigated by AFM, ellipsometry, neutron reflectometry, and electrochemical methods including electrical impedance spectroscopy (EIS). These membranes are then a more biologically relevant surrounding in which proteins can be incorporated to gain structure and function information. The solid support also makes systems robust, which enables the development of biosensor applications.

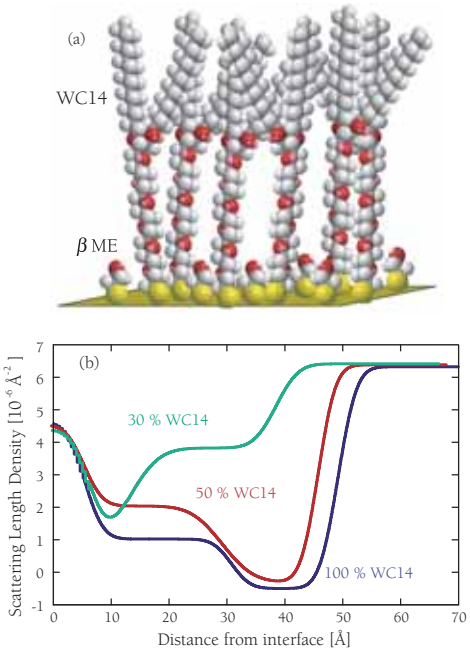

FIGURE 1: a) A cartoon of the surface-supported layer on gold, made up of the artificial lipid WC14 spaced-out on the surface by small β ME molecules. b) Scattering length density profiles derived from reflectometry that show the decreasing amount of WC14 on the surface as its proportion in the SAM-forming solution decreases, with the collapse of the WC14 in sparsely-tethered systems.

The tethered membrane systems in this work are based on a lipid (WC14) synthesized at NIST, in which the two alkyl tails are joined though a glycerol to a thiolated hexa(ethylene oxide) "spacer". This spacer supports the membrane above a gold surface, providing the potential for a sub-membrane solvent reservoir. This is necessary to enable transmembrane proteins to extend beyond the membrane, and helps to reduce the effects of the solid surface on the membrane. Neutron studies on the AND/R, supported by EIS, show that complete membranes can be formed on these tethers using an adaptation of the "rapid solvent exchange" method developed by Cornell *et al.* [2]. Unfortunately, neutron

reflectometry measurements with different solvent contrasts (mixtures of D_2O and H_2O) show that these membranes do *not* contain a solvent reservoir, implying the hexa(ethylene oxide) spacer is filling the sub-membrane space.

To produce a hydrated reservoir, tethering molecules were spaced out on the surface by using small β-mercaptoethanol (βME) molecules in a one-pot self-assembled monolayer (SAM) forming step (Fig. 1). This method decreases the amount of WC14 on the surface, with reflectometry showing the collapse of the synthetic lipid on to the surface as the amount of WC14 in the SAM decreases. A side effect of this reduction in the amount of WC14 is that the surface hydrophobicity is lowered.

It is for these "sparsely-tethered" membrane systems that the rapid-solvent exchange technique is most powerful, as the lower hydrophobicity means that more traditional vesicle-rupture techniques have proven unfruitful. However, using solvent exchange with a variety of completing lipids produces bilayer membranes that EIS shows are electrically sealing, with low capacitance and conductivity. Importantly, we can determine uniquely from the AND/R measurements that there is a distinct hydrated reservoir of about 20 Å under a sparsely-tethered membrane (Fig. 2) [3].

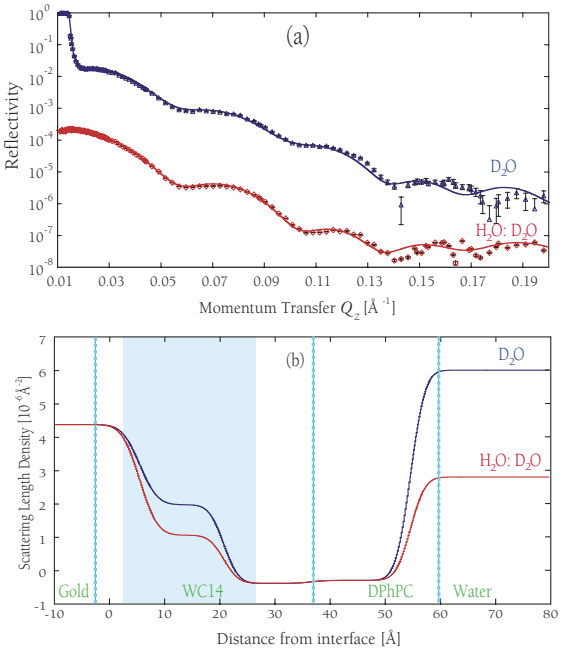

FIGURE 2: (a) AND/R reflectometry measurements on a system made from a 50 % mixture of WC14 and the βME, show that there is water in the WC14 sub-membrane space (shaded in blue) revealed in the changes of the derived SLD profile (b) for the two contrasts.

The membranes produced have been challenged by a membrane-active phospholipase protein, PLA_2. The protein, found in environments as diverse as livers and bee venom, cleaves the acyl-ester bond in the sn-2 position of glycerophospholipids, eventually destabilizing and destroying naturally occurring lipid membranes. PLA is known to be sensitive to the small-scale lateral structure of the membrane, and can therefore be used to probe the fluidity and the nature of defects in the lipid layer [4]. Our results [5] show that although electrochemically and structurally the bilayers formed from diphytanoyl phosphatidylcholine (DPhPC) and palmitoyl oleoyl phosphatidylcholine (POPC) lipids are similar, they react quite differently to the action of PLA_2 (Fig. 3). Although both membranes are quite stable in the presence of PLA_2 without its cofactor Ca^{2+}, once the ions are added the POPC bilayer is rapidly degraded and the DPhPC bilayer remains intact. This result implies that there are still subtle lateral differences between the bilayers formed, emphasizing the complexity of protein interactions with membranes and the necessity of producing a flexible biomimetic system for studying them.

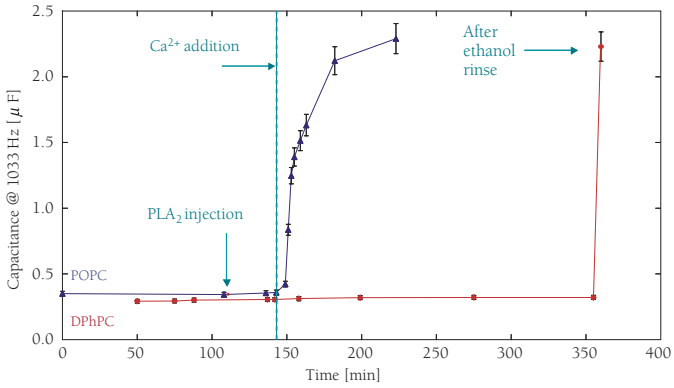

FIGURE 3: Electrical impedance spectroscopy (EIS) capacitance measurements showing the reaction of a bilayer formed from DOPC or DPhPC from a mixture of 70:30 βME:WC14 to a solution of PLA_2.

The tethered bilayer membranes that we have developed, characterized, and optimized show exciting potential as tools to study the structure-function relationships of membrane proteins. Careful manipulation of preparation conditions allows us to produce bilayer membranes which mimic a fully hydrated natural membrane, but which are robust and amenable to measurement with many different techniques, opening the possibility of their development as biosensor templates.

This work was supported by the National Science Foundation under grant #0304062. The CNBT and AND/R are supported by the National Institutes of Health under grant #1 R01 RR14812 and by The Regents of the University of California.

REFERENCES

[1] S. H. White, Protein Science **13**, 1948 (2004).

[2] B. A. Cornell et al., Nature **387**, 580 (1997).

[3] Submitted to JACS.

[4] K. Jørgensen, J. Davidsen, O. G. Mouritsen, FEBS Letters **531**, 23 (2002).

[5] Submitted to Langmuir.

Polyunsaturated Lipids: Neutrons Complete the Story ...

M. Mihailescu
University of California at Irvine
Irvine, CA 92697
and
NIST Center for Neutron Research
National Institutes of Standards and Technology
Gaithersburg, MD 20899-8562

K. Gawrisch
National Institute on Alcohol Abuse
and Alcoholism
National Institutes of Health,
Bethesda, MD 20892

The essential role of highly unsaturated fatty acids for human health, in particular for brain development and function, has been well established [1]. The membranes of brain synapses and of the retina may contain up to 50 mol % docosahexaenoic acid (DHA, 22:6n3) as hydrocarbon chains. DHA is a polyunsaturated, ω-3 fatty acid with 22 carbons and six double bonds. Reconstitution experiments with rhodopsin have shown that high concentrations of DHA are essential to achieve levels of rhodopsin activation by light that are similar to levels in rod outer segment disk membranes of the retina [2]. The efficiency of GTP-binding protein (G-protein) coupling to the photoactivated rhodopsin depends on membrane DHA content as well [3]. Rhodopsin belongs to the family of G-protein coupled membrane receptors (GPCR) that transmit extracellular signals elicited by compounds like neural transmitters, hormones, odorants, or light to the interior of cells where they activate G-proteins. This large superfamily of heptahelical receptors comprises receptors for dopamine, serotonin, epinephrine, opioids, and cannabinoids, just to mention a few. It is likely that other synaptosomal GPCR have a specific requirement for high concentrations of DHA for proper function as well.

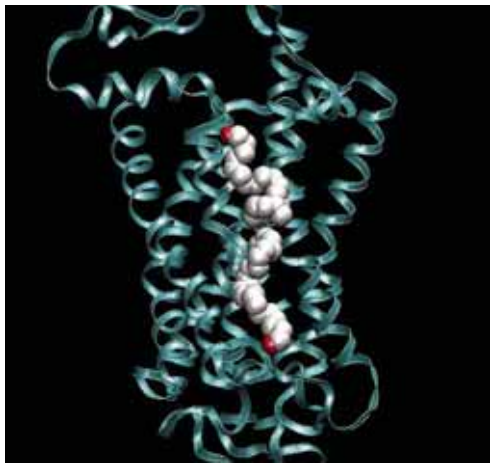

FIGURE 1: Snapshot from an MD simulation of rhodopsin in a polyunsaturated 18:0-22:6n3-PC (phosphatidylcholine) bilayer [4]. The protein backbone is given as a ribbon representation while two DHA chains are shown as spheres.

The mechanisms by which polyunsaturated lipid species may influence biological function at the molecular level are now attracting considerable attention. Recent data from NMR, x-ray diffraction, and molecular simulations studies on polyunsaturated lipids indicate that polyunsaturated chains themselves are exceptionally flexible and perform very rapid conformational transitions [5]. This is contrary to the image perceived in the past that polyunsaturated hydrocarbon chains perturb membrane properties because of their bulkiness and rigidity. One hypothesis is that polyunsaturated hydrocarbon chains alter membrane elastic properties that are critical for protein activation by ligands. According to the model, membranes rich in polyunsaturated lipids are under considerable curvature elastic stress that is partially released when the receptor protein changes its shape upon activation. The curvature stress in polyunsaturated

lipid membranes stems from an uneven density distribution of saturated and polyunsaturated hydrocarbon chains over the hydrophobic core of lipid bilayers. There is indirect evidence that the density of DHA chains is higher near the lipid water interface, while the density of saturated chains is higher in the bilayer center [5].

This hypothesis was confirmed in a series of neutron diffraction experiments on DHA-containing oriented multilayers at the Advanced Neutron Diffractometer /Reflectometer [6] that was recently installed at the NIST Center for Neutron Research. The phosphatidylcholine 18:0-22:6n3-PC (see Fig. 1) was labeled selectively in the saturated stearic acid (18:0) chain or the polyunsaturated DHA (22:6n3) chain.

Figure 2a presents the diffraction data for such a series of multilamellar samples, measured at 66 % relative humidity corresponding to 6.1 water molecules per lipid.

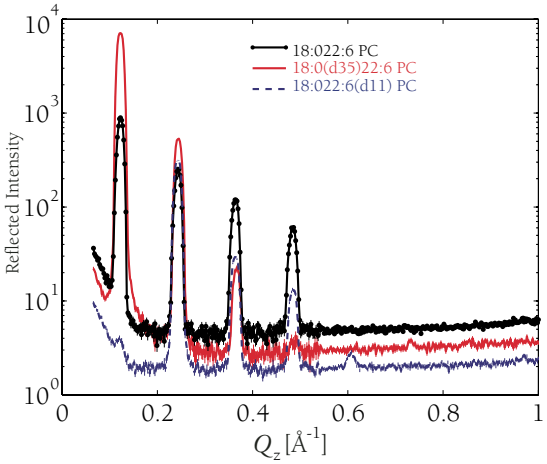

FIGURE 2a: Diffraction data of 18:0-22:6-PC oriented multilayers, with protonated hydrocarbon chains (black), with deuterated stearoyl chains (red), or with deuterated DHA chains (blue).

By a Fourier synthesis of the coherent diffraction signal in reciprocal space, the density profiles of saturated 18:0 and polyunsaturated 22:6 chains, in projection along the normal of the bilayer, as well as the water distribution were determined (Fig. 2b). The results show clearly that the chain density of the polyunsaturated DHA (blue trace) extends further into the lipid water interface. Also, DHA density is higher near the interface than in the bilayer center. In contrast, the density of saturated chain segments is higher in the bilayer center. Such uneven distribution of chain densities is likely to alter the lateral pressure profile of bilayers that has been linked to changes in the GPCR free energy upon conversion to the activated state [7]. It is important to mention that the experiments above were conducted in the biologically relevant liquid-crystalline state of lipid bilayers.

Neutron diffraction proves itself as an increasingly important method for structural investigations of biological matter. Advancements in neutron techniques, combined with the increased availability of specifically

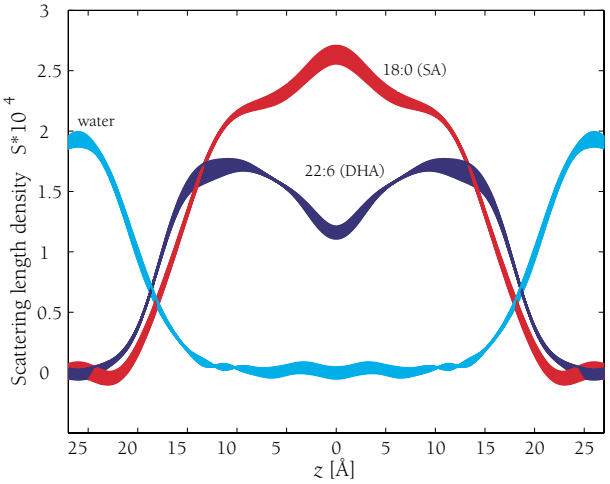

FIGURE 2b: The individual chain and water distributions within the bilayer, at 66 % relative humidity. The density profiles, shown here with their uncertainty bands, are on an absolute scale [8] up to a multiplicative unknown constant S, accounting for the area per lipid.

deuterated biological material, enable structural studies at the molecular level with unprecedented resolution. The power of neutron diffraction studies unfolds particularly well if the results are combined with spectroscopic approaches like NMR and molecular simulations, as is the case in this project.

ACKNOWLEDGMENTS

The AND/R, constructed by the Cold Neutrons for Biology and Technology (CNBT) partnership, is supported by the National Institutes of Health under grant #1 R01 RR14812 and by The Regents of the University of California.

REFERENCES:

[1] N. Salem, Jr., B. J. Litman, H. Y. Kim, and K. Gawrisch, Lipids **36**, 945 (2001).

[2] B.J. Litman, S. L. Niu, A. Polozova, and D.C. Mitchell, J. Mol. Neurosci. **16**, 237 (2001).

[3] S. L. Niu, D. C. Mitchell, S. Y. Lim, Z. M. Wen, H. Y. Kim, N. Salem, Jr. and B. J. Litman, J. Biol. Chem. **279**, 31098 (2004).

[4] S. E. Feller, K. Gawrisch, T. B. Woolf, J. Am. Chem. Soc. **125**, 4434 (2003).

[5] N. V. Eldho, S. E. Feller, S. Tristram-Nagle, I. V. Polozov, and K. Gawrisch, J. Am. Chem. Soc. **125**, 6409 (2003).

[6] http://www.ncnr.nist.gov/programs/reflect/ANDR

[7] R. S. Cantor, Biophys. J. **76**, 2625 (1999).

[8] M. C. Wiener, and S. H. White, Biophys. J. **59**, 162 (1991).

Methyl Dynamics as a Probe of Protein Structure and Function

J. E. Curtis and D. A. Neumann
NIST Center for Neutron Research
National Institute of Standards and Technology
Gaithersburg, MD 20899-8562

A. McAuley
Amgen Incorporated
Thousand Oaks, CA 91320-1799

D. J. Tobias
University of California, Irvine
Irvine, CA 92697-2025

J. H. Roh and A. P. Sokolov
The University of Akron
Akron, OH 44325-3909

The pharmaceutical industry increasingly depends on the ability to store proteins without degradation, and relies on increasing understanding of protein function in the design of medications. Using an approach combining neutron spectroscopy with molecular dynamics simulations, we highlight recent results addressing these issues by characterizing protein dynamics via their non-exchangeable protons. In particular, the dynamics of methyl group protons is distinct and apparently separable from other aliphatic protons, and because methyl groups are numerous and strategically distributed they can be used as a powerful probe of protein structure and function. Regarding stability, the onset of anharmonic behavior is found to depend on the level of hydration. We have also found both a lower temperature hydration-independent activation regime, and a higher temperature hydration-dependent regime that is directly related to the onset of biological activity in enzymes.

Proteins are ubiquitous high molecular weight heterogeneous polymers that, beside their obvious importance in nature, are now a major fraction of all drugs manufactured in the world [1]. Only a few techniques exist that can even crudely probe protein structure and dynamics in the amorphous state. Fortunately, neutron scattering is proving to be a powerful method to quantitatively measure proteins in native and non-native environments. Molecular dynamics computer simulations, when carried out in concert with high-resolution neutron scattering experiments, can provide a detailed microscopic interpretation to macroscopic observables. This is possible since both time (fs to ns) and length (Å to nm) scales of computer simulation and neutron spectroscopy overlap thus allowing for the validation of simulation methodologies and force field parameters. We are applying a combined experimental and computational effort to understand the factors leading to the activation of dynamical modes in proteins.

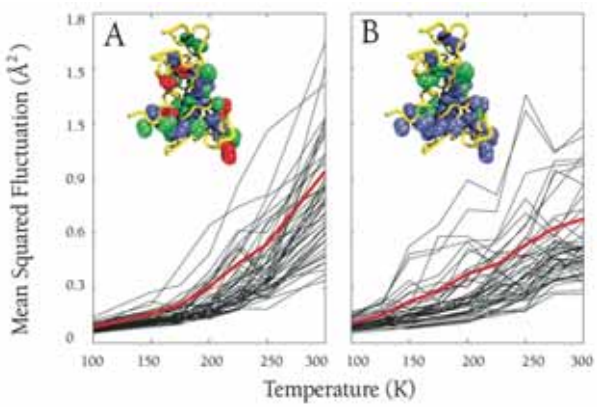

FIGURE 1: MSFs of methyl protons from MD simulations of RNase plotted separately for each methyl group: (A) hydrated (crystal), (B) dehydrated (powder). The thick red lines are averages. Insets show the crystal structure with methyl groups colored by MSF values at 300 K (> 1.4 Å^2, red; 0.7-1.4 Å^2, green; < 0.7 Å^2, blue).

As the temperature is raised above about 200 K, hydrated proteins undergo a change in dynamics, the so-called dynamical transition, from glasslike, in which the motion is primarily vibrational, to liquidlike, in which transitions between taxonomic substates are possible. The extent to which the solvent affects protein dynamics has implications for fundamental studies aimed at elucidating the role of specific protein motions in protein function and their practical application to biopreservation by maintenance of protein function and suppression of degradation pathways. We have studied the role of hydration on the dynamics of methyl groups in the protein ribonuclease A (RNase), in both hydrated and dehydrated powders via validated molecular dynamics simulations. The temperature dependence of the mean square fluctuations (MSFs) of individual methyl groups in a hydrated RNase and dehydrated RNase powder is shown in Fig. 1. In the hydrated system, the MSFs generally increase linearly with temperature below the dynamical transition temperature of approximately 200 K, and a majority show an abrupt increase with temperature above 200 K. In contrast, in the dehydrated system, the MSFs

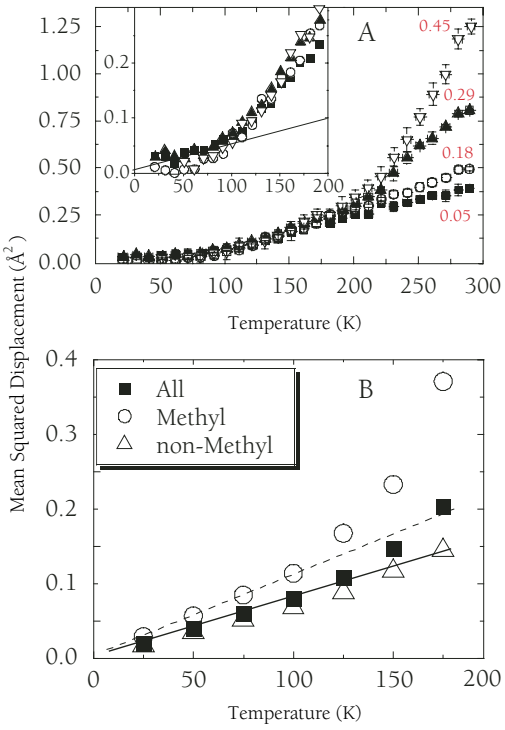

FIGURE 2: Mean square displacement ($\langle x^2 \rangle$) versus temperature for lysozyme at various hydration levels (*h*: ■ 0.05; ○ 0.18; ▲ 0.29; ▽ 0.45) measured using the HFBS. The inset shows low temperature onset of anharmonicity at temperatures between 100 K to 120 K. (B) Simulated $\langle x^2 \rangle$ for all non-exchangeable protons, methyl protons and non-methyl protons in dehydrated lysozyme. Harmonic behavior is shown as a linear extrapolation from low-temperature data for all protons (solid line) and for methyl protons (dashed line).

generally follow a roughly linear increase over the entire temperature range and, on average, do not undergo a dynamical transition. As shown in the inset of Fig. 1, we find that the dynamical transition exhibited by the methyl groups occurs throughout the hydrated protein at roughly the same temperature (about 200 K for most methyl groups), albeit with a slight dependence on sequence but not on solvent accessibility. The transition is suppressed throughout most of the protein in the absence of solvent. Our study provides direct evidence that both the amplitudes and distribution of motion above 200 K are influenced by solvent and are not exclusively an intrinsic property of the protein.

We have studied the hydration dependence of the dynamics of non-exchangeable protons in the protein lysozyme over a wider temperature range by elastic and inelastic neutron scattering using the High Flux Backscattering Spectrometer (HFBS) at NIST. In this study we have found two temperature regions where the onset of anharmonicity in the dynamics occurs as shown in Fig. 2. The first occurs at low temperature, approximately 100 K, and is not dependent on hydration level. Through analysis of the experimental data and characterization by moleculear dynamics simulations we have found that the low temperature anharmonicity is dominated by methyl group protons (Fig. 2B). The second, well-known, dynamical transition at about 200 K appears only in samples with a hydration level (h) greater than 0.2 grams water per gram of protein (h > 0.2). After correcting for methyl group contributions, variations of the neutron spectra with hydration have been correlated with variations in catalytic activity of the protein (Fig. 3). These results indicate that the relaxation processes that are activated above near 200 K at sufficient hydration levels (h > 0.2) are directly related to the onset of biological activity in enzymes. Water acts as a plasticizer by allowing for the activation of protein motions by decreasing the local viscosity of the protein atoms.

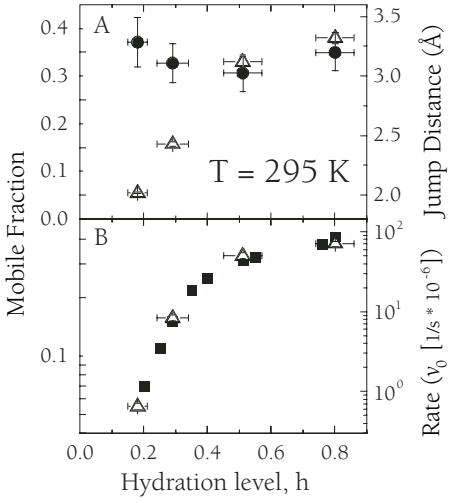

FIGURE 3: The correlation of protein secondary relaxation with function. (A) Mobile fraction (△) and jump distance (●) of the slow process as a function of hydration level. (B) mobile fraction (△) of the slow process and the initial rate of the lysozyme-catalyzed reaction, v_0, (■) as a function of hydration level.

Since methyl protons comprise a significant fraction of non-exchangeable protons in proteins (e.g. 26 % in lysozyme) and the properties of methyl dynamics appear to be separable from other non-exchangeable protons, they are a unique atomic probe of protein relaxation and functional dynamical modes. In addition to the discrimination of the role of methyl groups in the secondary relaxation processes as discussed above, we have found by simulation studies of lysozyme that the atoms that are activated at the low-temperature onset of anharmonicty (approximately 100 K) are all directly adjacent to the active site of the protein. Thus, the low-T activated process could be a general property of enzymes that represents the inherent and required flexibility of atoms in the functionally relevant region of the biomolecule. We are continuing our efforts to use partial deuteration both in simulations and in the future experiments, to study the connection between specific dynamical motions and protein function. The inherent dynamical character of methyl dynamics within proteins could also be used to elucidate minor structural changes in amorphous formulations of protein pharmaceuticals.

REFERENCES

[1] C. J. Roberts and P. G. Debenedetti, AIChE J. **48**, 1140 (2002).

[2] J. E. Curtis, M. Tarek, and D. J. Tobias, J. Am. Chem. Soc. **126**, 15928 (2004).

[3] J. H. Roh, V. N. Novikov, R. B. Gregory, J. E. Curtis, Z. Chowdhuri, and A. P. Sokolov, Phys. Rev. Lett. **95**, 038101 (2005).

Testing Time-Reversal Symmetry in Neutron Beta Decay

H. P. Mumm, M. S. Dewey, J. S. Nico, and A. K. Thompson
NIST Center for Neutron Research
National Institute of Standards and Technology
Gaithersburg, MD, 20899-8461

A. Garcia and J. F. Wilkerson
University of Washington
Seattle, WA 98195

S. J. Freedman, B. K. Fujikawa
University of California at Berkeley
and Lawrence Berkeley National Laboratory
Berkeley, CA 94720

T. E. Chupp and R. L. Cooper
University of Michigan
Ann Arbor, MI, 48104

C. A.Trull and F. E. Wietfeldt
Tulane University
New Orleans, LA 70118

G. L. Jones
Hamilton College
Clinton, NY 13323

The emiT experiment tests time-reversal symmetry in the beta decay of polarized free neutrons by searching for the time-reversal-odd, parity-even triple correlation between the neutron spin and momenta of both the electron and proton. The detection of this correlation above the small calculable effect due to final state interactions would be a direct indication of time-reversal symmetry violation. A highly successful second run of the emiT experiment was recently completed at the NIST Center for Neutron Research. Analysis of this greatly improved data set is currently in progress.

Charge-parity symmetry violation (CP violation) beyond that incorporated within the Standard Model of particle physics is a natural outcome of attempts to explain the dominance of matter over anti-matter in the universe. Surprisingly, no such violation has yet been observed. CP and time-reversal (T) violation can be related to each other through the charge-parity-time (CPT) theorem, so that tests of direct T violation should also help to illuminate this puzzle. Experimental limits on both neutron and atomic electric dipole moments (T-violating) place strict constraints on some, but not all, possible sources of new CP violation. Tests of nuclear beta decay, and neutron decay in particular, complement these EDM experiments. Some theoretical models that extend the Standard Model, such as left-right symmetric theories, lepto-quarks, and certain exotic fermions could cause observable effects that are as large as the present experimental limits [1].

The decay probability distribution for neutron beta decay dW, written in terms of the neutron spin direction $\hat{\sigma}_n$ and the momenta (energy) of the electron $\mathbf{p}_e$ (E_e) and antineutrino $\mathbf{p}_\nu$ (E_ν) was first described by Jackson, Trieman, and Wyld in 1957 [2].

$$dW \propto \left(1 + a\frac{\mathbf{p}_e \cdot \mathbf{p}_\nu}{E_e E_\nu} + A\frac{\hat{\sigma}_n \cdot \mathbf{p}_e}{E_e} + B\frac{\hat{\sigma}_n \cdot \mathbf{p}_\nu}{E_\nu} + D\frac{\hat{\sigma}_n \cdot \mathbf{p}_e \times \mathbf{p}_\nu}{E_e E_\nu}\right) dE_e\, d\Omega_e\, d\Omega_\nu .$$

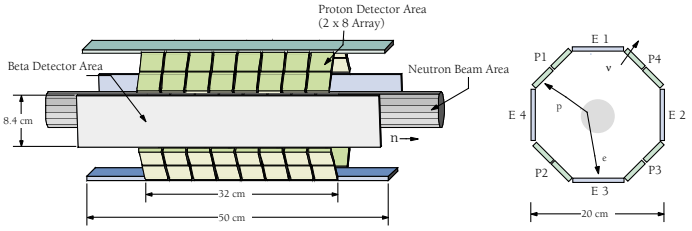

FIGURE 1: Schematic diagram of the emiT detector.

The triple correlation D is T-odd. A non-zero value for D above the level of calculable final state interactions implies a violation of time-reversal symmetry. The most sensitive measurement of D in ^{19}Ne decay is $(1 \pm 6) \times 10^{-4}$ [3], only about a factor of three above electromagnetic final state effects. The most recent measurements of D in neutron decay, $(-2.8 \pm 7.1) \times 10^{-4}$ and $(-6 \pm 13) \times 10^{-4}$ come from the TRINE collaboration and the first run of the emiT experiment respectively [4,5]. Standard Model final state effects in the neutron system are estimated to be approximately 1.3×10^{-5}, well below the sensitivity of current experiments [6]. Recently, using an extensively upgraded detector, the emiT collaboration completed a second, more sensitive measurement.

The emiT detector consists of an octagonal array of four electron and four proton detectors concentric to a beam of longitudinally polarized neutrons. The proton detectors are arrays of solid state diode detectors while the beta detectors are rectangular slabs of plastic scintillator. The detector configuration is shown schematically in Fig. 1. Decays are detected as a coincidence between an electron and a proton. Because the proton endpoint energy is 750 eV, it is much slower than the electron, and a delayed coincidence can be used to reject most backgrounds. This is shown in Fig. 2.

Monte Carlo evaluation of various detector arrangements led to a detector geometry that is simultaneously optimized for sensitivity to the D-coefficient and insensitivity to most systematic effects. The highly symmetric and segmented arrangement allows for the approximate cancellation of systematic effects stemming from detector efficiency and solid angle variations as well as from beam and polarization misalignment. Additional cancellations are

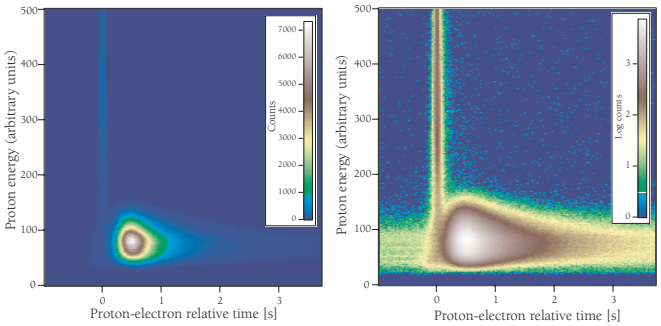

FIGURE 2: Surface barrier-scintillator coincidence data from a typical four hour run showing proton energy vs delay time. Prompt coincidence events at T = 0 are primarily beam related events. The very low backgrounds are also readily apparent in the log plot.

attained by reversing the direction of the neutron polarization during the measurement. Consequently, the emiT experiment is performed by periodically reversing the polarity of the neutron spin and then comparing the number of coincidence events with opposite signs of the triple correlation in otherwise identical coincidence pairs of proton and electron detectors. Using this approach, one can construct a ratio of the number of coincidence events in which all the factors in the numerator favor events with one sign of the triple correlation and those in the denominator favor the opposite sign. For example, the ratio for the geometry shown in Fig. 1 would be,

$$R = \frac{N^{\uparrow}_{e1p3} N^{\uparrow}_{e2p4} N^{\uparrow}_{e3p1} N^{\uparrow}_{e1p3} N^{\downarrow}_{e1p2} N^{\downarrow}_{e2p3} N^{\downarrow}_{e3p4} N^{\downarrow}_{e4p1}}{N^{\uparrow}_{e1p2} N^{\uparrow}_{e2p3} N^{\uparrow}_{e3p4} N^{\uparrow}_{e4p1} N^{\downarrow}_{e1p3} N^{\downarrow}_{e2p4} N^{\downarrow}_{e3p1} N^{\downarrow}_{e1p3}},$$

where the N's are the number of events seen in the indicated detector pair. Each factor can be written as,

$$N^{\uparrow(\downarrow)}_{eipj} = C^{\uparrow(\downarrow)}\ \Omega^{\uparrow(\downarrow)}_{ei}\ \Omega^{\uparrow(\downarrow)}_{pj}\ \varepsilon^{\uparrow(\downarrow)}_{ej}\varepsilon^{\uparrow(\downarrow)}_{pj}\varepsilon^{\uparrow(\downarrow)}_{eipj}\,(1\pm\vec{K}\bullet\vec{P}D),$$

where C is proportional to beam fluence in the indicated polarization, the Ω are the relevant solid angles, the ε are the individual detector efficiencies, and ε_{ep} is the correlated portion of the detection efficiency. $\vec{K}$ is an instrumental constant determined using a Monte Carlo simulation (note that it multiplies D and therefore cannot lead to a false effect), and $\vec{P}$ is the polarization vector. From the equations one can see that the individual detector efficiencies and solid angles cancel in R and it is straightforward to solve for D.

While the correlated detection efficiencies nearly cancel, precise alignment of the beam axis, the detector axis, and the magnetic field is critical to minimizing systematic effects stemming from this term. A misalignment between the detector axis and the neutron spin axis, for example, can mimic a time-reversal violating signal if the beam is not centered in the detector. This false signal (henceforth called the Asymmetric Transverse Polarization (ATP) effect) is due to a combination of the beta and neutrino asymmetries (A and B), solid angle, and decay kinematics. To reduce systematic effects to acceptable levels, both the detector and the field are aligned to the beam line to within a few milliradians.

The ATP effect is considered to be the largest systematic uncertainty in the experiment. Other systematic effects, such as variations in flux, polarization, and spin flip frequency (even in the case that they are dependent on the state of the spin-flipper), can be shown to produce an asymmetry proportional to D and cannot produce a false effect. To fully understand the size of a potential ATP effect, the neutron beam polarization and beam profile were measured during construction of the emiT beam line. The polarization was measured in a straightforward way using a second polarizer similar to the first, and the spin flipper, and beam images were obtained at three locations along the beam line to provide detailed information on the beam envelope. In addition to these measurements, the alignment of the magnetic guide field was monitored continuously during the run with two triple-axis magnetometers.

Although these measurements in combination with Monte Carlo simulations of the detector indicate that the ATP effect was well under control, it is also possible to make *in situ* measurements of this systematic effect. Periodically during data collection the neutron-spin guide field was rotated to point directly at one of the proton detectors. This results in an *oscillation* in the number of coincidence events observed as a function of proton detector because of the A and B correlations (the direction of the electron is anti-correlated with the neutron spin). By observing the size of the ATP effect in this situation and scaling down to the measured misalignment, one can obtain a very good estimate of this systematic uncertainty. Finally, it is possible to use the data itself as a magnetometer. By measuring this *oscillation* as a function of detector number for the normal runs one can, in effect, measure the misalignment of the magnetic field. This measured misalignment can be used to scale the ATP runs and tightly constrain the size of the ATP effect. Initial estimates indicate that the ATP effect is on the order of 2×10^{-5}, well below the statistical sensitivity of the experiment.

We have presented a brief overview of the second run of the emiT experiment. Further details can be found in Ref. 7. The improvements made to the apparatus after the first run (in particular to the proton detection system and the data acquisition system) were very successful. As a result, nearly 24 times as many coincident events were collected in a similar amount of run time. Not only were more data collected, but they were of much higher quality; the signal to noise was improved from about 2.5-to-1 to approximately 100-to-1. In addition, a more thorough characterization of all the systematic uncertainties was carried out. We have shown that the largest of these will be below 1×10^{-4}, which is below our expected statistical sensitivity of 2×10^{-4}. If this sensitivity is reached, this measurement will be the most precise test of time reversal invariance in beta decay to date. If the analysis yields a non-zero D, it will be an unambiguous sign of physics beyond the Standard Model.

REFERENCES

[1] P. Herczeg, in Proc. of the 6th Int. PASCOS-98, World. Sci., Singapore, (1998).

[2] J. D. Jackson, S. B. Treiman, and H. W. Wyld,Jr., Phys. Rev. **106**, 517 (1957).

[3] F. P. Calaprice, Hyperfine Interactions, **22**, 83, (1985).

[4] T. Soldner et al, Phys. Lett. B, **581**, 49 (2004).

[5] L. J. Lising et al., Phys. Rev. C, **62**, 055501 (2000).

[6] C. G. Callan and S. B. Treiman, Phys. Rev. **162**, 1494 (1967).

[7] H. P. Mumm et al., Rev. Sci. Instrum. **75**, 5343 (2004).

Field-Dependent Magnetic Domain Walls in Exchange-Biased GdFe/TbFe Bilayers

T. Hauet and S. Mangin
LPM, University H. Poincare -Nancy I
B.P 239 F-54506 Vandoeuvre cedex, France

P. Mangin
Laboratoire Leon Brillouin (LLB)
UMR 12 CEA/CNRS Bat. 563 CEA Saclay
Gif sur Yvette, France

J. A. Borchers
NIST Center for Neutron Research
National Institute of Standards and Technology
Gaithersburg, MD 20899-8562

Exchange biasing has been widely studied in ferromagnetic/antiferromagnetic (FM/AFM) bilayers [1] and is essential for the operation of magneto-electronic devices, such as read heads in computer hard drives. This phenomenon is characterized by a shift of the magnetic hysteresis loop by an amount known as the exchange field, H_E, after field cooling. In some systems it has been shown that the exchange coupling at the interface is antiferromagnetic and that H_E can change from positive to negative values depending on the magnitude of the cooling field [2]. Theoretical models for this behavior predict the formation of domain walls in either the FM or AFM layer [1,2]. Here we describe a system in which exchange bias is the direct result of a frozen interface domain wall, revealed by polarized neutron reflectivity (PNR), whose width depends on the cooling field.

GdFe/TbFe ferrimagnetic bilayers are ideal for studying magnetic configurations in exchange-biased bilayers [3] because their magnetic behavior mimics that of typical FM/AFM biased layers. In our sample Glass/$Gd_{40}Fe_{60}$(100 nm)/$Tb_{12}Fe_{88}$(50 nm)/Al(4.5 nm)/Al_2O_3(3.5 nm) grown by evaporation, both $Gd_{40}Fe_{60}$ and $Tb_{12}Fe_{88}$ are amorphous ferrimagnets in which the Fe and rare-earth magnetic moments are antiferromagnetically coupled. In $Tb_{12}Fe_{88}$, the iron contribution to the magnetization is dominant, and the net magnetization of the alloy points antiparallel to the terbium spins. $Tb_{12}Fe_{88}$ is a soft magnetic material (i.e., it has a small coercive field) at room temperature but becomes hard upon cooling. In $Gd_{40}Fe_{60}$, the contribution from the Gd is dominant, and the net magnetization is parallel to the Gd spins. GdFe is a soft magnetic material at all temperatures.

Analogous to classic exchange-spring magnets [4], the competition among the anisotropies, interlayer exchange coupling and Zeeman energies in our GdFe/TbFe bilayer gives rise to a rich magnetic phase diagram in which spin-twists form near the interface. PNR is ideally suited for imaging vertical domain walls in ferromagnetic and ferrimagnetic multilayers [4], as it provides a depth profile of both the sample structure and the vector magnetization. PNR measurements were performed at the NG-1 reflectometer with the neutron polarization direction and the applied field maintained parallel to the TbFe uniaxial anisotropy direction in the sample plane. Polarization efficiencies exceeded 96 %. Depth-dependent magnetic and structural properties were deduced by fitting the PNR data with a model for the scattering length density that includes the possibility for a smooth magnetic twist in either the GdFe or TbFe layer [4]. While the fits were quite sensitive to the magnetization of the entire TbFe layer as well as the GdFe magnetization close to the TbFe/GdFe interface, they were much less sensitive to GdFe moments closest to the glass substrate due to the large Gd absorption.

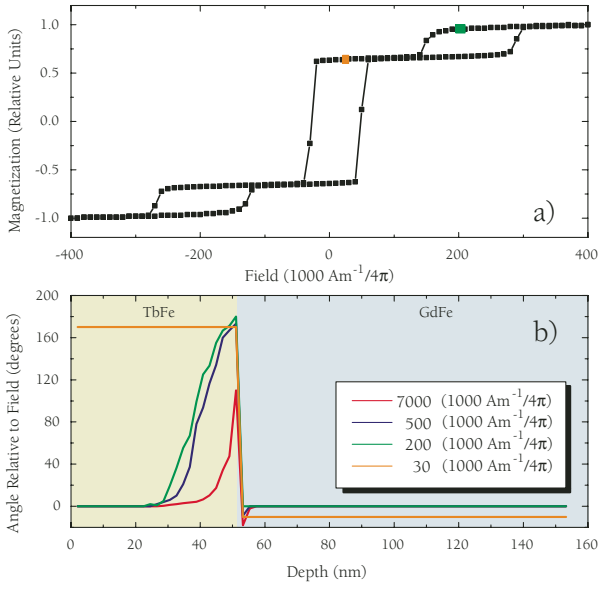

FIGURE 1: a) Magnetization as a function of field for the GdFe/TbFe bilayer at 300 K. b) Depth profile of the angle between the bilayer magnetization and the positive field direction (0°) obtained from fits to PNR data.

In Fig. 1a the magnetization is plotted as a function of field for the GdFe/TbFe sample at 300 K. Figure 1b shows the corresponding depth profile of the moment angle obtained from fits to the PNR measurements (not shown). For fields larger than 1.19×10^4 A/m (Note: 1000 $Am^{-1}/4\pi$ = 79.58 A/m = 1 Oe), an interface domain wall (IDW) forms in the soft TbFe. In fields smaller than 1.19×10^4 A/m, the IDW is annihilated, and the TbFe magnetization is fully reversed relative to the applied field. In general, the IDW allows for (nearly) antiparallel alignment of the GdFe and TbFe moments at the interface and for parallel alignment of the remaining GdFe and TbFe moments relative to the applied field. The thickness of the IDW decreases as the field increases.

As a next step we cooled the sample to 15 K in different fields in order to freeze the IDW's (Fig. 1b) and to probe IDW influence on the reversal of the GdFe magnetization. The field was cycled between 1.59×10^4 A/m and -1.59×10^4 A/m in order to flip only the soft GdFe, and not the TbFe. H_E of the resultant hysteresis loops exhibits a pronounced dependence upon the cooling field, H_{cf}. For example, H_E increases from -6.4×10^3 A/m to 7.9×10^3 A/m with H_{cf}, and H_E crosses zero at H_{cf} = 4.0×10^4 A/m [3].

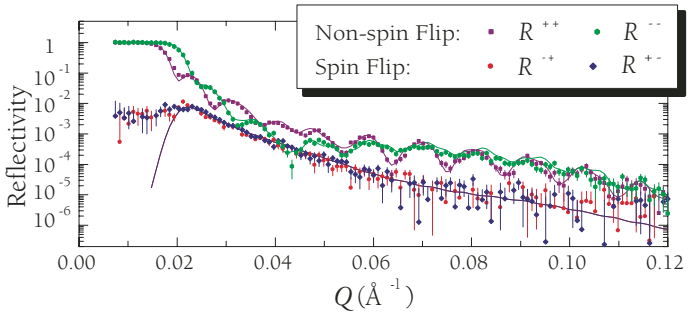

FIGURE 2: PNR spectra obtained in a field of 1.59×10^4 A/m after cooling the GdFe/TbFe sample from 300 K to 15 K in a 5.6×10^5 A/m field.

To best exemplify the relationship between the exchange field H_E, the cooling field H_{cf}, and the frozen TbFe spin configuration, we contrast here PNR results obtained after cooling in fields of 5.6×10^5 A/m and 1.59×10^4 A/m, which give rise to negative and positive bias fields (H_E = 4.0×10^3 A/m and -6.4×10^3 A/m) respectively. Figure 2 shows the PNR spectra and fit measured in 1.59×10^4 A/m after field cooling in 5.6×10^5 A/m. The fit indicates that a shallow IDW, with approximate thickness of 15 nm, is present in the TbFe layer (Fig. 3a). We note that the magnetic structure of the TbFe layer is frozen and nearly matches the one determined at 300 K (shown in Fig. 1b), as expected [3]. The TbFe interface moment is not parallel to its anisotropy axis, but is oriented at an energetically unfavorable angle of 110° relative to the positive field direction and thus gives rise to a positive biasing field. Upon reversing the GdFe magnetization in a field of -1.59×10^4 A/m, the small IDW in the TbFe layer vanishes and the TbFe interface moment realigns parallel to its anisotropy axis (Fig. 3a). The TbFe and GdFe moments are antiparallel at the interface (and throughout the entire layer) with the TbFe moments along the field at 0° and the GdFe moments opposite the field at 180°.

In contrast, fits to the PNR data obtained after cooling in H_{cf} = 1.59×10^4 A/m reveal that a larger IDW approximately 30 nm

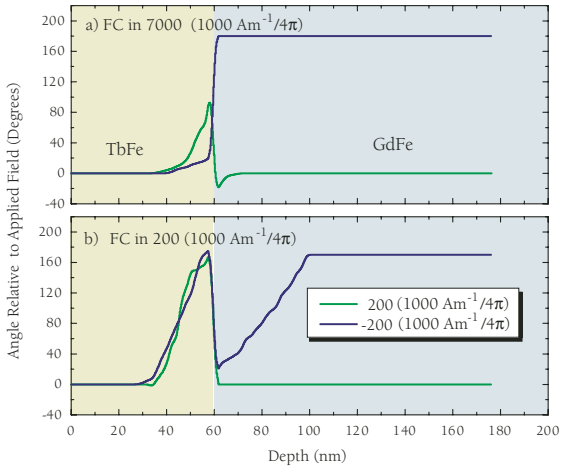

FIGURE 3: a) Depth profile of the angle between the magnetization and the positive field obtained from fits to PNR data for different applied fields after cooling in 5.6×10^5 A/m. b) Depth profile of the angle of the magnetization after cooling in 1.59×10^4 A/m.

thick (Fig. 3b) is frozen inside the TbFe layer and the TbFe interface moment is aligned *antiparallel* to the applied field at 180°. Since this TbFe configuration favors full alignment of the GdFe moment parallel to the positive field direction at 0°, a domain wall is forced into the GdFe layer when the field is reversed below H_E = -6.4×10^3 A/m. The spin structure in the reverse field involves two IDW's (Fig. 3b), and the interfacial GdFe and TbFe moments are oriented completely opposite to their directions in the H_{cf} = 5.6×10^5 A/m state (Fig. 3a).

Overall, the PNR measurements of TbFe/GdFe bilayers confirm that an interface domain wall, mainly located in the TbFe layer, freezes upon field cooling. PNR results also reveal that the orientation of the TbFe magnetization at the interface, as well as the thickness of the frozen IDW, is directly correlated with the magnitude and sign of H_E measured by bulk techniques. We further note that the cooling-field dependence of the TbFe interfacial angle obtained from PNR fits approximately matches theoretical predictions [5]. PNR thus provides direct access to the interface spin configuration in this biased layer and our observations of the magnetic structure in the TbFe "pinning" layer have clear implications for the nature of the frozen AFM spin state in typical AFM/FM exchange-biased systems.

REFERENCES

[1] J. Nogues, I. K. Schuller. J. of Magn. Magn. Mater. **192**, 203 (1999).

[2] J. Nogues, C. Leighton and Ivan K. Schuller, Phys. Rev. B **61**, 1315 (2000).

[3] S. Mangin, F. Montaigne and Y. Henry, Phys. Rev. B **68**, 140404 (2003).

[4] K.V. O'Donovan, J.A. Borchers, C.F. Majkrzak, O. Hellwig and E.E. Fullerton, Phys. Rev. Lett. **88**, 067201 (2002), and references therein.

[5] Y. Henry, S. Mangin, T. Hauet and F. Montaigne, to be published (2004).

Neutron Scattering Study of Spin Excitations in the Singlet Ground State of $SrCu_2(BO_3)_2$

B. D. Gaulin, S. Haravifard, J. P. Castellan, A. J. Berlinsky and H. A. Dabkowska
McMaster University
Hamilton, ON, L8S 4C6, Canada

S.-H. Lee, Y. Qiu, and J. R. D. Copley
NIST Center for Neutron Research
National Institute of Standards and Technology
Gaithersburg, MD, 20899-8562

The low temperature behavior of quantum magnets can be very different from that of their classical counterparts. While classical magnets usually enter an ordered state at low temperatures with a particular pattern to their magnetic structure, quantum magnets can tie up all their magnetic moments into quantum mechanical entities (singlets) and enter a non-magnetic state at low temperatures. We have used the very high energy resolution afforded by the Disk Chopper Spectrometer (DCS) at the NCNR to study the triplet excitations of one such quantum antiferromagnet, $SrCu_2(BO_3)_2$ by which we gain a microscopic understanding of how the quantium spins interact, and how this unusual non-magnetic state dissolves away as the temperature is raised.

Layered quantum magnets have been at the forefront of condensed matter physics research in large part due to their relevance to high temperature superconductivity. Two-dimensional copper-oxides, in which conducting holes are introduced, provide the framework for much exotic behavior, with high temperature superconductivity being the best appreciated example. More broadly, quantum antiferromagnets are of interest because the paradigm for their behavior is not the orderly, antiparallel arrangement of magnetic moments in a Neel state, but the formation of singlets in which the magnetic moments lose their spin-up or spin-down identity and reside in a quantum mechanical superposition of both spin-up and spin-down.

$SrCu_2(BO_3)_2$ is such a quasi-two dimensional quantum antiferromagnet. Quantum spin $^1/_2$ magnetic moments reside on the Cu^{2+} sites in the tetragonal structure shown in Fig. 1. There the tetragonal basal plane is shown and it can be seen that the Cu sites are arranged in orthogonal dimers, pairs of Cu^{2+} sites, which decorate the two-dimensional square lattice. The leading terms which describe how the spin $^1/_2$ magnetic moments interact are given by an intra-dimer antiferromagnetic exchange interaction, J, as well as an inter-dimer exchange interaction, J', which is also known to be antiferromagnetic. This is also illustrated in Fig. 1 below.

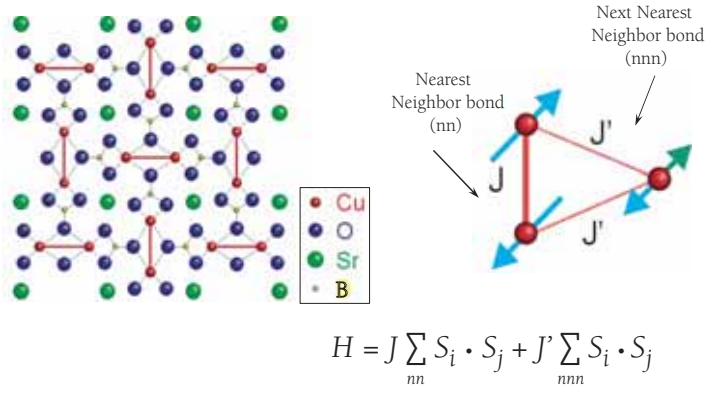

FIGURE 1: A schematic drawing of the basal plane structure of $SrCu_2(BO_3)_2$ is shown (left) which highlights the Cu^{2+} dimers (red atoms joined by a red bar). The leading order exchange interactions are illustrated in the top right diagram which shows the nearest-neighbor (nn) intra-dimer (J) and next-nearest-neighbor (nnn) inter-dimer (J') antiferromagnetic interactions. The leading order Hamiltonian for this system is given in the lower right of the figure.

A remarkable feature of this model for interacting spin $^1/_2$ dimers is that it was considered theoretically and solved exactly in 1981 by Shastry and Sutherland [1]. It is known, for example, that if J is adequately strong relative to J', the low temperature state of such a system will be a non-magnetic collective singlet, in which all the spin $^1/_2$ magnetic moments are tied up in singlets within the dimers. In contrast, if J'/J is greater than approximately 0.69, then a somewhat complicated, four sublattice, Neel state is formed at low temperatures. Early characterization [2] established $SrCu_2(BO3)_2$ on the singlet ground state side of this boundary and neutron scattering measurements [3] by Kageyama and co-workers directly observed singlet-triplet spin excitations as well as multi-triplet bound states.

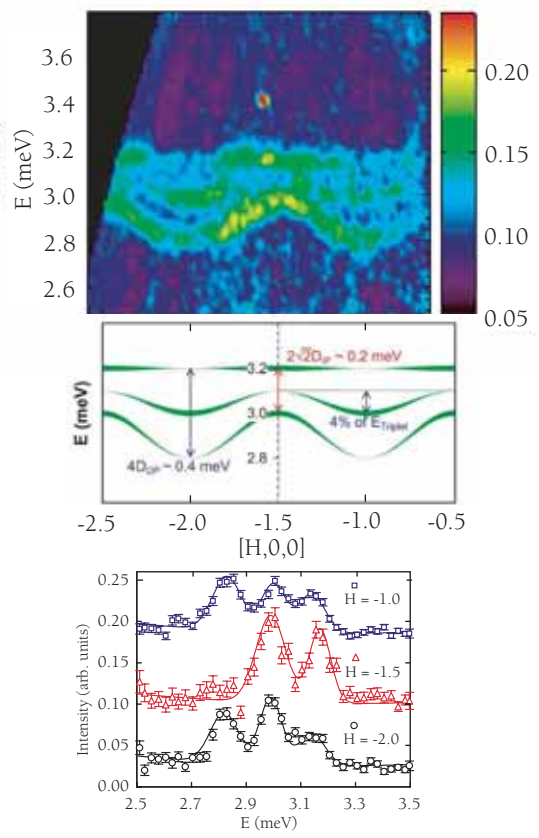

FIGURE 2: High-resolution inelastic neutron scattering data from DCS is shown in the top and bottom panels. The bottom panels are cuts through the scattering map displayed in the top panel which approximate constant-*Q* scans of the [*H*,0,0] form. The middle panel shows how subleading, Dzyaloshinskii-Moriya (DM) interactions manifest themselves in such a high-resolution experiment. Out-of-plane interactions are responsible for the full bandwidth of the scattering, while in-plane DM interactions give rise to the small energy gap at [1.5, 0, 0].

Inelastic neutron scattering measurements were carried out on a large single crystal of $SrCu_2(^{11}BO_3)_2$ using both the spin-polarized triple-axis spectrometer (SPINS) at the NCNR and DCS. Measurements on SPINS established the two dimensional nature of the magnetic scattering. The DCS measurements were performed with 5 Å incident neutrons, giving an elastic energy resolution of ≈ 0.09 meV, and this allowed us to examine fine detail in the dispersion of the triplet excitations. We carried out these measurements in the (*H*,0, *L*) reciprocal lattice plane. The DCS measurements could then integrate up the inelastic scattering in *L*, so as to continuously map out the triplet dispersion along [*H*, 0] within the basal plane. The resulting map at low temperatures is shown in the top panel of Fig. 2. It can be seen that the three triplet excitations are clearly resolved. Their dispersion can be understood in terms of sub-leading contributions to the interactions between the quantum *s* = 1/2 magnetic moments (i.e., considerations other than *J* and *J*') which must be allowed by the symmetry of the crystal structure.

We also measured the temperature dependence of the triplet excitations at about 3 meV with both DCS (shown at low temperatures in Fig. 2) and SPINS. The two triplet excitations were also measured with SPINS at higher energy. This relative temperature dependence is shown in Fig. 3. Clearly the one and two triplet excitations possess the same unusual temperature dependence. Interestingly, this dependence is identical to that of the bulk susceptibility, and the solid line in Fig. 3 is the complement of the bulk susceptibility, 1-χ, as measured with a SQUID magnetometer. It is not completely clear why this quantity should be such a good descriptor of the unusual manner in which the triplet excitations fade away into the paramagnetic state, but we can speculate that it may reflect the localized nature of the quantum mechanical wavefunctions of the triplet excitations themselves.

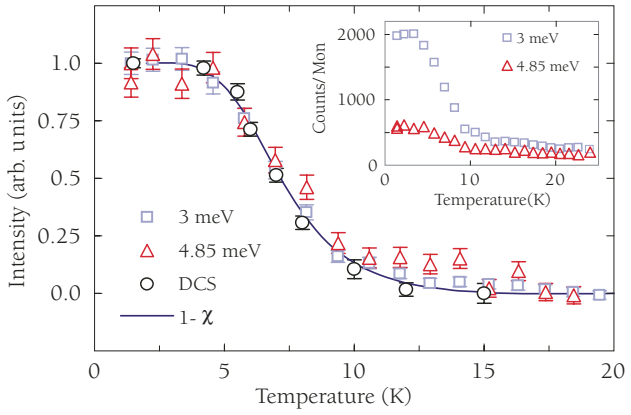

FIGURE 3: The normalized temperature dependences of the triplet excitations near 3 meV measured on SPINS (blue) and DCS (black) the two-triplet bound state near 4.85 meV measured on SPINS (red). The inset displays the unnormalized SPINS data. This unusual temperature dependence is almost perfectly tracked by the complement of the dc-susceptibility, 1-χ, perhaps reflecting the localized nature of the excitations.

REFERENCES:

[1] S. Shastry and B. Sutherland, Physica (Amsterdam) **108B**, 1069 (1981).

[2] S. Miyahara and K. Ueda, Phys. Rev. Lett., **82**, 3701 (1999).

[3] H. Kageyama et al, Phys. Rev. Lett., **84**, 5876 (2000); O. Cepas *et al.*, Phys. Rev. Lett., **87**, 167205 (2001).

Persistence and Memory of Polar Nanoregions in a Ferroelectric Relaxor in an Electric Field

G. Y. Xu and G. Shirane
Brookhaven National Laboratory
Upton, NY 11973-5000

P. M. Gehring
National Institute of Standards and Technology
NIST Center for Neutron Research
Gaithersburg, MD 20899-8562

Lead-oxide relaxor ferroelectric compounds exhibit the highest known piezoelectric coefficients and strains and are thus exceptionally attractive for device applications. Nanoscale regions of randomly oriented polarization, i.e., polar nanoregions or "PNR," form within these compounds well above T_c, and give rise to strong diffuse scattering. Cooling these relaxors in an external field from above T_c is believed to produce a microscopically uniform polar phase via rotation of the PNR, much like the case when field-cooling a ferromagnet. Surprisingly, the diffuse scattering in $Pb(Zn_{1/3}Nb_{2/3})O_3$ doped with x = 8 % substance fraction of $PbTiO_3$, for which the piezoelectric properties are greatest, persists upon field cooling, and is even partially enhanced. Further, the memory of the field reappears after heating the system above T_c, and then cooling in zero field.

The relaxor ferroelectric compounds $PbMn_{1/3}Nb_{2/3}O_3$ (PMN), $PbZn_{1/3}Nb_{2/3}O_3$ (PZN), and their solid solutions with $PbTiO_3$ (PT) have received enormous attention in the materials science and condensed matter physics communities due to their record-setting dielectric and piezoelectric properties [1]. They have supplanted lead zirconate (PZT) ceramics as the basis of state-of-the-art piezoelectric sensors and actuators, which are used to convert between mechanical and electrical forms of energy, and they show promise as nonvolatile memories. A distinguishing property of relaxors, as compared to classic ferroelectrics, is the appearance of nanometer-sized regions of local, randomly oriented, polarization at the so-called "Burns temperature" T_d [2], which is several hundred degrees above the ferroelectric transition temperature T_c. These polar nanoregions (PNR) are believed to play a key role in the unusual relaxor behavior [3]. Several models based on random fields in a dipole glass [4] have been proposed to explain the properties of the PNR. As the PNR represent small regions of polar order, they give rise to a strongly temperature dependent diffuse scattering that grows monotonically with decreasing temperature as seen with both x-ray and neutron scattering methods, and that grows monotonically with decreasing temperature. In addition, the PNR have been imaged directly with high-resolution piezoresponse force microscopy techniques.

Many unsolved questions concerning the PNR remain. Do they facilitate the ferroelectric phase transition, or do they impede it? What prevents the PNR from merging into the surrounding, macroscopically polar, environment below the ferroelectric phase transition temperature T_c? In studies of ferroelectrics, an external field is often applied to observe how the system responds. Yet few studies to date have examined the PNR response in relaxors to an electric field. A previous study showed that the diffuse scattering in a PZN based compound responds anisotropically when field cooled (FC) in an electric field [5]. The diffuse scattering measured transverse to the (300) Bragg peak is unaffected by an electric field applied along the [001] direction, whereas that transverse to the orthogonal (003) Bragg peak is significantly suppressed. Such an anisotropic response suggests that those PNR having "properly oriented" polarizations can be forced to "melt" into the surrounding macroscopically polar environment with the assistance of an external field, thereby producing a more "microscopically-uniform" polar state.

One of the most studied relaxor systems is PZN, which has a cubic perovskite structure. When doped with $PbTiO_3$, single crystals of PZN-xPT are obtained that can exhibit even higher piezoelectric responses. The single crystal examined in our study had the optimal piezoelectric responses of x = 8 %. Because PZN-8%PT has a rhombohedral ground state with <111> type polarizations at low temperatures, we chose to investigate the effect of an electric field applied along the [111] direction. The neutron diffuse scattering was measured in the (*HKK*) scattering plane near the (300) Bragg peak at 300 K < T_c (= 450 K) and these data are shown in Fig. 1.

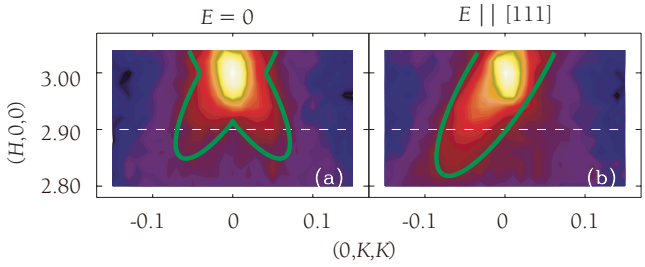

FIGURE 1: Contour plots (log-scale) of the neutron diffuse scattering intensity measured at 300 K (< T_c) in the (*HKK*) reciprocal scattering plane close to the (300) Bragg peak. The panels show data taken after the sample was (a) zero-field cooled (ZFC) and (b) field-cooled (FC) below T_c for electric field $E \parallel [111]$. The solid green lines are guides to the eye to emphasize the (a) symmetric and (b) asymmetric shapes of the diffuse scattering.

When the crystal is zero-field cooled (ZFC), the diffuse scattering geometry is symmetric about the [100] axis, and forms the butterfly-shape with "wings" of equal intensity on each side shown in Fig. 1(a). This is consistent with the three-dimensional diffuse scattering distribution consisting of <110> rod-type structures, where PNR with different polarizations contribute to different <110> diffuse rods. Because of the non-zero out-of-plane resolution in our measurements, when moving away from the center of the Bragg peak in the (*HKK*) plane, tails from the <110> rods are then picked up. This results in the butterfly-shaped pattern, which is symmetric about (300), as required by the crystal symmetry. The application of a moderate electric field of E = 200 kV/m along the [111] direction while still at 300 K did not change the diffuse scattering, which suggests that the PNR are robust in the ferroelectric phase. The sample was then heated to T = 500 K, and the 200 kV/m electric field along [111] was applied again. This time, as shown in Fig. 1(b), the diffuse scattering pattern becomes asymmetric with respect to the [100] direction. The left "wing" is clearly enhanced, while the right one is suppressed.

A more detailed look at the temperature dependence of the diffuse scattering is shown in Fig. 2, where linear scans measured along (2.9,*K*,*K*) (corresponding to the dashed line in Fig. 1) are plotted. In the ZFC state, the symmetric double-peaked profiles indicate that intensities from both wings increase evenly with cooling. In the FC state, the intensity of the left wing starts to increase below T_c, while the right wing remains almost the same. At 300 K, the left wing intensity is clearly much higher than that it is in the ZFC state. Upon removal of the electric field at 300 K, the asymmetric diffuse pattern persists, indicating that the PNR are frozen into the FC configuration. This behavior is quite similar to that of a spin glass system where cooling through T_c with and without an applied magnetic field leads to different final states, and the difference is only observable below T_c.

In addition to the unexpected persistence of the diffuse scattering in the presence of an external field, and thus of the PNR, a remarkable memory effect was observed whereby cooling the crystal to 500 K, i.e., 50 K above T_c, and then cooling in zero field did not result in an evenly balanced intensity between the wings of the diffuse scattering about (300). Instead, the left wing remained higher just as it had been in the FC state. Only by heating above 525 K did the system finally return to the initial ZFC state.

The response of polar nanoregions (PNR) in the relaxor compound PZN-8%PT subject to a [111]-oriented electric field has been studied by measuring the diffuse scattering. Contrary to classical expectations, the diffuse scattering associated with the PNR persists and is even partially enhanced by field cooling. The effect of the external electric field is actually retained by the PNR after the field is removed. The memory of the applied field reappears even after heating the system above T_c, and cooling in zero field.

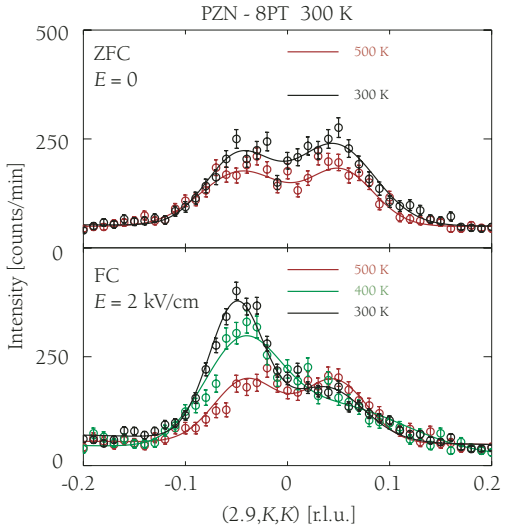

FIGURE 2: Linear cuts through the diffuse scattering shown in Fig. 1 performed at (2.9,*K*,*K*), after the sample was ZFC (top panel), and FC (bottom panel), measured at temperatures of 300 K, 400 K, and 500 K. The solid lines are fits to a sum of two Gaussian peaks.

REFERENCES:

[1] S.-E. Park and T. R. Shrout, J. Appl. Phys. **82**, 1804 (1997).

[2] G. Burns and F. H. Dacol, Phys. Rev. B **28**, 2527 (1983).

[3] L. E. Cross, Ferroelectrics **76**, 241 (1987).

[4] R. Pirc and R. Blinc, Phys. Rev. B **60**, 13470 (1999); R. Fisch, Phys. Rev. B 67, 094110 (2003).

[5] P. M. Gehring, K. Ohwada, and G. Shirane, Phys. Rev. B **70**, 014110 (2004).

[6] Guangyong Xu, P. M. Gehring, and G. Shirane, submitted to Phys. Rev. Lett.

Spin-Chirality on a Two-Dimensional Frustrated Lattice

K. Matan, J-H. Cho and Y. S. Lee
Massachusetts Institute of Technology
Cambridge, MA 02139

D. Grohol and D. G. Nocera
Massachusetts Institute of Technology
Cambridge, MA 02139

S-H. Lee and J. W. Lynn
NIST Center for Neutron Research,
National Institute of Standards and Technology
Gaithersburg, MD 20899-8562

Spins located in the plane of an equalateral triangle are geometrically frustrated if they are coupled antiferromagnetically. As a compromise, they can order by rotating 120° with respect to each other as you go clockwise around the triangle. They can rotate to the right or to the left, and these arrangements have different handedness (chirality). In a conducting material having such a textured system of spins, electron transport is affected, possibly displaying an anomalous Hall effect. By manipulating the spin texture one may be able to control the transport properties to possibly make spintronic devices.

Using new chemical synthesis methods, we have produced large single crystal samples of iron jarosite, $KFe_3(OH)_6(SO_4)_2$, an ideal Kagomé lattice antiferromagnet. The Kagomé lattice antiferromagnet, formed of corner sharing triangles, is one of the most highly frustrated two-dimensional (2D) lattices. This material possesses robust chiral correlations related to the arrangement of spins around triangular plaquettes. Combined thermodynamic and neutron scattering measurements reveal that the phase transition to the ordered ground-state is unusual [1]. At low temperatures, application of a magnetic field induces a transition between states with non-trivially different spin-textures.

The magnetic Fe^{3+} ions of jarosite have spin-5/2 and lie at the corners of the triangles of the Kagomé lattice, shown in Fig. 1. Since the interaction is antiferromagnetic, the spin system is frustrated, and the corner-sharing arrangement leads to a higher degree of degeneracy for the ground state compared to the triangular lattice. Even though the Kagomé lattice antiferromagnet should not order at any non-zero temperature, the compound $KFe_3(OH)_6(SO_4)_2$ orders magnetically in the "q = 0" arrangement (shown in Fig. 1a) below $T_N \approx 65$ K due to small anisotropy terms in the spin Hamiltonian, where q is the modulation wavevector. The ordered spins can be decomposed into three sublattices, with the spins on each triangle labeled as $\vec{S}_1$, $\vec{S}_2$, and $\vec{S}_3$. The *vector chirality* for each triangle may be defined as $\vec{K}_v = \frac{2}{3\sqrt{3}}(\vec{S}_1 \times \vec{S}_2 + \vec{S}_2 \times \vec{S}_3 + \vec{S}_3 \times \vec{S}_1)$. For the coplanar arrangement, this vector is parallel to the c-axis with amplitude +1 or -1. In the ordered state, each triangle has positive chirality (+1), such that the spins point directly toward or away from the center of each triangle. An ordered phase on a Kagomé lattice is characterized by two order parameters (the sublattice magnetization and the vector chirality) that have different symmetries. An intriguing possibility is that these symmetries are broken at different temperatures in our sample.

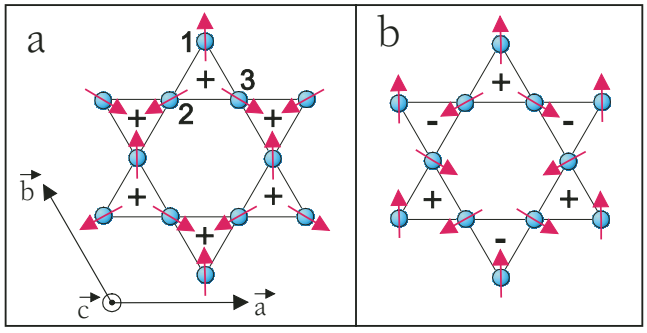

FIGURE 1: The Kagomé lattice with spins arranged in two different configurations. a) The "q = 0" structure, which is the ground state configuration for iron jarosite. The spin arrangement has uniform, positive vector chirality, indicated by the + within each triangular plaquette. b) An alternate spin arrangement with staggered vector chirality, known as the $\sqrt{3} \times \sqrt{3}$ structure.

The first hints of the interactions that drive the magnetic transition come from magnetization measurements. With the field oriented perpendicular to the Kagomé plane, a sharp peak appears near 65 K, indicative of the transition to the 3D magnetically ordered state and the presence of weak ferromagnetism along the *c*-direction. Recent theoretical work shows that antisymmetric exchange, via the Dzyaloshinskii-Moriya (DM) interaction, may induce such a moment by canting the spins slightly out of the plane. This interaction causes the spins on each triangle in the sample to form

an "umbrella" structure and gives each Kagomé plane a net ferromagnetic (FM) moment. However, the interlayer coupling in iron jarosite causes the FM moments to couple antiferromagnetically between layers in the absence of an applied field, as shown in the inset of Fig. 2b. To investigate this spin canting, magnetization measurements were performed as a function of magnetic field along the *c*-direction as shown in Fig. 2a. The results show an abrupt change in the magnetization at a critical field, H_C, which we define as the field at which d*M*/d*H* is a maximum. This abrupt increase is most likely caused by a 180° rotation of all spins on the previously oppositely canted layers, as shown in the inset of Fig. 2b. The critical field as a function of temperature is also shown in Fig. 2b. The field-induced spin-canting transition corresponds to a non-trivial change in the spin-texture of the jarosite sample. In particular, the transition yields a net, non-zero value for the *scalar chirality*, defined on each triangular plaquette as $K_s = \vec{S}_1 \cdot \vec{S}_2 \times \vec{S}_3$. The presence of this type of chirality (in static or fluctuating forms) can have important consequences in strongly correlated electron systems, such as yielding an anomalous Hall effect in metallic materials. In iron jarosite, we have discovered a phase transition in which a net scalar chirality can be "switched on" by a magnetic field.

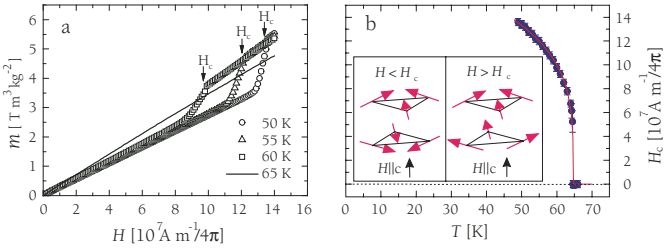

FIGURE 2: Measurements of the field-induced transition to a state with non-zero scalar chirality. a) Magnetic moment, *m*, versus applied field for several temperatures with $H \parallel c$. (Note that $M \propto m$.) The H_C values indicate the fields where d*M*/d*H* has a maximum. b) H_C versus temperature. The inset depicts the change in the spin configuration below and above H_C. The solid line in b) correspond to power-law forms for H_C and *M* with the exponent $\beta = 0.25$ and $T_N = 64.7$ K.

In order to probe the microscopic behavior of the magnetism in the temperature regime above T_N, we performed inelastic neutron scattering measurements of the spin fluctuations at $T = 70$ K within the $L = 0$ plane of reciprocal space. For the 3D ordered spin structure below T_N, the stacking arrangement of the planes doubles the magnetic unit cell with respect to the structural unit cell such that the magnetic Bragg peaks occur at half-odd-integer values of *L* ($L \neq 0$). However, for temperatures above T_N, the correlations between layers are destroyed and the 2D spin fluctuations yield "rods" of scattering in reciprocal space along the *L* direction. The scans in Fig. 3a pass through the 2D rods of scattering and directly measure the dynamic structure factor of the spin correlations of the single Kagomé planes in iron jarosite.

A reciprocal space map of the intensity of the spin fluctuations is shown in Fig. 3a. First, the fact that the intensities are centered within the structural Brillouin zones indicates that the fluctuations have the $q = 0$ arrangement. The absence of scattering at the (2,0,0) position is

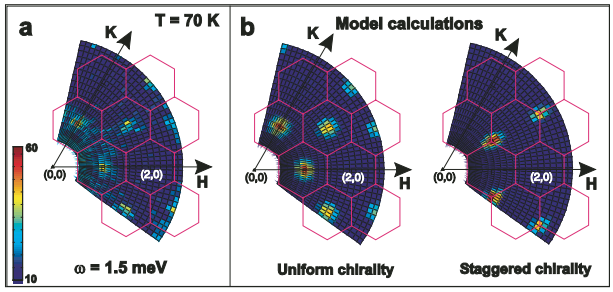

FIGURE 3: Inelastic neutron scattering data for $KFe_3(OH)_6(SO_4)_2$ measured above T_N, along with structure factor calculations. a) Intensity contour plot of data from inelastic neutron scattering measurements of a single crystal sample (mass = 48 mg). The bright regions are the loci of scattering intensity for the low energy ($\hbar\omega = 1.5$ meV) spin fluctuations at $T = 70$ K, above T_N. b) Model calculations of the intensity as described in the text. The left plot corresponds to short-ranged $q = 0$ correlations with uniform vector chirality, whereas the plot on the right depicts $\sqrt{3} \times \sqrt{3}$ correlations. Both calculations are for the case in which there is no preferred spin direction within the Kagomé plane.

consistent with this spin arrangement. Secondly, the nearly equivalent intensities at the (1,0,0) and (1,1,0) positions reveal that the spin fluctuations have *XY* symmetry at this temperature (the spin-rotational symmetry within the Kagomé plane is not broken). In contrast, at low temperatures in the 3D ordered state, a preferred spin direction is chosen and the intensities at (1,0,*L*) and (1,1,*L*) differ considerably. The observation of short-range $q = 0$ correlations in the 2D fluctuations implies a particular arrangement of the vector chirality. In each region of correlated spins, the vector chirality must be uniform (all positive or all negative for each plaquette). We calculated the neutron scattering intensity arising from $q = 0$ correlations between coplanar spins assuming only positive chirality. Our model calculations are based on 7-unit cell clusters of spins, and we have averaged over all spin directions within the Kagomé plane. The results are shown in Fig. 3b, and the agreement with the data is excellent. The presence of vector chiral order above T_N may be naturally explained in light of the DM interaction.

Our measurements of this ideal Kagomé material reveal novel magnetic behavior related to two types of spin chirality: vector and scalar. The DM interaction is a significant perturbation to the Heisenberg Hamiltonian and strongly influences the low temperature physics. For $T > T_N$, the vector spin chirality is ordered even in the absence of broken spin-rotational symmetry. In the ordered state below T_N, we have discovered a field-induced transition to a state with non-zero scalar chirality. Thus, materials based on jarosites may be promising candidates for studies of the coupling between non-trivial spin textures and the transport of electrons in frustrated systems. For example, carrier-doped compounds would likely exhibit an anomalous Hall effect of topological origin, and this may possibly have useful applications in spin-based electronics.

REFERENCES:

[1] D. Grohol, K. Matan, J.H. Cho, S.-H. Lee, J.W. Lynn, D.G. Nocera, Y.S. Lee, Nature Materials **4** (4), 323 (2005).

Inter-Granular Giant Magnetoresistance in a Spontaneously Phase Separated Perovskite

J. Wu and C. Leighton
University of Minnesota
Minneapolis, MN 55455

J. W. Lynn and C.J. Glinka
NIST Center for Neutron Research,
National Institute of Standards and Technology
Gaithersburg, MD 20899-8562

J. Burley, H. Zheng, and J. F. Mitchell
Argonne National Laboratory
Argonne, IL 60439

Giant magnetoresistance (GMR) has greatly advanced our understanding of exchange coupling and spin-dependent scattering and has revolutionized magnetic recording. In the conventional view, GMR requires the fabrication of artificial magnetic heterostructures, i.e., chemical interfaces are required. Using small-angle neutron scattering (SANS), we show here that a certain perovskite oxide ($La_{1-x}Sr_xCoO_3$) can phase separate into ferromagnetic metallic clusters in a non-ferromagnetic matrix, and that this leads to a GMR effect. We argue that this system is a naturally forming analog to the artificial structures fabricated by depositing nanoscale magnetic particles in a metallic or insulating matrix, i.e., this material displays a GMR effect *without* the introduction of chemical interfaces.

The colossal magnetoresistance (CMR) in bulk perovskite oxides, and the GMR in artificial metallic heterostructures seemingly originate from very different physics. Recent progress in magnetic phase separation however, has shown that heterogeneity also plays a key role in understanding CMR, as these randomly doped oxides can exhibit spatial coexistence of ferromagnetic (F) metallic and non-F insulating regions. Doped cobaltites such as $La_{1-x}Sr_xCoO_3$ (LSCO) have been shown to exhibit this phase inhomogeneity where at low x the non-F regions dominate and the system behaves as a semiconducting spin-glass, whereas at high x ($x > 0.18$) a metallic F is found. In this work SANS was employed as a probe of this magnetic inhomogeneity. The wavevector transfer (q) dependence of the SANS from LSCO is shown in Fig. 1 for $x = 0.3$ (i.e., in the F metallic phase) where the Curie temperature, $T_C = 220$ K. Strong magnetic scattering is observed, following the Porod form, $I(q) \propto q^{-4}$, due to scattering from a 3-D distribution of "hard spheres" of radius R in the regime $q >> R^{-1}$. This is often observed in Fs due to scattering from domains and observation of this form down to $q = 0.01$ Å^{-1} implies that this $x = 0.3$ sample exhibits long-range F order. For $T > T_C$, $I(q)$ consists of weak scattering from the chemical microstructure, while near T_C significant intensity is observed at high q. This follows the Lorentzian form, $I(q) = I_0 / (q^2 + \kappa^2)$, with I_0 and κ constants, due to the quasielastic critical scattering near T_C.

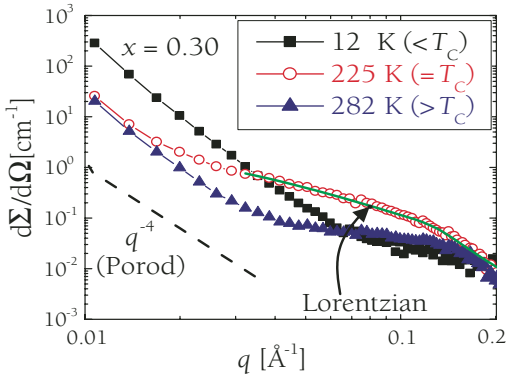

FIGURE 1: q dependence of the absolute SANS intensity for $x = 0.30$. Note that $I(q) \propto d\Sigma/d\Omega$

Examining Fig. 1 it is clear that the scattering can be separated into a low q part (from long-range F order) and a higher q Lorentzian part (from short-range fluctuations). We therefore present the T dependence by plotting the low q intensity (Fig. 2, top panel) and the high q intensity (middle panel), along with the T dependence of the magnetization, M, (bottom panel). Starting at $x = 0.30$, which has long-range F order, we find a sharp increase in the low q intensity at T_C, in agreement with $M(T)$. The high q data show a narrow peak near T_C, due to the expected critical scattering. At $x = 0.18$, the critical composition for long-range order, the low q scattering is less intense and has a broad onset near T_C, whereas the high q scattering exhibits a wide peak, reflecting the fact that long-range F order is barely stable. At $x = 0.15$ the low q intensity is weak, with no transition to long-range F order. In this case the high q intensity shows a T dependence that closely mimics $M(T)$, in contrast to $x = 0.18$ and $x = 0.30$. Given that this high q intensity is due to scattering from short length-scale F correlations it is clear that the sizeable magnetization at $x = 0.15$ results from F clusters.

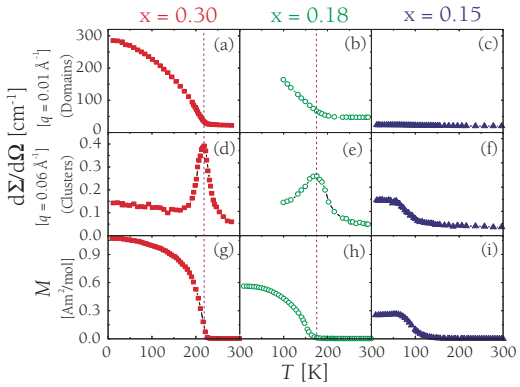

FIGURE 2: T dependence of, the SANS intensity at low q (top panel), high q (middle panel), and the magnetization (bottom panel), for x = 0.30, 0.18 and 0.15.

The Lorentzian form allows for the extraction of the magnetic correlation length, ξ, as shown in Fig. 3. At x = 0.30 the spin correlations form above T_C and ξ diverges at T_C due to the onset of long-range order. For x = 0.18, however, the correlation length, does not diverge, although it increases near T_C. For the case of x = 0.15 no critical divergence exists due to the absence of a transition to long-range order. Instead, ξ increases below 150 K (Fig 3(c)), due to nucleation of isolated F clusters, with $\xi \approx 20$ Å at low T.

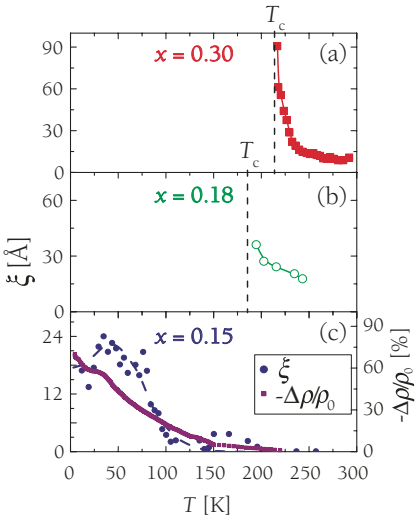

FIGURE 3: T dependence of the correlation length for x = 0.30 (a), 0.18 (b) and 0.15 (c). The bottom panel also shows the T dependence of the magnetoresistance at $H = 90/4\pi$ MAm^{-1} (90 kOe).

The picture that emerges at x = 0.15 is of isolated F clusters embedded in a non-F matrix. In order to correlate the information provided by SANS with the electronic properties, we examined magnetotransport in single-crystals. The 10 K magnetoresistance (MR) for x = 0.15 is shown in Fig. 4. The observed large negative, which persists to high field, is hysteretic (with peaks in ρ at the coercive field, $H_C = 6.5/4\pi$ MAm^{-1}), and exhibits distinct differences between the virgin curve and subsequent cycles. This effect only occurs at low T, as shown in Fig. 3(c), which plots the T dependence of the MR at $H = 90/4\pi$ MAm^{-1}. The MR turns on at the same temperature as the first indications of cluster nucleation, meaning that the MR observed here only occurs when F clusters form in the semiconducting non-F matrix.

This point is reinforced by the composition dependence in the inset to Fig. 4, which shows a rapid decrease at x = 0.18, where the isolated F clusters coalesce into a percolated network.

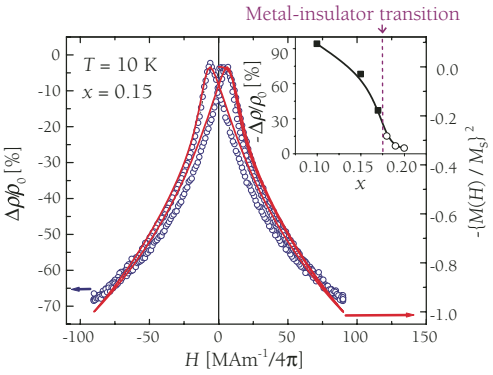

FIGURE 4: Magnetoresistance of an x = 0.15 single crystal of LSCO at 10 K. The right axis shows $(M(H)/M_S)^2$ where M_S is the saturation value of M at $H = 90/4\pi$ MAm-1, and the inset shows the doping dependence of the MR at this same field value.

These MR phenomena exhibit remarkable similarity to the inter-granular MR previously observed in artificial structures composed of nanoscale F particles in an insulating or metallic matrix (e.g. Co-SiO_2, Fe-Cu). These composites display sizeable negative MR, noticeable differences between the virgin curve and subsequent cycles, strong hysteresis (with peaks in ρ at H_C), as well as an MR that decreases rapidly beyond the percolation limit. Quite simply, we suggest that LSCO is a naturally occurring analog of these artificial granular systems. In our case the system spontaneously phase separates into metallic F clusters embedded in a semiconducting matrix of hole-poor non-F material. The hysteretic low-T MR arises due to spin-dependent transport between F clusters. ρ is maximized at $\pm H_C$ (where M = 0 and the cluster magnetization vectors are randomly aligned) and is reduced in applied fields due to alignment of the cluster magnetizations.

These qualitative statements can be strengthened by quantitative analyses. Specifically, in the artificial matrix systems MR $\propto (M(H)/M_S)^2$, where M_S is the saturation magnetization. The agreement with this scaling form is shown in Fig. 4, where the solid line depicts the measured $(M/M_S)^2$. It has also been shown that in the insulating matrix systems, $\rho = \rho_0 \exp(T_0 / T)^{1/2}$, with ρ_0 and T_0 constants, due to hopping between clusters in the presence of a Coulomb energy penalty. Such a T dependence is indeed observed (data not shown).

In summary, we have shown that the spontaneously phase separated perovskite oxide $La_{1-x}Sr_xCoO_3$ is the first known natural analog to artificial GMR structures composed of ferromagnetic particles embedded in non-ferromagnetic insulating or metallic matrices. We observe an intergranular GMR effect even without the deliberate introduction of chemical interfaces. Our work demonstrates the feasibility of fabricating chemically homogeneous solids where magnetic phase separation leads to the formation of magnetoelectronic heterostructures with useful function.

REFERENCES

See J. Wu et al., Phys. Rev. Lett. **94** 037201 (2005) and references therein.

Magnetism and Ferroelectricity in $HoMnO_3$ and $TbMnO_3$

O. P. Vajk and J. W. Lynn
NIST Center for Neutron Research
National Instituteof Standards and Technology
Gaithersburg, MD 20899-8562

M. Kenzelmann
Laboratory for Solid State Physics
ETH Honggerberg
CH-8093 Zurich, Switzerland

S. B. Kim, C. L. Zhang and S.-W. Cheong
Rutgers University
Piscataway, NJ 08854

A. B. Harris
University of Pennsylvania
Philadelphia, PA 19104

S. Jonas and C. Broholm
Johns Hopkins University
Baltimore, MD 21218

J. Schefer
Laboratory for Neutron Scattering
ETH Zurich and Paul Scherrer Institute
CH-5232 Villigen, Switzerland

Ferroelectricity is the spontaneous electric polarization of a material, and is an electric analogue to magnetic ordering such as ferromagnetism. Although there are many ferroelectric and magnetic materials, very few have simultaneous magnetic and ferroelectric order. Among this rare class of solids, known as mutiferroics, only a select few exhibit significant coupling between the magnetic and ferroelectric properties. The origin of this unusual coupling is not yet well understood, and these exotic materials have attracted added attention recently because of the intriguing possibility of using these coupled order parameters in novel spintronic device applications. We have performed magnetic neutron scattering studies at the NCNR's BT-2 triple-axis spectrometer of two multiferroics that exhibit significant magnetic-ferroelectric coupling, hexagonal $HoMnO_3$ [1] and perovskite $TbMnO_3$ [2]. Our results are crucial first steps towards a fuller understanding of the interaction between magnetism and ferroelectricity in multiferroics.

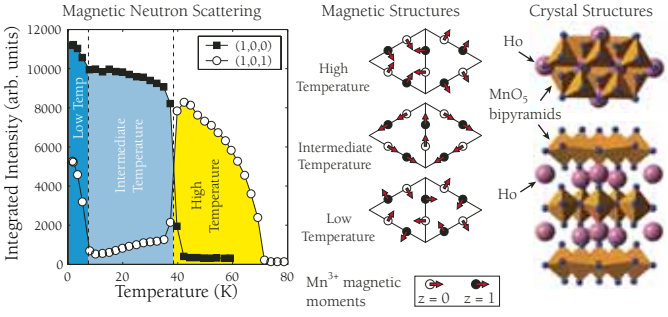

FIGURE 1: Neutron scattering measurements (left) are used to determine the magnetic structure of $HoMnO_3$ (middle) and the transitions between these structures. Top and side views of the crystal structure are shown on the right. The middle panel shows projections of the moments of the bottom layer, $z = 0$, and middle layer, $z = 1$, Mn^{3+} ions are located at the center of the orange bipyramids.

In hexagonal $HoMnO_3$, magnetic Mn^{3+} ions (surrounded by O^{2-} ions) form two-dimensional (2D) triangular lattices of spin-2 moments in the *a-b* plane, which are then stacked in an alternating fashion along the *c* axis (see Fig. 1). Below around 875 K, these sheets buckle, displacing the Ho^{3+} ions between these sheets in the c direction and giving rise to the ferroelectric order. Neighboring Mn^{3+} spins within the 2D sheets are antiferromagnetically coupled, and below 72 K the magnetically frustrated system orders in a structure where adjacent spins are at a 120 degree angle. At around 40 K, $HoMnO_3$ undergoes a spin reorientation transition with a sharp dielectric anomaly, indicating a strong coupling between the ferroelectric and antiferromagnetic order in this system.

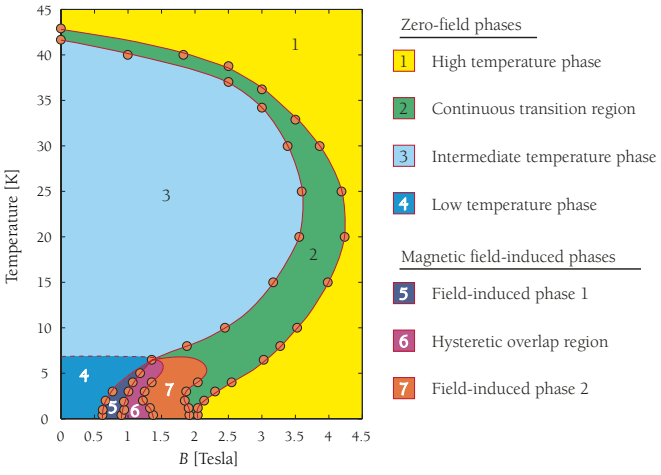

FIGURE 2: Phase diagram of $HoMnO_3$ as a function of temperature and magnetic field.

We have established the magnetic phase diagram as a function of both temperature and magnetic field using single-crystal samples of $HoMnO_3$. The magnetic ordering temperature of $HoMnO_3$ is not affected by fields up to 7 Tesla, but a magnetic field does strongly affect the spin reorientation transitions that occur within the ordered phase, as shown in Fig. 2. At very low temperatures, the magnetic phase diagram becomes much

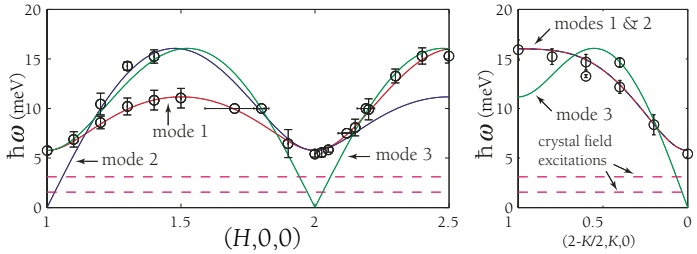

FIGURE 3: Spin wave dispersion in $HoMnO_3$. Circles are experimental data. Solid lines are fits to a theoretical model. Dashed lines show dispersionless crystal field levels.

more complex, and two distinct intermediate phases emerge with significant hysteresis in the transition between them.

To elucidate the energetics of this material, we have also performed neutron scattering measurements of the spin-wave spectrum of $HoMnO_3$. Spin waves have different frequencies depending on their wavelength, and by measuring the dispersion we can determine the strength of the microscopic interaction between each spin on the lattice and its neighbors. Our results for the in-plane dispersion are shown in Fig. 3. The dispersion is independent of the out-of-plane direction, indicating that the dynamics are almost completely two-dimensional.

We fit our results to a simple model with only two parameters: a nearest-neighbor antiferromagnetic exchange J plus an additional anisotropy D which makes spins prefer to lie in the a-b plane. The solid lines in Fig. 3 show our fit results, with J = 2.44 meV and D = 0.38 meV. Weaker interactions must be present in the system as well in order to explain the complex magnetic behavior, but the quantitative results we extract for J and D are a critical first step towards being able to model the complex interactions between the magnetism and the ferroelectricity in $HoMnO_3$. The complexity of the phase diagram revealed by neutron scattering indicates that there is still much to be learned about the complex physical behavior of $HoMnO_3$.

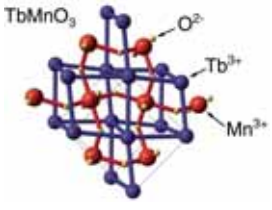

FIGURE 4: Crystal structure of $TbMnO_3$. Mn^{3+} ions are shown by red spheres, Tb^{3+} by blue spheres, and O^{2-} by yellow spheres.

Unlike $HoMnO_3$, the unit cell of $TbMnO_3$ is based on a simple cubic, rather than hexagonal, structure. The actual structure is more complicated, however, because lattice distortions break the cubic symmetry, as shown in Fig. 4. $TbMnO_3$ orders magnetically at 41 K in an incommensurate structure, meaning that the periodicity of the magnetic order does not match the periodicity of the crystal structure. Below 28 K, $TbMnO_3$ becomes ferroelectric. The application of a magnetic field of only a few Tesla can switch the direction of electric polarization in the ferroelectric state, indicating a strong coupling between the ferroelectric order and the magnetism in this material. The mechanism for this coupling is not understood, but may arise from the competing spin interactions. To determine a microscopic theory of this coupling mechanism, an unambiguous determination of the magnetic order is essential.

Figure 5 shows measurements of the magnetic order in $TbMnO_3$. At 43 K, above the magnetic ordering temperature, no magnetic scattering is observable. At lower temperatures, magnetic peaks emerge at various incommensurate positions, indicating that the periodicity of the magnetic structure does not match the crystal lattice.

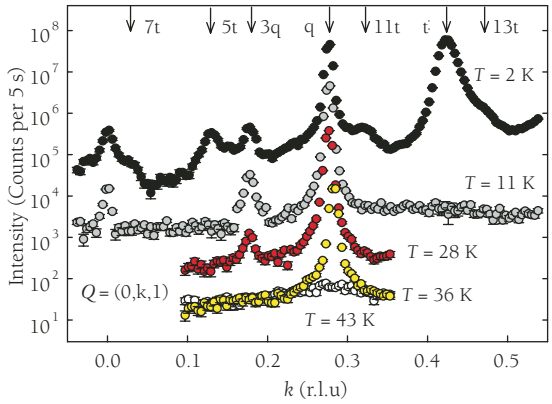

FIGURE 5: Neutron scattering measurements along the (0,k,1) direction in $TbMnO_3$ at different temperatures. Scans below 36 K are offset vertically for clarity. Arrows noted with q indicate scattering associated with the incommensurate Mn^{3+} order, and arrows noted with t indicate scattering associated with incommensurate Tb^{3+} order.

In order to determine this structure completely, we measured the scattering intensity at a large number of Bragg reflections above and below the ferroelectric transition temperature. Our experimental results were then compared to possible magnetic structures to find the model which best fit the data. Above the ferroelectric ordering temperature, $TbMnO_3$ has a longitudinally-modulated incommensurate structure. Below the ferroelectric ordering temperature, however, the magnetic order has a spiral structure that breaks the inversion symmetry of the lattice. This symmetry breaking by the magnetic order appears to be responsible for the emergence of ferroelectric order in $TbMnO_3$.

Neutron scattering has proven to be a critical tool in probing the magnetic properties of multiferroic materials. Our results for the magnetic structure and dynamics of $HoMnO_3$ and $TbMnO_3$ have provided important insights into these systems and will help pave the way towards greater understanding of the interactions between magnetic and ferroelectric order. The ability to tune magnetic properties with electric fields or ferroelectric properties with magnetic fields has great technological potential, but we must first understand the underlying physics of such materials in order to master their use.

REFERENCES

[1] O. P. Vajk, M. Kenzelmann, J. W. Lynn, S. B. Kim and S.-W. Cheong, Phys. Rev. Lett. **94**, 087601 (2005).

[2] M. Kenzelmann, A.B. Harris, S. Jonas, C. Broholm, J. Schefer, S. B. Kim, C. L. Zhang, S.-W. Cheong, O. P. Vajk and J. W. Lynn, to appear in Phys. Rev. Lett.

3D Imaging of Microstrains During Single Grain Deformation

T. Gnäupel-Herold
NIST Center for Neutron Research
National Institute of Standards and Technology
Gaithersburg, MD 20899-8562

F. Biancaniello and M. Stoudt
NIST Metallurgy Division
National Institute of Standards and Technology
Gaithersburg, MD 20899-8556

The study of single grain deformation represents a great opportunity for improving many aspects of materials deformation models that describe aggregate behavior. In principle, grains as constituents of polycrystals are single crystals, for which there is a large body of data available. However, other grains surround any given grain. Together, these grains impose highly complex boundary conditions on each other that cannot be reproduced in a single crystal deformation test. An example is an effect related to grain deformation called "tenting" (Fig. 1, lower image) in which the deformation of sub-surface grains causes protrusions or pits to form in the grains directly at the surface.

Due to the considerable difficulties in examining the 3D distribution of strains within a single grain, experimental data are scarce and, if available, were obtained by micro-beam [1] and surface scanning techniques [2]. The two principal methods that can provide non-destructive measurements of properties such as strain, grain shape and orientation on a single grain *in situ,* within a three-dimensional (3D) aggregate are neutron diffraction and synchrotron x-ray diffraction. To our knowledge, the mapping of strains *within* a grain by neutron diffraction has not yet been attempted. This is due to the requirement that beams approximately one order of magnitude smaller than the grain size in typical alloys (< 100 mm) are required for 3D mapping. The resulting reduction in intensity from the small beam size is accompanied by attenuation due to path lengths of > 1 mm within the material and by tight requirements on the positioning accuracy of the grain.

A different approach was chosen here in which these problems are circumvented by increased grain size. Using an alloy of high purity aluminum with 0.8 % magnesium grain sizes of up to 10 mm were achieved through a heat treatment. The grain used in the measurement is shown in Fig. 1. The size of the gage volume was 1×1×1 mm^3. Using a high-resolution mode of the BT-8 neutron diffractometer (low $\Delta\lambda/\lambda$), the (222) reflection at $2\theta \approx 90.4°$ was studied. As the typical full-width at half-maximum (FWHM) in the undeformed state is ≈ 0.03°, the instrumental contribution to the broadening after deformation can be neglected. The sample was strained in a uniaxial tensile test in five steps to a total strain of 12.5 %. After each straining step, the sample was placed in a four-circle goniometer for grain orientation (centering in χ perpendicular to the scattering plane), and then scanned in the X,Y and Z-directions of the sample table in 1 mm increments. The scan consisted of measuring the integrated intensity over a range of rocking angles ω (grain rotation in the scattering plane), thus allowing the spatial mapping of grain rotation and rocking curve broadening.

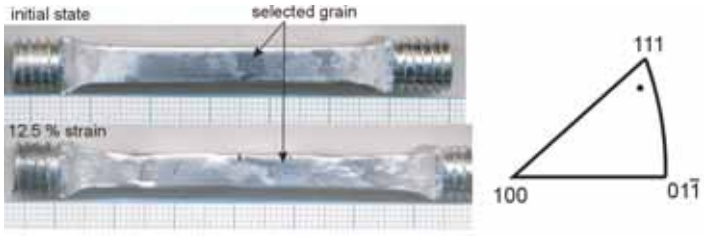

FIGURE 1: Tensile sample with the grain selected for measurement shown at the beginning and at the end of the experiment. The grid shown has a spacing of 1 mm. The stereographic projection on the right shows the grain's [111] direction close to the tensile axis.

Classic peak broadening analysis considers averages over a large number of grains. Peak broadening is split into two contributions: broadening from domain size and broadening from dislocation induced short-range strains. The deconvolution of the two effects requires measurements over a large range 2θ. The spatial mapping of a single grain, on the other hand, allows the unambiguous separation of strain broadening and rotation broadening. As a grain is subjected to non-uniform tri-axial stresses during deformation, different regions of the initially uniform grain are subjected to different levels of deformation (leading to different dislocation densities) as well as to rotations. The rotations lead to a fragmentation of the grain that can be measured from the positions of

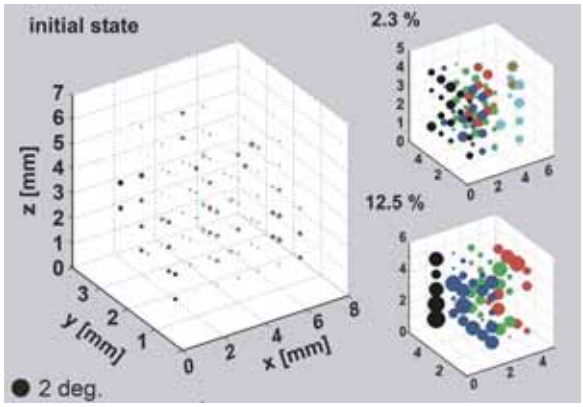

FIGURE 2: Spatial distribution of grain fragmentation $|\bar{\omega} - \omega_i|$. Seemingly missing points indicate locations where no rocking curve was found; this is partially due to rotations too large to fall within the scan range and partially due to the measurement location being outside the grain. The size of the circles is proportional to the absolute value of the grain fragmentation. The different colors are for better contrast.

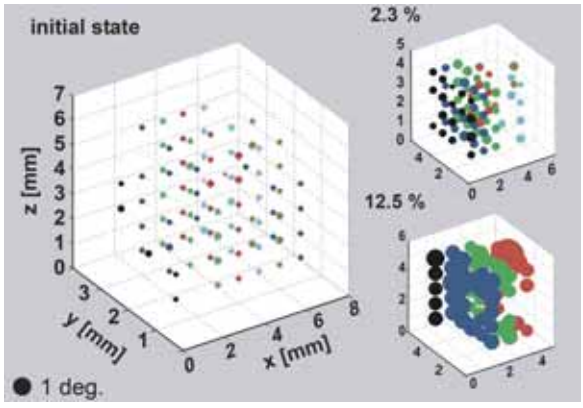

FIGURE 3: Spatial distribution of the FWHM (dots) of each rocking curve. The scale is identical to the scale employed in Fig.2.

rocking curves. The increase in grain fragmentation after each straining is shown in Fig. 3. Grain fragmentation is the absolute difference $|\bar{\omega} - \omega_i|$ between the centroids of the individual rocking curves ω_i and the grain average $\bar{\omega}$. The spatial distribution of the fragmentation indicates clustering of neighboring data points with similar values of fragmentation.

Regions in the grain with different dislocation densities yield broadened rocking curves. The spatial distribution of the FWHM of each curve is shown in Fig. 3. The grain average, i.e., the sum of all individual rocking curves, contains both broadening through mutually displaced rocking curves as well as the broadening of each curve itself (Fig. 4). The integral broadening for the entire grain is therefore always larger than the average FWHM and the average rotation (Fig. 5). As shown in Fig. 5, the contribution from rotations is always larger than that from the FWHMs and it seemingly dictates the slope of the grain average curve. This is evident from Fig. 4 that shows that the integral curve is very asymmetric due to large rotations within the grain. This indicates the strong presence of slip, which was also confirmed by the appearance of slip lines on the surface. In the extreme case of complete slip dominance as the sole mode of deformation, the rocking curves would exhibit very little broadening, but their centroid positions would differ up to several degrees. It is important to note that each individual rocking curve already contains both effects, but on a reduced scale. Each curve can be considered individually as a grain average that is formed by the superposition of rocking curves from even smaller regions. However, with decreasing dimensions of the gage volume (or grain) the broadening from rotations decreases as well, because the number of small angle grain boundaries within the gage volume decreases.

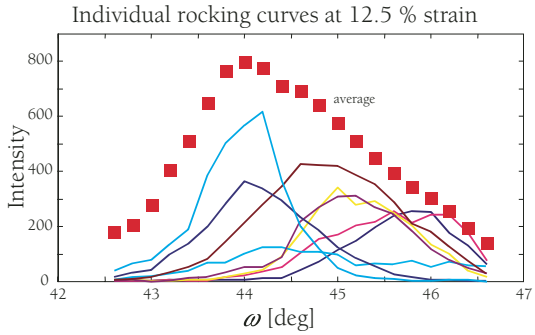

FIGURE 4: Selected individual rocking curves vs. the grain average. The individual curves have both different positions and FWHMs.

The experiment conducted here shows the feasibility of 3D strain scanning in a single grain. The sum of all individual rocking curves forms the integral curve of the grain whose broadening was studied at different levels of deformation. Between the two aspects of broadening – rotations and strain broadening – the contribution from rotation dominates the integral broadening.

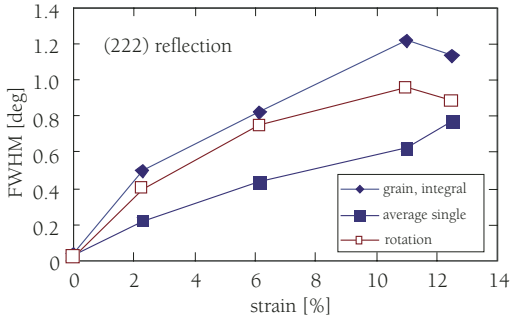

FIGURE 5: Separation of the broadening contributions from the average of the single FWHMs and the standard deviation of the individual rotations.

REFERENCES

[1] N. Tamura, J.-S. Chung, G. E. Ice, B. C. Larson, J. D. Budai, J. Z. Tischler, M. Yoon, in: *"Proceedings Materials Reliability in Microelectronics IX"*, A.H. Verbruggen, et al., eds., MRS Symp. 563, Warrendale PA, 1999.

[2] D. Raabe, M. Sachtleber, Z. Zhao, F. Roters, S. Zafferer, Acta Mater. **49**, 3433 (2001).

Neutron Residual Stress Measurements for Improved Safety of Gas Pipelines

M. Law
Australian Nuclear Science and Technology Organisation
PMB 1 Menai NSW 2234, AUSTRALIA

T. Gnäupel-Herold, H. J. Prask and V. Luzin
NIST Center for Neutron Research
National Institute of Standards and Technology
Gaithersburg, MD 20899-8562

Gas pipelines have an enviable safety record in transporting energy; this is due to detailed materials characterization and stress analysis. In many types of integrity analysis (fracture, fatigue, stress corrosion cracking, and weld cracking) the residual stresses in the pipe must be included. These residual stresses may arise from the forming operations involved in producing the coil and pipe, seam welding the pipe, and girth welding pipes together to form a gas pipeline. To perform integrity analysis, and to assess methods of manufacture and joining, it is necessary to measure these stresses. Neutron residual stress measurements offer many advantages in determining these stresses: the great penetrating power and non-destructive nature of the measurement means that stresses can be measured at a range of depths with good spatial resolution. The evolution of residual stresses in pipeline manufacture was investigated by neutron diffraction measurements at various stages in the manufacturing process: the strip the pipes are formed from, the finished pipe, and the stresses arising from welding these pipes together to make a pipeline.

Residual stresses are of special significance in gas pipelines as they are designed with smaller safety factors than other major engineering components. For example, in engineering structures the factor of safety with respect to the yield strength is typically 3 or more, with pipelines this is 1.25 (ASME B31.8).

High gas throughput dictates high gas pressure, which makes the use of high strength steels economical. The use of such materials in pipe manufacture invariably creates high levels of residual stresses that may contribute to premature failure by fatigue, stress corrosion cracking, fracture, or lead to unacceptable deformation.

FIGURE 1: Left: Circumferential rupture in the hydrotest, and Right: measurement geometry for the corresponding hoop direction.

In the manufacturing process, after a series of controlled temperature rolling operations, the resulting strip is wound onto a coil, and unwound from this to be fed into the pipe mill where the pipe is formed by bending and longitudinal seam welding followed by compressive sizing and expansion in the mill hydro-test (Fig. 1). Each of the mechanical processes introduces cold work, thus increasing both the strength and the through-thickness residual stresses. Failure mechanisms such as stress corrosion cracking, hydrogen assisted cold cracking, and fracture are all affected strongly by residual stresses. Any study of these threats to pipeline integrity must begin by assessing the residual stresses in the as-built pipeline. Through-thickness stresses are preserved in pieces of pipe even shorter than the pipe diameter, thus allowing easy access in neutron measurements (Fig. 1). An additional source of high stresses is welding which may produce high tensile stresses (up to the yield stress) balanced by lower compressive residual stresses elsewhere in the component. As post-weld heat treatment is not common in constructing gas pipelines the resulting stress state is essentially the initial residual stress state at the beginning of service of the pipe. Due to the lack of published data on residual stresses in shielded and manual metal arc welds common in gas pipelines there is considerable interest in non-destructive measurements of these stresses.

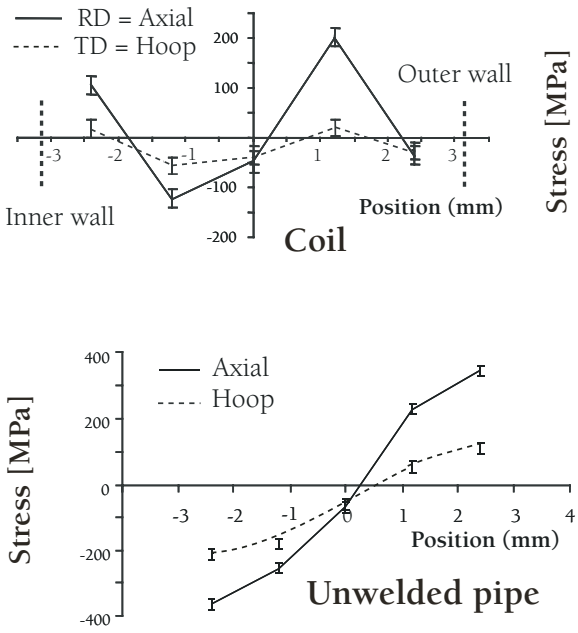

FIGURE 2: Through-thickness stresses after coiling (left) and bending (right) into pipe shape.

The residual stress measurements were performed on the BT-8 instrument at the NIST Center for Neutron Research (NCNR). Measurements were made without cutting the full ring of pipe so as to fully preserve the stress field. A nominal gauge volume of 1 x 1 x 1 mm^3 was used. Unstressed d-spacings were measured on small coupons in the weld, heat affected zone (HAZ), and in the parent material.

Due to the severity of the coldwork at each stage of the manufacturing process the stresses change substantially between stages (Fig. 2). The depth dependence of the stresses is consistent with stresses introduced by plastic bending (coil) and subsequent unbending (pipe). However, as the coldwork (accumulated plastic strain) increases from coil to pipe bending the maximum stresses found near the inner and outer surfaces increase as well. The stresses in the unwelded pipe reach up to 60 % of the specified minimum yield strength of ≈ 480 MPa. After girth welding even higher stresses are found in the vicinity of the weld but not in the immediate weld area itself (Fig. 3). Tensile stresses exceeding the minimum yield strength are found at distances of about 2 × wall thickness on both sides of the weld.

An explanation for these high stresses in the parent metal is that as the cooling, shrinking weld bead is restrained by the parent material adjacent to it, the parent material goes into compression. At the same time the parent material is also being heated which causes it to expand. The expansion increases the compressive stresses on the adjacent parent material as it is restrained by parent material further away from the weld. The compressive stress exceeds the yield strength and the material yields compressively. As the weld pool and adjacent material continue cooling, the parent material adjacent to the weld is restrained from shrinking. The magnitude of these tensile stresses is in accord with published data showing hoop residual stresses to be primarily between 0.2 and 1.0 times the yield stress but sometimes outside these bounds.

The low hoop stresses (compared to those seen in the parent material) in the weld are a result of the weld contraction being restrained by the adjacent parent material, which is also heated by the weld. The weld metal yields under tensile stress. When the adjacent parent metal cools and contracts, low tensile hoop stresses are the result. In the parent material the maximum value of residual stress in the hoop direction is in the range of the actual yield stress (between 543 MPa and 575 MPa) and well above the nominal yield strength. If an integrity analysis had assumed nominal yield strength magnitude residual stresses, the actual stresses are much higher and the analysis would be inaccurate and inadequately conservative.

The residual stresses in the axial direction were between 60 % and 80 % of the yield strength. As stresses in this direction have the greatest effect on flaws in the girth weld, the assumption that residual stresses are of yield stress magnitude would lead to an overly small allowable defect size, thus sentencing many adequate welds to repair and adding considerably to construction time and costs. The acceptable defect size in the girth weld is a function of the stress perpendicular to the weld, i.e. the axial stress. It is customary to assume that the magnitude of residual stresses are equal to the yield strength, but in this case the axial stresses are approximately 2/3rds of the yield stress.

In summary, the results presented here provide a complete picture of the through-thickness residual stresses in gas pipeline at different stages of the manufacturing process. It was found that peak stress levels increase substantially with each manufacturing stage due to increasing amounts of cold work. After welding the peak stresses are well above the nominal yield strength. This is important for reasons of pipeline integrity such as stress corrosion cracking, and for calibrating and verifying numerical models of residual stress evolution.

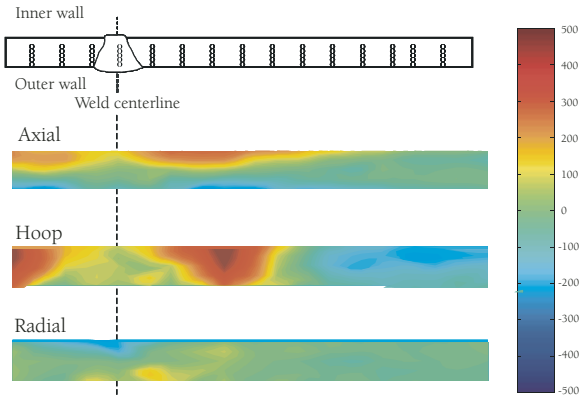

FIGURE 3: Stresses (MPa) after girth welding.

REFERENCES

P. Michaleris "Incorporation of residual stresses into fracture mechanics models" Edison Welding Institute (EWI) report 7412 (1996)

Crystal Orientation from Laue Diffraction Patterns

A. Santoro and B. H. Toby
NIST Center for Neutron Research
National Institute of Standards and Technology
Gaithersburg, MD 20899-8562

Laue diffraction provides a quick method of crystal alignment for crystallographic or triple-axis measurements, potentially replacing many hours of tedious work on a triple-axis instrument. Recent work has shown that a single Laue measurement, requiring only minutes of neutron beam time, can be sufficient to derive the orientation matrix of a randomly oriented crystal of known or even unknown lattice parameters. The theory and user-friendly computer programs have been developed that show how this may be accomplished.

The geometry we use for analysis of Laue images is illustrated in Fig. 1. As shown in this figure, the stereographic and gnomonic projections of reciprocal vectors or diffracted beams are directly related to the locations of the diffracted beams seen in a Laue pattern. Knowledge of the lattice geometry is not needed to obtain these projections. Further, the projections may be observed from any point of view, regardless of the actual crystal setting, which facilitates detection of symmetry elements and offers the most convenient way of selecting three non-coplanar reflections to be used to index the reciprocal lattice. Although symmetry and cell dimensions are not directly derivable from Laue diffraction patterns, our recent work shows that axial ratios and interaxial angles can be derived from Laue images.

In our algorithm, we assign Miller indices 100, 010 and 001 to the three vectors corresponding to the selected reflections. This fixes the directions of the three reciprocal lattice directions and the angles between them, but not the reciprocal unit cell lengths. Selection of a fourth vector, which is assigned index 111, defines the relative magnitudes of the reciprocal unit cell, a^*/b^*:1:c^*/b^*, and allows the Laue pattern to be indexed. It should be noted, that the cell produced in this fashion may not reflect the full lattice symmetry, and thus may not be the conventional unit cell, but the two cells will be closely related and previous work allows the lattice symmetry to be easily discovered. [1, 2]

Recent work at HIFR has demonstrated the value of an orientation matrix for triple-axis measurements [3]. The orientation matrix relates two Cartesian coordinate systems: one system, labeled as $OX_RY_RZ_R$, which has the beam running along Y_R, and X_R pointing down, as shown in Fig. 1, is defined as the instrument reference system. The second orthogonal system, labeled as $OX_CY_CZ_C$, is defined relative to the designated reciprocal cell with $\hat{X}c = \hat{a}^*$, $\hat{Z}_c = \hat{a}^* \times \hat{b}^* / |\hat{a}^* \times \hat{b}^*|$, and $\hat{Y}_c = \hat{Z}_c \times \hat{X}_c$, where the caret indicates a unit vector. NCNR work shows that the orientation matrix, **U**, of Busing and Levy [4] may be derived directly from Laue images using the following procedure. We can convert the coordinates of a reciprocal lattice point, *hkl*, expressed as column vector $\boldsymbol{h}$, to the system $OX_CY_CZ_C$ (column vector $\boldsymbol{x_C}$) using equation $\boldsymbol{x_C} = \mathbf{B}\,\boldsymbol{h}$, where

$$\mathbf{B} = \begin{pmatrix} a^* & b^*\cos(\gamma^*) & c^*\cos(\beta^*) \\ 0 & b^*\sin(\gamma^*) & -c^*\sin(\beta^*)\cos(\alpha) \\ 0 & 0 & c^*\sin(\beta^*)\sin(\alpha) \end{pmatrix}.$$

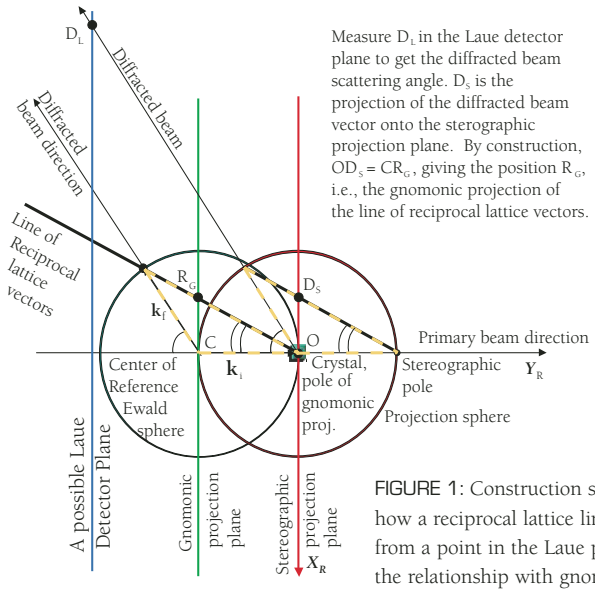

FIGURE 1: Construction showing how a reciprocal lattice line is derived from a point in the Laue pattern and the relationship with gnomonic and stereographic projections.

We select two reciprocal vectors, $\boldsymbol{h}_1$ and $\boldsymbol{h}_2$ of known indices for these reflections (e.g. $h_1k_1l_1$ and $h_2k_2l_2$) and with known Cartesian coordinates in the instrument reference system, $X_{R1}Y_{R1}Z_{R1}$, and $X_{R2}Y_{R2}Z_{R2}$. We use matrix **B** to determine the components of $\boldsymbol{h}_1$ and $\boldsymbol{h}_2$ in the crystal Cartesian system.

We then define a unit-vector triplet $\boldsymbol{tc_1} = \boldsymbol{h_1}$; $\boldsymbol{tc_3} = (\boldsymbol{h_1} \times \boldsymbol{h_2})/|\boldsymbol{h_1} \times \boldsymbol{h_2}|$; $\boldsymbol{tc_2} = \boldsymbol{tc_3} \times \boldsymbol{tc_1}$. From this triplet we calculate a new matrix, $\mathbf{T_c}$, where matrix element T_{cij} is the *X, Y* or *Z* component (for *j*=1,2 or 3, respectively) of $\boldsymbol{tc_i}$ in the crystal Cartesian system ($OX_CY_CZ_C$). Likewise, we compute matrix, $\mathbf{T_R}$, that relates the same set of unit vectors to the instrument reference system ($OX_RY_RZ_R$) in a similar fashion. To obtain the orientation matrix, **U**, we note that it must relate these coordinate systems so that $\mathbf{T_R} = \mathbf{U}\,\mathbf{T_c}$. Since $\mathbf{T_c}$ is orthogonal, we solve for the orientation matrix as $\mathbf{U} = \mathbf{T_R}\,\mathbf{T_c}^{\mathbf{T}}$. In practice, multiple reciprocal lattice vectors are used in this procedure to reduce experimental errors.

REFERENCES

[1] A. Santoro, A. D. Mighell, Acta Cryst. A **26**, 124 (1970).
[2] V. L. Himes, A. D. Mighell, Acta Cryst. A **43**, 375 (1987).
[3] M. D. Lumsden, J. L. Robertson, M. Yethiraj, J. Appl. Cryst. **38**, 405 (2005).
[4] W. R. Busing, H. A. Levy, Acta Cryst. **22**, 457 (1967).

Very Compact High Performance Microchannel Plate Neutron Collimators

A. S. Tremsin
University of California Berkeley
Berkeley, CA 94720

D. F. R. Mildner
National Institute of Standards and Technology
NIST Center for Neutron Research
Gaithersburg, MD 20899-8563

W. B. Feller
NOVA Scientific, Inc
Sturbridge, MA 01566

R. G. Downing
NOVA Scientific, Inc.
Sturbridge, MA 01566
(Currently at the NIST)

Söller slit collimators usually define the angular spread of a neutron beam. A typical collimator consists of many parallel plates many centimeters in length that are coated with neutron absorbing material. We have modeled and tested a new type of neutron collimator made of ^{157}Gd-doped microchannel plates (MCPs) with only a few millimeters thickness, and yet the rocking curve is sharper than conventional 0.5° collimators. The rocking curve for existing MCP technology can be as sharp as 0.2° Full-Width-at-Half-Maximum (FWHM) and experiments with collimators only 0.6 mm long confirm the accuracy of the numerical model.

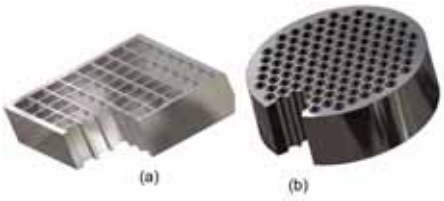

FIGURE 1: a) Square-channel and b) circular-channel MCPs doped with ^{157}Gd.

Thermal neutron beams are usually collimated with a Söller slit collimator, comprised of neutron-absorbing films supported on thin spacers, e.g., thin single crystal silicon wafers or mylar films with absorbing coatings [1-3]. The shorter the collimator, the narrower the transmitting channel required to achieve the same level of collimation. Recently, the stacking of 160 μm thick silicon wafers coated with 4 μm of gadolinium metal achieved a 2.75 cm long collimator with performance comparable to conventional collimators [2]. However, collimators can be substantially more compact if the absorber-spacers are reduced to a thickness of few microns. The structural dimensions of commercially available microchannel plates (MCP) meet these requirements with typical channel sizes of 6 μm to 15 μm and 2 μm to 3 μm walls thicknesses. We have computer-modeled and tested available MCPs (doped with ^{157}Gd) as prototypical, very compact and highly efficient thermal neutron collimators.

Microchannel plates typically consist of millions of open channels fused together into a monolithic structure, a section of which is shown in Fig. 1. The channels are usually circular, hexagonal or square in cross-section, 6 μm to 12.5 μm wide and spaced 7.5 μm to 15 μm center-to-center. The thickness of the disk is typically 40 to 250 times larger than the channel diameter (equivalent to 0.24 mm to 3.75 mm), and MCPs can be fabricated with a cross sectional area as large as 10x10 cm^2. Whenever the neutron trajectory transects the microchannel wall, neutron absorption occurs from its reaction with ^{157}Gd (thermal neutron capture cross section ≈ 259 000 barns).

Numerical modeling of the "ideal" rocking curve shown in Fig. 2a, indicates that MCPs with their tighter geometrical packaging are an attractive alternative to existing neutron collimator technology. Increasing the wall composition fraction of $^{157}Gd_2O_3$ from x = 0.003 to .03 substantially

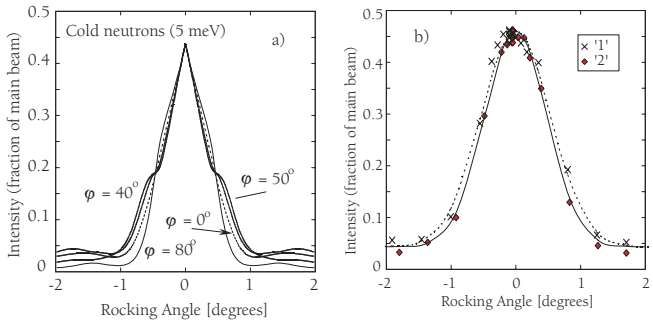

FIGURE 2: a) Modeled rocking curve for aspect ratio L/D = 75:1. Aspect ratios up to 250:1 are readily available. b) Measured rocking curve.

improves the performance of collimators with aspect ratios of L/D = 250:1, though further increases of ^{157}Gd concentration do not result in any better collimation. The model does not include reflection and scattering processes, though the latter will give a moderate smoothing of the triangular shape of the 'ideal' rocking curve.

The correctness of our model for the MCP neutron collimators has been confirmed by preliminary experimental measurements. The microchannel plates tested (L/D =75:1, 8 μm circular channels with 11.5 μm centers doped with x = 0.03 of ^{157}Gd) were systematically rotated and tilted in the beam to map the neutron transmission. The results are summarized in Fig. 2b showing the collimation in two orthogonal planes (curves 1 and 2). The predicted performance of the same MCP is only slightly better. The measured maximum transmission (≈ 0.44) is equal to the open area fraction of the microchannel plates. MCP open areas of 60 % to 90 % are common.

The model indicates that transmission and collimation comparable to that of a conventional 0.5° neutron Söller collimator is achievable and sharper rocking curves are possible using thicker MCP collimators. Furthermore, solid-core MCP collimators are feasible for significantly higher aspect ratios constructed using 25 mm thick pieces with channels widths down to about 6 μm, producing an L/D ratio of > 4000 [4]. The MCPs enable shorter neutron optic layouts and better collimation than existing technology.

REFERENCES

[1] Th. Krist and F. Mezei, Nucl. Instrum. Methods, **A450**, 389 (2000).
[2] L. D. Cussen, *et al.*, Nucl. Instrum. Methods, **A471** 392 (2001).
[3] C. Petrillo, *et al.*, Nucl. Instrum. Methods, **A489** 304 (2002).
[4] A. S. Tremsin *et al.*, IEEE Trans. Nuc. Sci. **51**(3) 1020 (2004).

INAA for Small Samples and New SRMs for Solid Sampling Instruments

R. Zeisler
Analytical Chemistry Division
National Institute of Standards and Technology
Gaithersburg, MD 20899-8395

A significant problem in the use of the emerging solid and small sample techniques is a general lack of suitable certified reference materials and Standard Reference Materials® (SRMs) used for calibration and quality assurance purposes. Essentially no SRMs are certified for the small sample sizes typically used [1] and direct utilization of most existing SRMs in solid sampling analysis procedures is often difficult or even impossible either because trace components are not sufficiently homogeneously distributed in the sample, or their homogeneous distribution has not been validated. To study the homogeneity of SRMs at small sample sizes we have developed the established Instrumental Neutron Activation Analysis (INAA) procedures of the NIST Nuclear Methods Group [2] to accommodate the small samples with essentially no degradation of uncertainty in the analytical results. These procedures have since become an integral part of the development of a first material of a new generation of highly homogeneous SRMs.

Based on models linking sample mass (m) to the homogeneity of particulate materials, Kurfürst *et al*. [3] have proposed an elemental homogeneity factor H_e that gives the relative standard deviation in percent for the element of interest if 1 mg samples were repeatedly analyzed and no analytical uncertainty were to influence the result $H_e = u_{HET}\sqrt{m}$ [4]. Experimental determination of u_{HET} by INAA requires that small samples are prepared for INAA in the form of pellets either by directly pelletizing 1 mg amounts of material in a 3 mm diameter die, or preparing 70 mg to 100 mg amounts in a 13 mm diameter die and then sub-sampling these pellets at 0.5 mg to 2 mg with a 1.5 mm diameter corer. These small samples provide nearly ideal sample geometries for high-precision assay by INAA. The procedural relative uncertainties are generally 0.5 % to 0.7 % and very suitable for the intended purpose, with counting statistics varying from 0.1 % to several percent depending on the activity of the element. To minimize the counting uncertainty, these experiments mainly utilized a newly installed set of three high-resolution gamma-ray spectrometers with ultra-high count rate capabilities. Count rates in short and intermediate half-life assays reached up to 50 000 s^{-1}. The spectrometers were evaluated for high accuracy analysis of metals where expanded relative uncertainties of smaller than 0.3 % were achieved. The long counts were carried out on a conventional detector system equipped with a sample changer.

Investigations of homogeneity by INAA encompassed a number of different materials before a sediment from the Patapsco River, Maryland, the SRM 2702 Inorganic Marine Sediment, was selected for development of the new generation SRM for solid sampling (small sample) analytical techniques. The new material, SRM 2703, was produced with a smaller particle size distribution than the original to assure homogeneity. For the acceptance of the material, twelve test portions of SRM 2703 were analyzed by INAA, and the heterogeneity components were calculated by subtracting the analytical uncertainties from the observed experimental uncertainty. The results for elements with counting statistics of 1% relative or smaller are shown in Table 1. The Kurfürst homogeneity factors are very similar for these elements and reveal homogeneity for the observed elements at sample sizes of 1 mg or smaller. Since the observed elements ranged in their concentrations from major constituents (Al, Fe) to trace (Mn, Zn) and ultra-trace (Sc, V) constituents of different origin, the material was accepted for certification. Other solid sampling techniques subsequently confirmed homogeneity for additional critical elements such as Ni and Pb.

TABLE 1. Homogeneity test results obtained by INAA for small samples of SRM 2703. Reported are elements with low counting uncertainties. Uncertainties are % relative values (1 s) for each component.

Element	Mass (mg)	Observed Uncertainty	Counting uncertainty	Other uncertainties (estimate)	Uncertainty due to heterogeneity	Kurfürst homogeneity factor (√m)
Al	0.8	0.92	0.37	0.5	0.68	0.61
As	0.7	2.22	0.84	0.7	1.93	1.62
Ce	0.7	1.17	0.91	0.5	0.54	0.45
Co @ 1723 keV	0.7	1.26	0.89	0.5	0.74	0.62
Co @ 1332 keV	0.7	1.33	0.88	0.5	0.86	0.72
Fe @ 1099 keV	0.7	1.26	0.77	0.5	0.86	0.72
Fe @ 1292 keV	0.7	1.09	0.72	0.5	0.65	0.54
La @ 487 keV	0.7	1.30	0.79	0.7	0.76	0.63
La @ 1596 keV	0.7	1.39	0.78	0.7	0.91	0.76
Mn @1811 keV	0.8	1.08	0.50	0.7	0.65	0.58
Mn @2113 keV	0.8	1.04	0.66	0.7	0.39	0.35
Na @1368 keV	0.8	1.21	0.87	0.7	0.47	0.42
Na @2754 keV	0.8	0.80	0.79	0.7	-*	-*
Sc @ 889 keV	0.7	1.00	0.99	0.5	-*	-*
Sc @ 1121 keV	0.7	1.16	0.99	0.5	0.34	0.28
Th	0.7	1.51	1.03	0.5	0.98	0.82
V	0.8	1.49	0.90	0.5	1.08	0.96
Zn	0.7	1.31	1.10	0.5	0.51	0.42

** Factor could not be calculated because the observed experimental uncertainty is similar to the analytical uncertainty*

The new generation SRM 2703 Sediment for Solid Sampling (small sample) Analytical Techniques provides certified values for 23 elements, reference values for 7 elements, and information values for 8 elements for a minimum sample size of 0.7 mg.

REFERENCES

[1] Survey of Reference Materials, International Atomic Energy Agency, Vienna, Austria, IAEA-TECDOC-854 (1995), IAEA-TECDOC-880 (1996).

[2] R. R. Greenberg, R. F. Fleming, and R. Zeisler, Environm. Intern. **10**, 129 (1984).

[3] C.O. Ingamells, P. Swizer, Talanta **20**, 547 (1973).

[4] U. Kurfürst, K.-H. Grobecker, M. Stoeppler, Trace Elem. **3**, 591 (1984).

Serving the Science and Technology Community

Growth continues to mark user participation at the NCNR, even after a dozen years of operation as North America's premier neutron scattering facility. Existing instruments are regularly improved, and several new ones are being built, the latter to become available to users in the next two to three years.

The past year saw a rise in proposal pressure of about 30 % from the previous year. While we do not necessarily expect similar increases over the long term, it is clear that we must continue to expect continued high demand for access to NCNR instruments. In response to these pressures, this year the NCNR received a significant increase in funding to expand access to the NCNR through the user program. Upgrading instruments and then operating them in a robust user program will accomplish this enhancement. During the past year the NCNR expanded access for the reflectometer instruments and accelerated work on the new triple axis spectrometers that will join the user program when completed.

We continue to make improvements to the many services that users count on for accessing and using the NCNR. The process for coordinating user activities is very different from what it was just a few years ago. Mass mailings and stacks of paper proposal forms have been replaced by online proposal submission and review. A new User Office has been established to aid users and visitors. In the coming year, our databases will be completely revamped to integrate procedures such as site access for users, safety training, instrument and equipment scheduling, and publication of research results.

The NCNR User's Group (NUG) provides an independent forum for users to give feedback on the operation of the NCNR. The NUG is organizing its first election of officers and developing an online tool to collect feedback from the NCNR user community. The results from last year's user survey continue to influence how we allocate resources supporting data analysis software, sample environment equipment, user access and health physics training.

CENTER FOR HIGH RESOLUTION NEUTRON SCATTERING

The Center (CHRNS) represents a partnership between NIST and the National Science Foundation (NSF) that has been crucial to the development and operation of many of the user instruments at the NCNR. The five year cooperative agreement between NIST and NSF was renewed this year. CHRNS offers a suite of instruments unmatched in North America for the investigation of the structure and dynamics of solids by neutron scattering, probing length scales from 1 nm to about 10 μm and energies from about 30 neV to approximately 100 meV. Most of the proposals we receive ask for time on one of the CHRNS instruments, which include a 30 m SANS diffractometer, a high-resolution USANS diffractometer, the backscattering spectrometer (HFBS), the disk-chopper spectrometer (DCS), the neutron spin-echo spectrometer (NSE), and the cold-neutron triple-axis spectrometer (SPINS). CHRNS also plays a major role in the NCNR's educational activities, through its annual weeklong summer school on neutron scattering, for example, and its outreach efforts.

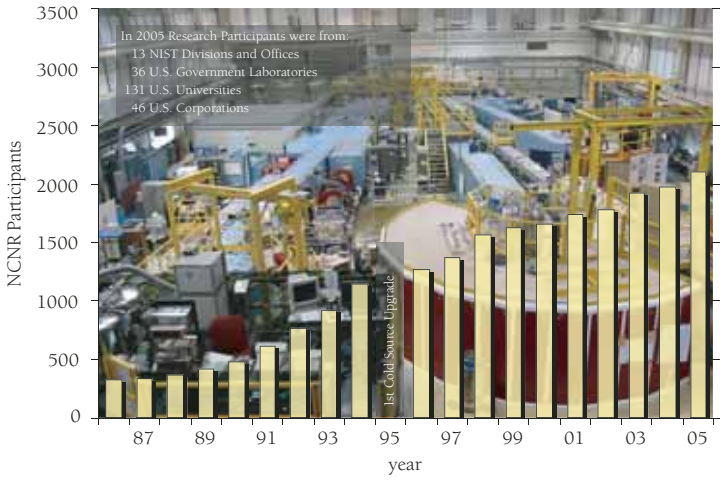

ELEVENTH ANNUAL SUMMER SCHOOL

Every June, we host a summer school to introduce young scientists, mainly graduate students and postdoctoral researchers, to the theory and practice of neutron scattering. Ever popular, the 2005 event attracted 84 applications for the 32 available slots. Sponsored by CHRNS, its flavor alternates in successive years between structural studies by SANS and reflectometry and dynamics studies using neutron spectroscopy. Its format centers on hands-on instruction at the instruments with students performing actual experiments. Participants chose three out of four

experiments that examined the dynamics of systems ranging from methyl iodide, C_{60}, manganites, and microemulsion droplets, using time-of-flight, backscattering, and spin-echo spectrometers. The experiments were bracketed by a half day of lectures at the start of the school and by two advanced-level invited talks on bio-membranes and complex magnetic oxides at the end. On the last day, the students learned how to choose the best spectrometer for a particular experiment, and gave group presentations to NCNR staff summarizing the experiments that they had performed. The instructors' commentary on the presentations and the students' evaluations of the instruction indicated that they departed friends, with some good proposals and experiments foreseen in coming years.

COLD NEUTRONS FOR BIOLOGY AND TECHNOLOGY

The Cold Neutrons for Biology and Technology (CNBT) research initiative is a consortium dedicated to studies of biological membrane systems, funded by the National Institutes of Health (NIH-NCRR), with contributions from NIST, the University of California at Irvine, the University of Pennsylvania, and Johns Hopkins University. In addition to the above-mentioned institutions, the CNBT partnership encompasses investigators from Rice University, Carnegie Mellon, Duke, and the NIH-NIAAA, as well as collaborators from the Los Alamos National Laboratory. The CNBT collaboration includes the Advanced Neutron Diffractometer/Reflectometer (AND/R) for structural biology, 10 % of the time on the NG-7 30 m SANS diffractometer, a fully equipped biology laboratory, and two state of the art computer clusters – one at NCNR and one at UC Irvine – for molecular dynamics simulations. This combination provides a powerful set of capabilities for US researchers interested in structural biology problems that involve membrane systems.

The ExxonMobil Research and Engineering Company is a member of the Participating Research Team (PRT) that operates, maintains, and conducts research at the NG-7 30 m SANS instrument and the NG-5 Neutron Spin Echo Spectrometer. Their mission is to use those instruments, as well as other neutron scattering techniques available to them at NCNR, in activities that complement research at ExxonMobil's main laboratories as well as at its affiliates' laboratories around the world. The aim of these activities is to deepen understanding of the nature of ExxonMobil's products and processes, so as to improve customer service and to improve the return on shareholders' investment. Accordingly, and taking full advantage of the unique properties of neutrons, most of the experiments we conduct here at NCNR use SANS or other neutron techniques to study the structure and dynamics of hydrocarbon materials, especially in the fields of polymers, complex fluids, and petroleum mixtures. ExxonMobil regards its participation in the NCNR and collaborations with NIST and other members of the scientific community not only as an excellent investment for the company, but also as a good way to contribute to the scientific health of the nation.

INDEPENDENT PROGRAMS

The Neutron Interactions and Dosimetry (NI&D) Group (Physics Laboratory) provides measurement services, standards, and fundamental research in support of NIST's mission as it relates to neutron technology and neutron physics. The NI&D group is in the forefront in basic research with neutrons in the measurements of symmetries and parameters of the weak nuclear interactions, addressing fundamental issues that are important in the understanding of theories of evolution of the cosmos. The neutron interferometry program provides the world's most accurate measurements of neutron coherent scattering lengths and tests fundamental aspects of quantum mechanics. This group is also among world leaders in developing ^{3}He based neutron polarization and analysis techniques. The NI&D group, which operates nation's premier high-resolution neutron imaging facility, has pioneered the development of neutron phase imaging and the application of neutrons imaging in fuel cell research. The NI&D group has initiated a vigorous and accelerated program to develop advanced neutron spectrometry techniques and effective neutron interrogation and measurement standards and methods for national defense and homeland security needs. The NI&D group also improves neutron cross-section standards through both evaluation and experimental work and maintains, and disseminates measurement standards for neutron dosimeters, neutron survey instruments, and neutron sources.

The **Smithsonian Institution's Nuclear Laboratory for Archeological Research** is part of the Anthropology Department at the American Museum of Natural History. It has had a productive 28 year partnership with the NCNR, during which time it has chemically analyzed over 30 500 archaeological artifacts by Instrumental Neutron Activation Analysis (INAA), drawing extensively on the collections of the Smithsonian, as well as on those of many other institutions in this country and abroad. The chemical analyses provide a means of linking these diverse collections together to study continuity and change involved in the production of ceramic objects. INAA data are used to determine if groups of ceramics have been made from the same or different raw materials. The ceramics can then be attributed to geographic regions, specific sources, workshops and even individual artists. The ability to use chemical composition to link pottery groups found in archaeological contexts to specific production locations is currently being used to examine the manufacture and distribution of lead glazed pottery in Mexico and the northern Spanish borderlands of California and the American southwest.

The **Polymers Division** of the Materials Science and Engineering Laboratory works with the NCNR and industrial partners in several program areas including electronics materials, nanomanufacturing, self-assembling systems, polyelectrolyte solutions, and biomaterials. Several neutron-based methods are employed in these studies including small angle neutron scattering, neutron reflectometry, neutron diffraction, and neutron spin echo spectroscopy. In the electronics materials program, the NCNR provides unique measurements that impact next-generation photolithography, including the *in-situ* distribution of aqueous base and water in ultrathin polymer films and the measurement of the spatial extent of the deprotection reaction in model 193 nm and EUV photoresist materials. In the nanomanufacturing program, neutron techniques are used to elucidate the underlying principles of dispersing and manipulating advanced materials such as carbon nanotubes and block copolymer thin films. In the biomaterials program, NCNR instruments provide important structure and dynamics information for tissue engineering, regenerative medicine, and protein preservation.

The **Nuclear Methods Group** (Analytical Chemistry Division, Chemical Sciences and Technology Laboratory) develops and applies nuclear analytical techniques for the determination of elemental compositions, striving for improvements in accuracy, sensitivity, and selectivity. The group has pioneered the use of cold neutrons as analytical probes in two methods: prompt-gamma activation analysis (PGAA) and neutron depth profiling (NDP). In PGAA, the amount of a particular analyte is measured by detecting characteristic gamma rays emitted by the sample while it is being irradiated in an intense cold-neutron beam. NDP is another in-beam method that can characterize the concentration of several elements as a function of depth in the first few microns below a surface. It accomplishes this by energy analysis of the charged particles emitted promptly during neutron bombardment. In addition to NDP and PGAA, the group has a high level of capability in two more conventional methods, instrumental and radiochemical neutron activation analysis (INAA and RNAA). In aggregate, the techniques used by the group are a powerful set of complementary tools for addressing analytical problems for both in-house and user programs, and are used to help certify a large number of NIST Standard Reference Materials.

The **Center for Food Safety and Applied Nutrition**, U.S. Food and Drug Administration (FDA), directs and maintains a neutron activation analysis (NAA) facility at the NCNR. This facility provides agency-wide analytical support for special investigations, and emergency response, complementing other analytical techniques used at FDA with instrumental, neutron-capture prompt-gamma, and radiochemical NAA procedures, radioisotope x-ray fluorescence spectrometry (RXRFS), and low-level gamma-ray detection. This combination of analytical techniques enables diverse multi-element and radiological information to be obtained for foods and related materials. The NAA facility supports agency quality assurance programs by developing in-house reference materials, by characterizing food-related certified reference materials with NIST and other agencies, and by verifying analyses for FDA's Total Diet Study Program. Studies include development of RXRFS methods for screening food ware and food packaging materials for the presence of Pb, Cd and other potentially toxic elements, use of instrumental NAA to investigate bromate residues in bread products, development of Compton suppression techniques for instrumental NAA, and use of prompt-gamma NAA to determine elemental compositions of NIST Ephedra Standard Reference Materials and commercial dietary supplements.

Operations

The NIST reactor (NBSR) operated for 197 full power (20 MW) days, on all but six days as scheduled. This accounts for a reliability (days operated on day scheduled) of 97 % for FY2005. A typical operating year consists of approximately 250 full power beam days. For FY2005, the NBSR operated less because of a scheduled three month outage to perform periodic maintenance on the reactor. Maintenance activities during this extended shutdown included replacement of the reactor control rods, improvement of the rods' seals through extensive in-place machining and alignment, and replacement of the heavy water in the main and auxiliary systems. The Reactor Operations and Engineering staff also performed a remote inspection of the reactor vessel interior, resulting in a detailed video record of the reactor vessel internals for benchmarking and future reference. The condition of the reactor is excellent. The extended shutdown was coordinated with the installation of the front end of the new Multi-Analyzer Crystal Spectrometer (MACS) at NG-0. Because of the close proximity of the MACS instrument to the NCNR cold source, installation work in this area must be performed with the reactor shutdown.

The NBSR is operating under a provision of the U.S. Nuclear Regulatory Commission (NRC) that allows for continued operation after submittal of a timely application for license renewal. The original license for the NBSR expired on May 16, 2004 and NIST submitted a timely renewal application on April 9, 2004. NRC procedures are being followed in providing the schedule for the next steps in the NBSR license renewal process. Work continues on reactor analysis and plant improvements in preparation for these steps. Highlights from this year included replacement of reactor nuclear instrumentation and several console displays during the extended outage. We continue to study and analyze options for a full replacement of the control panel with an improved, ergonomic design. Other reactor license renewal goals were met by replacing all of the secondary cooling water pumps and motors and with the completion of the cooling tower replacement program. We also completed a modernization of the reactor building ventilation system and are currently replacing the RT2 in-core pneumatic sample assembly.

Operator Richard Beasley at the control console with refurbished displays.

We have been very active in a variety of outreach activities with state and local government officials and with members of neighborhood organizations in an effort to share information about NIST, the NCNR, and about the ongoing license renewal process. On May 24, the NCNR participated in a public meeting at the Gaithersburg Community Center hosted by NIST called "Getting to Know the National Institute of Standards and Technology: Neighbor, National Resource, and World-Class Laboratory".

Facility Developments

SAMPLE PREPARATION AND CHARACTERIZATION LABORATORIES

The NCNR completed in 2005 the renovation of three or our larger laboratories, nearly doubling the space and equipment available for the preparation and characterization of samples for neutron scattering experiments by users and staff. Users preparing to come to the NCNR for an experiment can find detailed descriptions of available laboratory equipment and supplies on the NCNR's website at http://www.ncnr.nist.gov/userlab/.

One of the new laboratories is the result of a bioengineering research partnership between the NCNR and five universities, with partial funding from the National Institutes of Health. This Cold Neutrons for Biology and Technology (CNBT) laboratory is equipped with a high volume laminar flow hood designed for working with acids (e.g., for cleaning substrates), a chromatography refrigerator; a large -40 ºC freezer, a temperature controlled, 13 200 rpm microtube centrifuge, as well as standard wet chemistry equipment for preparing biology-related samples for diffraction, reflectometry, and SANS experiments.

Another laboratory is dedicated primarily to sample characterization and includes equipment for dynamic light scattering, infrared spectroscopy, UV-Visible Spectrophotometry, gas chromatography, and an optical microscope with temperature controlled sample stage, camera and attachments for fluorescence measurements. This laboratory also has a rotary evaporator for purifying solvents and a computer-controlled Langmuir-Blodgett (LB) trough (see Fig. 1) for depositing multimolecular layer LB films on solid substrates.

In addition to the above, there are laboratories with specialized equipment for x-ray diffraction, solid-state chemistry, surface and interface science, and general solution chemistry. Also implemented this year is a bar coding system for maintaining an accurate chemical inventory for all the laboratories. Users can now quickly obtain Materials Safety Data Sheets and determine the availability, location, and quantity of chemicals kept in any laboratory.

FIGURE 1: Yamali Hernandez keeps a watchful eye on the Langmuir-Blodgett trough in one of the NCNR's recently renovated user laboratories.

COMMISSIONING OF A DOUBLE FOCUSING TRIPLE-AXIS SPECTROMETER

The first measurements to characterize the performance of the new state-of-the-art thermal neutron triple-axis spectrometer at beam port BT-7 have been carried out and have met expectations. The new instrument features a choice of either a Cu(220) or a PG(002) doubly-focusing monochromator, providing a continuous incident neutron energy range from 5 meV to 500 meV. The 400 cm^2 reflecting area for each monochromator yields as much as an order-of-magnitude gain of neutrons onto the sample compared with other thermal triple-axis spectrometers at the NCNR. The reactor beam and post monochromatic beam elements (collimators, slits, and filters) offer a wide range of choices to optimize the resolution and intensity of the instrument, with estimated fluxes on the sample of approximately 10^8 $n/cm^2/s$.

The sample stage of the instrument includes two coaxial rotary tables, one for sample rotation and one for the independent rotation of magnetic field coils, and a computer-controlled sample goniometer and elevator. Polarized ^3He cells are under construction for the instrument to provide full polarization analysis with both monochromators and any of the standard analyzer crystals.

The BT-7 spectrometer is designed to be used with interchangeable, customized analyzer/detection systems supported on air pads. The first new analyzer system will have a multistrip PG(002) analyzer array that can be used in a horizontally focused mode, or in a flat configuration either with a linear position-sensitive detector or with conventional Söller collimators. All options will be under computer control and can be selected and interchanged by the experimenter without requiring any mechanical changes or user intervention. A separate diffraction detector is provided in front of the analyzer for Bragg peak measurements, and a series of 13 detectors embedded in the shielding behind the analyzer will continuously monitor the neutron flux entering the analyzer system.These detectors can also be used for measurements of the instantaneous correlation function, for example, or with a radial collimator to determine a diffraction pattern over a limited angular range. This analyzer system is at an advanced stage of development and is scheduled to be installed early in 2006. In the interim, a conventional analyzer system has been installed on air pads so that the instrument is now fully operational as a triple-axis

spectrometer, although the full measurement capability and flexibility won't be realized until the new analyzer system is available.

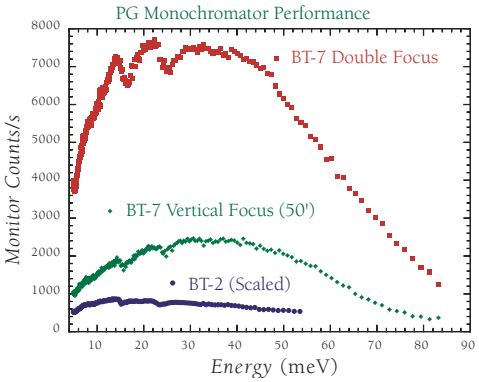

FIGURE 2: Comparison of the beam intensities (monitor count rates) for the PG(002) monochromators for the new BT-7 triple-axis spectrometer and the conventional triple-axis spectrometer at BT-2. The BT-7 monochromator features vertical focusing that varies with energy, whereas the BT-2 monochomator has a fixed vertical focus optimized for 14.7 meV. The collimation was open 50' before and after the monochromator, respectively, on both instruments. The much larger BT-7 monochromator provides more neutrons that fully illuminate the sample over a wider range of incident energies. The new double-focusing mode is seen to provide a dramatic gain in neutron intensity by relaxing the wave vector resolution of the instrument.

INSTALLATION OF THE HIGH INTENSITY MULTI-AXIS COLD NEUTRON SPECTROMETER (MACS) BEGINS

While inelastic neutron scattering can, in principle, elucidate atomic scale dynamics in almost any material, experiments on the most exciting new materials are often impractical because high quality samples are too small. Arguably, this is not a fundamental limitation of the technique but one due to the lack of flux and detection efficiency of current instrumentation. The MACS project aims to increase both factors by an order of magnitude in order to perform informative experiments on 1 mg samples and to obtain comprehensive maps of inelastic scattering when larger samples are available.

FIGURE 3: Designers Peter Hundertmark and Timothy Pike examine the drive mechanism that will rotate the sample and detector around the monochromatic beam transport system.

MACS is a third generation cold neutron spectrometer and, as such, presents many fascinating engineering challenges. In the past year most of these have been overcome and MACS is now in the midst of a busy manufacturing and installation phase. The NCNR's Facility Operation Group has designed, procured, painted, and filled more than 50 metric tons (50 tons) of beamline shielding and beam conditioning optics for MACS.

Figure 3 shows parts of the monochromatic beam transport system for MACS. The shielding penetration consists of an adjustable channel lined by m = 3.5 super mirrors that will guide a converging monochromatic beam to the sample position while minimizing the aperture for fast neutrons and gamma radiation. The ball screw actuation mechanism visible in Fig. 3 will position the super mirror channel, the sample table, and the detector system to receive a monochromatic beam with energies varying from 2.5 meV to 20 meV. Anticipating high-field superconducting magnet systems, all materials within 750 mm of the sample position are nonmagnetic.

FIGURE 4: Stephen Smee (left) and Gregg Scharffstein with the MACS monochromating system. Not shown are Joe Orndorff and Randy Hammond who complete the team from the Instrument Development Group at Johns Hopkins University that designed and assembled the system.

Apart from the intense NCNR cold neutron source, the key to enhancing flux on sample is the monochromating system, which will focus the beam from 1400 cm^2 to 8 cm^2. It consists of a variable beam aperture to minimize background and to control wave vector resolution, a four-position radial collimation system to control energy resolution, and a translating, doubly focusing graphite monochromator. These will inhabit a helium-filled cask to reduce air scattering and pack shielding close to the complex beamline elements. Figure 4 shows these items during tests by the Instrument Development Group at Johns Hopkins University where they were designed and assembled. The monochromating system now stands ready for neutrons at the NCNR.

All the equipment described above was installed in the beamline in the late summer and early fall of 2005. Sample stage and detector system installation will start in the fall so MACS can be ready for commissioning experiments and friendly users in the spring of 2006. While MACS will eventually become a CHRNS user facility for a broad range of science

spanning condensed matter physics, chemistry, and biology, and we are particularly excited about the new capabilities that MACS will provide for research in quantum magnetism and superconductivity.

DATA ANALYSIS, VISUALIZATION, AND MODELING SOFTWARE – DAVE II

Significant development activity in the DAVE (Data Analysis and Visualization Environment) team over the last year has resulted in a brand new look and feel for DAVE. DAVE II brings a new paradigm to data visualization and analysis via a novel datacentric user-interface. The infrastructure includes a project manager, data manager, visualization manager, user-interface, visualization modules, and mechanisms for easy integration of additional applications as they become available. All of this has been designed to help the user get the most from his/her neutron

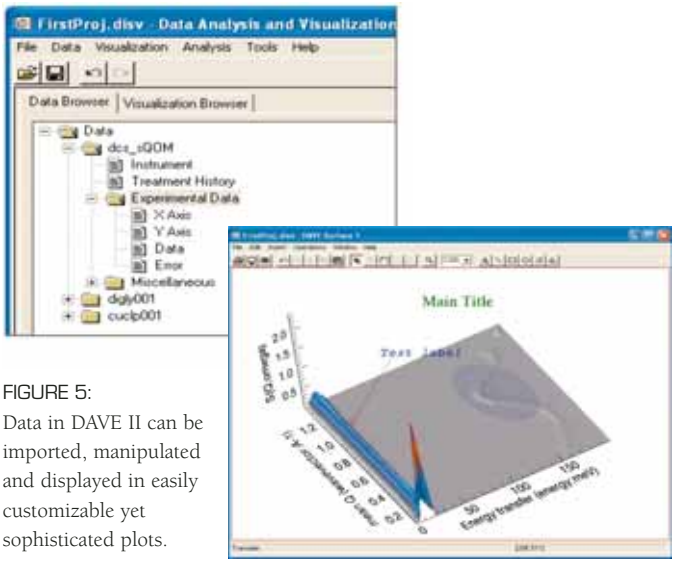

FIGURE 5:
Data in DAVE II can be imported, manipulated and displayed in easily customizable yet sophisticated plots.

data. The project manager concept promises to greatly simplify the user experience because it allows a user to save a complete session (plots, reduction steps, data operations, etc.) and restore it at a later time. Moreover there is much greater flexibility in DAVE II with the implementation of a document/view architecture. Multiple datasets can be loaded simultaneously and multiple views (even of the same dataset) can be created (line, contour, image, surface and volume renderings using OpenGL, the industry standard for high performance graphics). The visualizations are feature-rich allowing simple creation of sophisticated plots resulting in publication-quality output. Undo/redo functionality is implemented allowing scientists to perform "what-if" types of analyses with ease, thus enhancing the user experience. In the initial release, support for ASCII and the current DAVE format are provided. Operations to perform specific data analysis tasks are being implemented and the initial data reduction functionality is identical to that of the current version of DAVE.

FIGURE 6: Jeff Ziegler installs one of his Preamplifier-Amplifier-Discriminator modules in the High Flux Backscattering Spectrometer.

DEPLOYMENT OF ELECTRONICS FOR LARGE DETECTOR ARRAYS

As the number of detectors on an instrument increases and the detectors themselves are buried in locations that are not readily accessible, the task of tuning the discriminator thresholds and periodically inspecting the banks for quality control becomes a major undertaking. The Preamplifier-Amplifier-Discriminator 2 (PAD2) system (Fig. 6), developed by the NCNR's data acquisition and instrument control team, is a state-of-the-art solution to the needs of instruments with a large number of detectors. This system consists of compact front-end modules combining the functions of preamplifier, amplifier, and discriminator, concentrator boards that multiplex control and data signals for eight front-end units, and a system controller that can set the gain and signal threshholds for a collection of up to 2048 individual detectors. The differential signal levels employed allow for longer cable runs and greatly improved noise rejection over the existing TTL solutions. Live quality control is now possible thanks to *in situ* pulse height analysis. A single point of control makes it possible to tune the discriminator settings for detectors behind shielding or *in vacuo*. Taken in combination, the capabilities of this new system are groundbreaking and surpass anything available commercially. The system was successfully deployed on the 32-detector BT-1 powder diffractometer and the HFBS backscattering spectrometer in 2005.

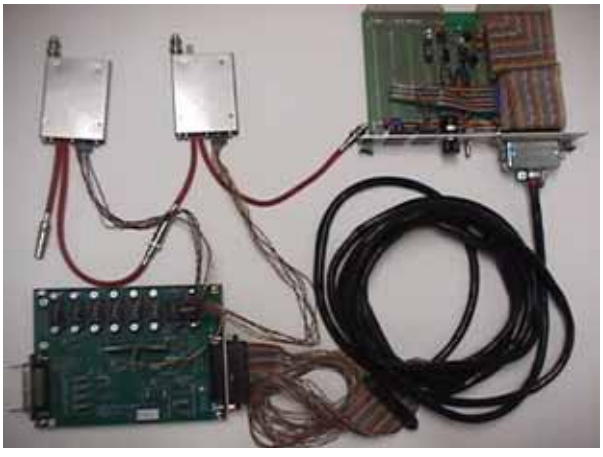

FIGURE 7: Preamplifier-Amplifier-Discriminator 2 (PAD2) system components.

Awards in 2005

ACA GRANTS 2006 WARREN AWARD TO CHARLES MAJKRZAK

The American Crystallographic Association presented the 2006 Bertram E. Warren Award to Dr. Charles F. Majkrzak of the NCNR. Dr. Majkrzak is cited for his seminal contributions to the development of neutron reflectivity and for his pioneering work in the exploration of many issues in interface science using this technique.

Of particular note is how Dr. Majkrzak designed, optimized, and made creative use of supermirror polarizers, integrating them into neutron instruments that attain very low backgrounds and consequently the highest signal-to-noise ratios achieved anywhere. Moreover, Dr. Majkrzak and his collaborators developed an exact, first-principles method to analyze specular reflectivity data. The culmination of their efforts was a solution to the phase problem for neutron reflectivity that allowed the direct inversion of the reflection amplitude to obtain the scattering length density profile uniquely within the dynamical theory of diffraction. This method involves the use of a layer, a substrate, or fronting material that can be used as a reference, and is of immense importance for neutron reflectivity studies of unknown structures.

TANER YILDIRIM WINS NIST BRONZE MEDAL

NIST has recognized the work of Dr. Taner Yildirim, physicist at the NCNR, with a Bronze Medal award. Dr. Yildirim's theoretical research has led to a new understanding of how the physical and chemical properties of carbon nanotubes can be controlled with pressure. He predicted that networks of covalently interlinked nanotubes would form under pressure, a finding with clear implications for the strength of nanocomposites that was later confirmed experimentally. He showed that compressing an insulating nanotube allows the reversible tuning of the band gap, a critical property in nanoscale electronic devices, and could also be used to tune the chemical reactivity at specific sites on the nanotubes, allowing attachment of selected atoms to those sites. This latter prediction holds promise for controlled nanochemistry and chemical filtering.

NIST SILVER MEDALS GO TO SUSAN KRUEGER, JOSEPH DURA, CHARLES MAJKRZAK AND DONALD PIERCE

NIST has recognized the work of Susan Krueger, Joseph Dura and Charles Majkrzak-physicists, and Donald Pierce-mechanical engineer all of the NIST Center for Neutron Research with Silver Medal awards. Drs. Krueger, Dura, Majkrzak and Mr. Pierce are recognized for their outstanding scientific and engineering leadership in establishing, at the NCNR, the Cold Neutrons for Biology and Technology (CNBT), a partnership between NIST, the National Institutes of Health, and six major U.S. universities. This team and their partners conceived, developed, and implemented new world-class neutron diffraction and reflection instrumentation, and a new approach for structural biology research that provides the United States with totally new capabilities for future studies of key biological systems.

RABINOW AWARD MADE TO PAUL BRAND, RICHARD FIELDS AND HENRY PRASK

Drs. Paul C. Brand (NCNR), Richard J. Fields (Metallurgy, MSEL) and Henry J. Prask (NCNR) were awarded the Jacob Rabinow Applied Research Award by NIST. Over the last decade, Drs. Brand, Fields, and Prask have developed the nation's best capabilities for measuring residual stress depth profiles and texture in metals, ceramics, and composites. They forged applied research collaborations with a dozen U.S. industrial organizations, the Army and Navy, the Departments of Transportation and Energy, and 10 major universities. Their work has had a major impact on automobile spring production, sheet-metal forming, welding and machining technology as well as advanced thermal barrier coatings. Their measurement of residual stress in railroad rails improved the transportation infrastructure and has facilitated major advances in the modeling of mechanical properties of materials.

BRIAN TOBY ELECTED FELLOW OF THE INTERNATIONAL CENTRE FOR DIFFRACTION DATA (ICDD)

In a letter dated 30 September 2004, The Board of Directors of the ICDD elected Dr. Brian H. Toby, team leader in crystallography at the NCNR, to the rank of Fellow for his outstanding contributions to the work of the Centre over many years.

"The designation of Fellow of the ICDD may be given by the Awards Committee to those members of the ICDD who have given of their time and talents, beyond that normally associated with regular membership."

FRANK BATES PRESENTED TURNBULL LECTURE AWARD

Dr. Frank Bates, Distinguished McKnight University Professor and Head of Chemical Engineering and Materials Science at the University of Minnesota, was presented the Turnbull Lecturer Award at the 2004 MRS Fall Meeting in Boston. The Award recognizes the career of a scientist who has made outstanding contributions to understanding materials phenomena and properties through research, writing, and lecturing, as exemplified by David Turnbull.

"For pioneering contributions to the fundamental understanding of structure and properties of complex polymeric materials, particularly block copolymers and polymeric vesicles, coupled with outstanding lecturing, writing, teaching, and educational leadership."

Professor Bates has been a frequent visitor to the NCNR using neutrons to study polymer structure on the NG-7, 30 m SANS instrument that is funded by a Participating Research Team that includes the University of Minnesota. He was awarded the 1997 Polymer Physics Prize by the American Physical Society and was elected to the US National Academy of Engineering in 2002.

VANESSA PETERSON WINS AMERICAN CERAMIC SOCIETY BRUNAUER AWARD

The Cements Division of the American Ceramic Society granted the 2005 Brunauer Award to Dr. Vanessa Peterson of the NCNR for the best paper on the topic of cements published by the American Ceramic Society during the previous year.

The paper cited: V. K. Peterson, B. Hunter, and A. Ray, "*Tricalcium silicate T1 and T2 polymorphic investigations: Rietveld refinement at various temperatures using synchrotron powder diffraction*", J. Am. Ceram. Soc. 87 [9], 1625-1634 (2004).

THOMAS RUSSELL AWARDED 2005 POLYMER PHYSICS PRIZE

Dr. Thomas Russell, Distinguished Professor of the Polymer Science & Engineering Department of the University of Massachussetts Amherst and a frequent user of facilities at the NCNR was awarded the 2005 Polymer Physics Prize…

"for his pioneering research and fundamental elucidation of the surface and interfacial behavior of polymers".

The prize consists of $10 000 and a certificate citing the contributions made by the recipient. It was presented to Professor Russell at the American Physical Society March 2005 meeting in Los Angeles, CA.

Professor Russell is Director of the Materials Research Science and Engineering Center on Polymers, Associate Director of MassNanoTech, and is an Associate Editor of Macromolecules. He is a fellow of the American Physical Society and the American Association for the Advancement of Science. In 2004 he was elected Distinguished Professor, and was given the Dutch Polymer Award.

Publications

Abdurashitov, J. N., Gavrin, V. N., Girin, S. V., Gorbachev, V. V., Gurkina, P. P., Ibragimova, T. V., Kalikhov, V. A., Khairnasov, N. G., Knodel, T. V., Matveev, V. A., Mirmov, I. N., Shikhim, A. A., Verentenkin, E. P., Vermul, V. M., Yants, V. E., Zatsepin, G. T., Bowles, T. J., Elliot, T. J., Teasdale, J. W. A., Nico, J. S., Cleveland, B. T., Haxton, W. C., Wilkerson, J. F., Suzuki, A., Lande, K., Khomyakov, Y.-S., Poplavsky, V. M., Popov, V. V., Mishin, O. V., Petrov, A. N., Vasiliev, B. A., Voronov, S. A., Karpenko, A. I., Maltsev, V. V., Oshkanov, N. N., Tuchkov, A. M., Barsanov, V. I., Janelidze, A. A., Korenkova, A. V., Kotelnikov, N. A., Markov, S.-Y., Slein, V. V., Shakirov, Z. N., Zayatina, A. A., Zlokazov, S. B., "Present Status of the SAGE ^{37}Ar Neutrino Source Experiment," *Proceedings of the XI International Workshop on Neutrino Telescopes,* edited by Baldo-Ceolin, M., (February, 2005, Venice, Italy) p. 76 (2005).

Adams, C. P., Lynn, J. W., Smolyaninova, V. N., Biswas, A., Greene, R. L., Ratcliff, W., Cheong, S.-W., Mukovskii, Y. M., Shulyatev, D. A., "First-Order Nature of the Ferromagnetic Phase Transition in (La-Ca)MnO_3 Near Optimal Doping," Phys. Rev. B **70**, 134414 (2004).

Aharony, A., Entin-Wohlman, O., Korenblit, I. Y., Harris, A. B., Yildirim, T., "The Cubic Kugel-Khomskii Model for Triply Degenerate t_{2g} Electrons," New J. Phys. **7**, 49 (2005).

Akcora, P., Zhang, X., Varughese, B., Briber, R. M., Kofinas, P., "Structural and Magnetic Characterization of Norbornene-Deuterated Norbornene Dicarboxylic Acid Diblock Copolymers Doped With Iron Oxide Nanoparticles," Polymer **46** (14), 5194 (2005).

Aldrige, L. P., Bordallo, H. N., Desmedt, A., "Water Dynamics in Cement Pastes," Physica B **359**, E565 (2004).

Alinger, M. J., Odette, G. R., Hoelzer, D. T., "The Development and Stability of Y-Ti-O Nanoclusters in Mechanically Alloyed Fe-Cr Based Ferritic Alloys," J. Nucl. Mater. **329-333**, 382 (2004).

Allen, A. J., "Characterization of Ceramics by X-Ray and Neutron Small-Angle Scattering," J. Am. Ceram. Soc. **88** (6), 1367 (2005).

Allen, A. J., McLaughlin, J. C., Neumann, D. A., Livingston, R. A., "*In Situ* Quasielastic Scattering Characterization of Particle Size Effects on the Hydration of Tricalcium Silicate," J. Mater. Res. **19**, 3242 (2004).

Alvarez, E., Lindstrom, R. M., Paul, R. L., Cook, J., Schröder, I. G., "Redesign of the Cold-Neutron Analytical Chemistry Instruments at the NIST Center for Neutron Research," *Transactions of the American Nuclear Society* **91**, 823 (2004).

Anderson, D. L., Cunningham, W. C., "Analysis of Total Diet Study Foods for Gamma-Ray Emitting Radionuclides," J. Radioanal. Nucl. Chem. Lett. **264** (2), 371 (2005).

Anderson, D. L., Kastovszky, Z. S., "Applications of PGAA with Beams," Chapter 6, in *Handbook of Prompt Gamma Activation Analysis with Neutron Beams*, edited by Molnár, G. L. (Kluwer Academic Publishers, Netherlands), p. 137 (2004).

Anderson, D. L., Mackey, E. A., "Improvements in Food Analysis by Thermal Capture Prompt Gamma-Ray Spectrometry," J. Radioanal. Nucl. Chem. Lett. **263** (3), 683 (2005).

Argyriou, D. N., Ruett, U., Adams, C. P., Lynn, J. W., Mitchell, J. F., "Phase Separation Without Quenched Disorder in $Pr_{0.7}Ca_{0.3}MnO_3$," New J. Phys. **6**, 195 (2004).

Atienza, J. M., Martinez-Perez, M. L., Hervias, J. R., Pompean, F., Garcia-Hernandez, M., Elices, M., "Residual Stresses in Cold Drawn Ferritic Rods," Scripta Mater. **52** (4), 305 (2005).

Baglioni, P., Fratini, E., Lonetti, B., Chen, S.-H., "Structural Arrest in Concentrated Cytochrome C Solutions: the Effect of pH and Salts," J. Phys.: Condens. Matter **16** (42), S5003 (2004).

Bailey, M., Shen, D. Y., McGuire, M. A., Toby, B. H., DiSalvo, F. J., Yamane, H., Sasaki, S., Shimada, M., "The New Indium Sub-Nitrides, $Ae_6In_4(In_xLi_y)N_{3-z}$ (Ae=Sr and Ba)," Inorg. Chem., in press.

Balzar, D., Audenbrand, N., Daymond, M. R., Fitch, A., Hewat, A., Langford, J. I., LeBail, A., Louër, D., Masson, O., McCowan, C. N., Popa, N. C., Stephens, P. W., Toby, B. H., "Size-Strain Line-Broadening Analysis of the Ceria Round-Robin Sample," J. Appl. Crystallogr. **37**, 911 (2004).

Bandyopadhyay, R., Liang, D., Yardimci, H., Sessoms, D. A., Borthwick, M. A., Mochrie, S. G. J., Harden, J. L., Leheny, R. L., "Evolution of Particle-Scale Dynamics in an Aging Clay Suspension," Phys. Rev. Lett. **93**, 228302 (2004).

Bass, C. D., Dawkins, J. M., Luo, D., Micherdzinska, A., Sarsour, M., Snow, W. M., Mumm, H. P., Nico, J. S., Huffman, P. R., Markoff, D. M., Heckel, B. R., Swanson, H. E., "Measurement of the Parity-Violating Neutron Spin Rotation in ^{4}He," J. Res. Natl. Inst. Stand. Technol. **110**, 205 (2005).

Bauer, B. J., "Transformation of Phase Size-Distribution into Scattering Intensity," J. Polym. Sci., Part B: Polym. Phys. **42** (17), 3070 (2004).

Bennett, A., Daivis, P. J., Shanks, R., Knott, R., "Concentration Dependence of Static and Hydrodynamic Screening Lengths for Three Different Polymers in a Variety of Solvents," Polymer **45**, 8531 (2004).

Bhatia, S. R., "Ultra-Small-Angle Scattering Studies of Complex Fluids," Curr. Opin. Colloid Interface Sci. **9**, 404 (2005).

Bishop, R. L., Sears, E. L., Blackman, M. J., "A Través del Río del Cambio," in *Estudios de Cultura Maya, Mexico. Conf.* Proc., in press.

Boukari, H., Chernomordik, V., Krueger, S., Nossal, R., Sackett, D. L., "Small-Angle Neutron Scattering Studies of Tubilin Ring Polymer," Physica B **350**, E533 (2004).

Broholm, C., Aeppli, G., "Dynamic Correlations in Quantum Magnets," Chapter 2, in *Strong Interactions in Low Dimensions (Physics and Chemistry of Materials With Low Dimensional Structures)*, edited by Baeriswyl, D., Degiorgi, L. (Kluwer Academic Publishers), p. 21 (2004).

Bu, Z., Wang, L., Kendall, D. A., "Nucleotide Binding Induces Changes in the Oligomeric State and Conformation of Sec A in a Lipid Environment: A Small-Angle Neutron Scattering Study," J. Mol. Biol. **332**, 23 (2003).

Burgess, I., Li, M., Horswell, S. L., Szymanski, G., Lipkowski, J., Satija, S., Majewski, J., "Influence of the Electric Field on a Bio-Mimetic Film Supported on a Gold Electrode," Colloids Surf., B **40** (3-4), 117 (2005).

Butch, N. P., Yuhasz, W. M., Ho, P.-C., Jeffries, J. R., Frederick, N. A., Sayles, T. A., Zheng, X. G., Maple, M. B., Betts, J. B., Lacerda, A. H., Woodward, F. M., Lynn, J. W., Rogl, P., Giester, G., "Ordered Magnetic States in $PrFe_4Sb_{12}$ Single Crystals," Phys. Rev. B **71**, 214417 (2005).

Cappelletti, R. L., "MSEL Center for Neutron Research FY2004 Programs and Accomplishments," NISTIR 7128 (2004).

Cappelletti, R. L., "NCNR 2004 NIST Center for Neutron Research Accomplishments and Opportunities," NIST SP1029 (2004).

Chari, K., Seo, Y.–S., Satija, S., "Competitive Adsorption at the Air-Water Interface from a Self-Assembling Polymer-Surfactant Mixture," J. Phys. Chem. B **108** (31), 11442 (2004).

Chen, C., Neelakanta, A., Sakai, V. G., Maranas, J. K., "On the Assessment of Interchain Packing Distances in Polymer Melts Using Neutron Diffraction," Macromol., in press.

Chen, S. H., Su, A. C., Chang, C. S., Chen, H. L., Ho, D. L., Tsao, C. S., Peng, K. Y., Chen, S. A., "Aging of Poly(2-Methoxy-5-(2'-ethylhexy-loxy)-1,4-phenylenevinylene)/Toluene Solutions and Subsequent Effects on Luminescence Behavior of Cast Films," Langmuir **20** (20), 8909 (2004).

Chen, W. C., Gentile, T. R., O' Donovan, K. V., Borchers, J. A., Majkrzak, C. F., "Polarized Neutron Reflectometry of a Patterned Magnetic Film with a ^{3}He Analyzer and a Position-Sensitive Detector," Rev. Sci. Instrum. **75** (10), 3256 (2004).

Chen, W.-R., Liu, Y., Mallamace, F., Thiyagarajan, P., Chen, S.-H., "Studies of Structural Arrest Transition in L64/D_2O Micellar Solutions," J. Phys.: Condens. Matter **16**, S4951 (2004).

Chen, W.-R., Mallamace, F., Glinka, C. J., Fratini, E., Chen, S.-H., "Neutron-and Light-Scattering Studies of the Liquid-to-Glass and Glass-to-Glass Transitions in Dense Copolymer Micellar Solutions," Phys. Rev. E **68**, 041402 (2003).

Chinchilla, O., Bishop, R. L., Blackman, M. J., Sears, E. L., Vicente, J. V., Moraga, R., "Intercambio de Cerámica a Larga Distancia en Cotzumalquapa: Resultados del Análisis por Activación de Neutrones," *XVIII Simposio de Investigaciones Arqueológicas en Guatemala*, edited by Laporte, J. P., Arroyo, B., Mejía, H. E. (Museo Nacional de Arqueología y Etnología: Ministerio de Cultura y Deportes, Instituto de Antropología e Historia, Asociación Tikal, Foundation for the Advancement of Mesoamerican Studies, Inc.), p. 1027 (2005).

Choi, H. D., Firestone, R. B., Lindstrom, R. M., Molnar, G. L., Reddy, A. V. R., Tan, V. H., Zhou, C. M., Paviottia-Corcuera, R. A., Trkov, A., "Development of a Database for Prompt Gamma-Ray Neutron Activation Analysis," J. Nucl. Sci. Technol. **2** (2), 1372 (2005).

Chung, J.-H., Proffen, T., Shamoto, S., Ghorayeb, A. M., Croquennec, L., Tian, W., Sales, B. C., Jin, R., Mandrous, D., Egami, T., "Local Structure of $LiNiO_2$ Studied by Neutron Diffraction," Phys. Rev. B **71** (6), 064410 (2005).

Cicerone, M. T., Soles, C. T., Chowdhuri, Z., Pikal, M. J., Chang, J., "Fast Dynamics as a Diagnostic for Excipients in Preservation of Dried Proteins," Am. Pharm. Rev., in press.

Ciezak, J. A., Trevino, S. F., "The Inelastic Neutron Scattering Spectra of *a*-3-Amino-5,1,2,4-2H-Triazole: Experiment and DFT Calculations," Chem. Phys. Lett. **403** (4-6), 329 (2005).

Ciezak, J. A., Trevino, S. F., "The Molecular Structure and Inelastic Neutron Scattering Spectra of 2,6-Diamino-3,5-Dinitropyrazine," J. Mol. Struct.: Theochem **723**, 241 (2005).

Cipriano, B. H., Raghavan, S. R., McGuiggan, P. M., "Surface Tension and Contact Angle Measurements of a Hexadecyl Imidazolium Surfactant Absorbed on a Clay Surface," Colloids Surf., A, in press.

Ciraci, S., Dag, S., Yildirim, T., Gülseren, O., Senger, R. T., "Functionalized Carbon Nanotubes and Device Application," J. Phys.: Condens. Matter **16**, R901 (2004).

Cochran, E. W., Bates, F. S., "Shear-Induced Network-to-Network Transition in a Block Copolymer Melt," Phys. Rev. Lett. **93** (8), 087802 (2004).

Cook, J. C., Glinka, C. J., Schröder, I. G., "Performance of the Vertical Optical Filter for the NG-3 30 m SANS Instrument at the National Institute of Standards and Technology's Center for Neutron Research," Rev. Sci. Instrum. **76**, 025108 (2005).

Copley, J. R. D., "The Disk Chopper Spectrometer at NIST: The Good, The Bad and The Ugly," *Proceedings of the 17th Meeting of the International Collaboration on Advanced Neutron Sources*, in press.

Cornelius, A. L., Light, B. E., Kumar, R. S., Eichenfield, M., Dutton, T., Pepin, R., Gardner, J. S., "Disturbing the Spin Liquid State in $Tb_2Ti_2O_7$: Heat Capacity Measurements on Rare Earth Titanates," Physica B **359-361**, 1243 (2005).

Cox, D. E., Noheda, B., Shirane, G., "Low-Temperature Phases in $PbZr_{0.52}Ti_{0.48}O_3$: A Neutron Powder Diffraction Study," Phys. Rev. B **71**, 134110 (2005).

Crawford, M. K., Harlow, R. L., Deemyad, S., Tissen, V., Schilling, J. S., McCarron, E. M., Tozer, S. W., Cox, D. E., Ichikawa, N., Uchida, S., Huang, Q., "High Pressure Study of Structural Phase Transitions and Superconductivity in $La_{1.48}Nd_{0.4}Sr_{0.12}CuO_4$," Phys. Rev. B **71**, 104513 (2005).

Crawford, M. K., Harlow, R. L., Lee, P. L., Zhang, Y., Hormadaly, J., Flippen, R., Huang, Q., Lynn, J. W., Stevens, R., Woodfield, B. F., Boerio-Goates, J., Fisher, R. A., "Coupled Magnetic and Structural Transitions in the Frustrated Spin-3/2 Antiferromagnetic $GeCo_2O_4$," Phys. Rev. B, in press.

Curtis, J. E., Tarek, M., Tobias, D. J., "Methyl Group Dynamics as a Probe of the Protein Dynamical Transition," J. Am. Chem. Soc. **126** (49), 15928 (2004).

Dai, P., Kang, H. J., Mook, H. A., Matsuura, M., Lynn, J. W., Kurita, Y., Komiya, S., Ando, Y., "Electronic Inhomogeneity and Competing Phases in Electron-Doped Superconducting $Pr_{0.88}LaCe_{0.12}CuO_{4-\delta}$," Phys. Rev. B **71** (10), 100502 (2005).

DeSanto, P., Buttrey, D. J., Grasselli, R. K., Lugmair, C. G., Volpe, A. F., Toby, B. H., Vogt, T., "Structural Characterization of the Orthorhombic Phase M1 in MoVNbTeO Propane Ammoxidation Catalyst," Top. Catal. 23 (1-4), **23** (2003).

Deshpande, S., Kulkarni, A., Sampath, S., Herman, H., "Application of Image Analysis for Characterization of Porosity in Thermal Spray Coatings and Correlation with Small Angle Neutron Scattering," Surf. Coat. Technol. **187** (1), 6 (2004).

Dewey, M. S., Gilliam, D. M., Nico, J. S., Wietfeldt, F. E., Fei, X., Snow, W. M., Greene, G. L., Pauwels, J., Eykens, R., Lamberty, A., Van Gestel, J., "Measurement of the Neutron Lifetime Using a Proton Trap," Phys. Rev. Lett. **91** (15), 152301 (2003).

Diallo, S. O., Pearce, J. V., Azuah, R. T., Glyde, H. R., "Quantum Momentum Distribution and Kinetic Energy in Solid ^{4}He," Phys. Rev. Lett. **93** (7), 075301 (2004).

Ding, L., Liu, W., Wang, W., Glinka, C. J., Worcester, D. L., Yang, L., Huang, H. W., "Diffraction Techniques for Non-Lamellar Phases of Phospholipids," Langmuir **20** (21), 9262 (2004).

Doucet, M., Maliszewskyj, N., Pheiffer, S., "New Instrumentation Control Software at the NCNR," *Proceedings of the 17th Meeting of the International Collaboration on Advanced Neturon Sources*, in press.

Dumesnil, K., Dufour, C., Mangin, P., Fitzsimmons, M. R., Park, S., Rhyne, J. J., Rogalev, A., Borchers, J. A., "Magnetization Reversal in a YFe_2-Dominant $DyFe_2/YFe_2$ Exchange-Coupled Superlattice: An X-Ray Magnetic Circular Dichroism and Polarized Neutron Reflectometry Study," J. Appl. Phys. **97**, 10K108 (2005).

Dyck, M., Krüger, P., Lösche, M., "Headgroup Organization and Hydration of Methylated Phosphatidylethanomines in Langmuir Monolayers," Phys. Chem. Chem. Phys. **7**, 150 (2005).

Eastwood, E., Viswanathan, S., O'Brien, C. P., Kumar, D., Dadmun, M. D., "Methods to Improve the Properties of Polymer Mixtures: Optimizing Intermolecular Interactions and Compatibilization," Polymer **46**, 3957 (2005).

Egres, R. G., Wagner, N. J., "The Rheology and Microstructure of Acicular Precipitated Calcium Carbonate Colloidal Suspensions Through the Shear Thickening Transition," J. Rheo. **49** (3), 719 (2005).

Esker, A. R., Grüll, H., Satija, S. K., Han, C. C., "Polymer Dynamics in Hydrogenous Systems by Neutron Reflectivity," J. Polym. Sci., Part B: Polym. Phys. **42** (17), 3248 (2004).

Faraone, A., Liu, L., Mou, C.-Y., Yen, C.-W., Chen, S.-H., "Fragile-to-Strong Liquid Transition in Deeply Supercooled Confined Water," J. Chem. Phys. **121**, 10843 (2004).

Fedeyko, J. M., Rimer, J. D., Lobo, R. F., Vlachos, D. G., "Spontaneous Formation of Silica Nanoparticles in Basic Solutions of Small Tetraalkylammonium Cations," J. Phys. Chem. B **108** (33), 12271 (2004).

Fedeyko, J. M., Vlachos, D. G., Lobo, R. F., "Formation and Structure of Self- Assembled Silica Nanoparticles in Basic Solutions of Organic and Inorganic Cations," Langmuir **21** (11), 5197 (2005).

FitzGerald, P. A., Davey, T. W., Warr, G. G., "Micellar Structure in Gemini Nonionic Surfactants from Small-Angle Neutron Scattering," Langmuir **21**, 7121 (2005).

Gallagher, P. D., Satija, S. K., Karim, A., Douglas, J. F., Fetters, L. J., "Swelling of a Polymer Brush by a Poor Solvent," J. Polym. Sci., Part B: Polym. Phys. **42** (22), 4126 (2004).

Garcia-Sakai, V., Chen, C., Maranas, J. K., Chowdhuri, Z., "Effect of Blending with Poly (Ethylene Oxide) on the Dynamics of Poly (Methyl Methacrylate): A Quasielastic Neutron Scattering Approach," Macromol. **37**, 9975 (2004).

Garcia-Sakai, V., Maranas, J. K., Chowdhuri, Z., Peral, I., Copley, J. R. D., "Miscible Blend Dynamics and the Length Scale of Local Compositions," J. Polym. Sci., Part B: Polym. Phys., in press.

Gardner, J. S., Ehlers, G., Rosov, N., Erwin, R. W., Petrovic, C., "Spin-Spin Correlations in $Yb_2Ti_2O_7$: A Polarized Neutron Scattering Study," Phys. Rev. B **70** (10), 180404 (2004).

Gardner, J. S., Keren, A., Ehlers, G., Stock, C., Segal, E., Roper, J. M., Fak, B., Stone, M. B., Hammar, P. R., Reich, D. H., Gaulin, B. D., "Dynamic Frustrated Magnetism in $Tb_2Ti_2O_7$ at 50 mK," Phys. Rev. B **68**, 180401 (2003).

Garvey, C. J., Parker, I. H., Knott, R. B., Simon, G. P., "Small Angle Scattering in the Porod Region from Hydrated Paper Sheets at Varying Humidities," Holzforschung **58** (5), 473 (2004).

Gaulin, B. D., Gardner, J. S., "Experimental Studies of Frustrated Pyrochlore Antiferromagnets," Chapter 8, in *Magnetic Frustrated Spin Systems*, edited by Diep, H. T. (World Scientific), p. 457 (2005).

Gaulin, B. D., Lee, S.-H., Haravifard, S., Castellan, J. P., Berlinsky, A. J., Dabkowska, H. A., Qiu, Y., Copley, J. R. D., "High Resolution Study of Spin Excitations in the Singlet Ground State of $SrCu_2(BO_3)_2$," Phys. Rev. Lett. **93** (26), 267202 (2004).

Gehring, P. M., Chen, W., Ye, Z.-G., Shirane, G., "The Non-Rhombohedral Low-Temperature Structure of PMN-10%PT," J. Phys.: Condens. Matter **16**, 7113 (2004).

Gehring, P. M., Copley, J. R. D., "NCNR Holds Eleventh Annual Summer School on Neutron Scattering," Neutron News, in press.

Geissler, E., Hecht, A. M., Horkay, F., Basser, P. J., "Light Small Angle Neutron and X-Ray Scattering from Gels," Macromol. Symp. **227** (1), 27 (2005).

Gentile, T. R., Babcock, E., Borchers, J. A., Chen, W. C., Hussey, D., Jones, G. L., Lee, W. T., Majkrzak, C. F., O'Donovan, K. V., Snow, W. M., Tong, X., te Velthius, S. G. E., Walker, T. G., Yan, H., "Polarized ^{3}He Spin Filters in Neutron Scattering," Physica B **356** (1-4), 96 (2005).

Gentile, T. R., Chen, W. C., Jones, G. L., Babcock, E., Walker, T. G., "Polarized ^{3}He Spin Filters for Slow Neutron Physics," J. Res. Natl. Inst. Stand. Technol. **110**, 299 (2005).

George, M., Snyder, S. L., Terech, P., Weiss, R. G., "Gelation of Perfluorinated Liquids by N-Alkyl Perflouroalkanamides," Langmuir, in press.

Gerber, M. J., Kline, S. R., Walker, L. M., "Characterization of Rod-Like Aggregates Generated from a Cationic Surfactant and a Polymerizable Counterion," Langmuir **20** (20), 8510 (2004).

Gericke, M. T., Bowman, J. D., Carlini, R. D., Chupp, T. E., Coulter, K. P., Dabaghyan, M., Desai, D., Freedman, S. J., Gentile, T. R., Gillis, R. C., Greene, G. L., Hersman, F. W., Ino, T., Ishimoto, S., Jones, G. L., Lauss, B., Leuschner, M., Losowski, B., Haurin, R., Masuda, Y., Mitchell, G. S., Nann, H., Muto, S., Page, S. A., Penttilä, S. I., Ramsay, W. D., Santra, S., Seo, P.-N., Sharapov, E. I., Smith, T. B., Snow, W. M., Wilburn, W. S., Yuan, V., Zhu, H., "Commissioning the NPDGamma Detector Array: Counting Statistics in Current Mode Operation and Parity Violation in the Capture of Cold Neutrons on B_4C and ^{27}Al," J. Res. Natl. Inst. Stand. Technol. **110**, 215 (2005).

Gibson, W. M., Schultz, A. J., Richardson J. W., Carpenter, J. M., Mildner, D. F. R., Chen-Mayer, H. H., Miller, M. E., Maxey, E. R., Youngman, R., "Convergent Beam Neutron Crystallography," J. Appl. Crystallogr. **37**, 778 (2004).

Gilliam, S. B., Gidcumb, S. M., Parikh, N. R., Patnaik, B. K., Hunn, J. D., Snead, L. L., Lamaze, G. P., "A Study of Helium Retention and Surface Blistering Characteristics of Tungsten with Regard to First Wall Conditions in an Inertial Fusion Energy Reactor," J. Nucl. Mater., in press.

Glade, S. C., Wirth, B. D., Odette, G. R., Asoka-Kumar, P. Sterne, P. A., Howell, R. H., "Positron Annihilation Spectroscopy and Small-Angle Neutron Scattering Characterization of the Effect of Mn on the Nanostructural Features Formed in Irradiated Fe-Cu-Mn alloys," Phil. Mag. **85** (4-7), 629 (2005).

Gnäupel-Herold, T., Foecke, T., Prask, H. J., Fields, R. J., "An Investigation of Springback Stresses in an AISI-1010 Deep Drawn Cup," Mater. Sci. Eng., A **399**, 26 (2005).

Gonzalez, Y. I., Nakanishi, H., Stjerndahl, M., Kaler, E. W., "Influence of pH on the Micelle-to-Vesicle Transition in Aqueous Mixtures of Sodium Dodecyl Benzenesulfonate with Histidine," J. Phys. Chem B **109**, 11675 (2005).

Gonzalez, Y. I., Stjerndahl, M., Danino, D., Kaler, E. W., "Spontaneous Vesicle Formation and Phase Behavior in Mixtures of an Anionic Surfactant with Imidazoline Compounds," Langmuir **20**, 7053 (2004).

Goremychkin, E. A., Osborn, R., Bauer, E. D., Maple, M. B., Frederick, N. A., Yuhasz, W. M., Woodward, F. M., Lynn, J. W., "Crystal Field Potential of $PrOs_4Sb_{12}$: Consequences for Superconductivity," Phys. Rev. Lett. **93** (15), 157003 (2004).

Granado, E., "Investigating Strongly Correlated Electron Systems with Synchrotron X-Ray Diffraction at LNLS," Physica B **354**, 320 (2004).

Granado, E., Huang, Q. Z., Lynn, J. W., Gopalakrishnan, J., Ramesha, K., "Crystal Structures and Magnetic Order of $La_{0.5+\delta}A_{0.5-\delta}Mn_{0.5+\varepsilon}Ru_{0.5-\varepsilon}O_3$ (A= Ca, Sr, Ba): Possible Orbital Glass Ferromagnetic State," Phys. Rev. B **70** (21), 214416 (2004).

Granado, E., Urbano, R. R., Azimonte, C., Souza, R. A., Souza-Neto, N. M., Ramos, A. Y., Perez, C. A., Lynn, J. W., Barilo, S. N., "Orbital Order in a Spin-Glass Fe-Substituted Manganite," Phys. Rev. B, in press.

Graves, S., Meleson, K., Wilking, J., Lin, M. Y., Mason, T. G., "Structure of Concentrated Nanoemulsions," J. Chem. Phys. **122**, 134703 (2005).

Grohol, D., Matan, K., Cho, J.-H., Lee, S.-H., Lynn, J. W., Nocera, D. G., Lee, Y. S., "Spin Chirality on a Two-Dimensional Frustrated Lattice," Nature Mater. **4** (4), 323 (2005).

Grüll, H., Sung, L., Karim, A., Douglas, J. F., Satija, S. K., Mayashi, M., Jannai, H., Hasimoto, T., Han, C. C., "Finite Size Effects on Surface Segregation in Polymer Blend Films Above and Below the Critical Point of Phase Separation," Euro. Phys. Lett. **65** (5), 671 (2004).

Gu, X., Nguyen, T., Ho, D. L., Oudina, M., Martin, D., Kidah, B., Jamin, J., Rezig, A., Sung, L., Byrd, E., Martin, J. W., "Microstructure and Morphology of Amine-Cured Epoxy Coatings and Their Changes/ with Outdoor Exposures- An AFM Study," J. Coat. Technol. **2** (7), 547 (2005).

Hackley, V. A., Stoimenov, P. K., Ho, D. L., Sung, L. P., Klabunde, K. J., "Structure Development in Aerogel-Processed Nanocrystalline Alkaline-Earth Oxides as Revealed by SANS," J. Appl. Crystallog. **38**, 619 (2005).

Hagiwara, M., Regnault, L. P., Zheludev, A., Stunault A., Metoki, N., Suzuki, T., Suga, S., Kakurai, K., Koike, Y., Vonderwisch, P., Chung, J. H., "Spin Excitations Under Fields in an Anisotropic Bond-Alternating Quantum S=1 Chain: Contrast with Haldane Spin Chains," Phys. Rev. Lett. **94**, 177202 (2005).

Hamilton, W. A., Porcar, L., Magid, L. J., "Using Neutron Relectometry and Reflection Geometry 'Near Surface' at a Solid-Solution Interface," Physica B **357** (1-2), 88 (2005).

Hammouda, B., Ho, D. L., Kline, S., "Insight into Clustering in Poly(Ethylene Oxide) Solutions," Macromol. **37** (18), 6932 (2004).

Hammouda, B., Horkay, F., Becker, M., "Clustering and Solvation in Poly(Acrylic Acid) Polyelectrolyte Solutions," Macromol. **38** (5), 2019 (2005).

Harroun, T. A., Koslowsky, M., Nieh, M.-P., de Lannoy, C.-F., Raghunathan, V. A., Katsaras, J., "Comprehensive Examination of Mesophases Formed by DMPC and DHPC Mixtures," Langmuir **21**, 5356 (2005).

Hauer, B., Hempelman, R., Udovic, T. J., Rush, J. J., Kockmann, W., Jansen, E., Schäfer, W., Richter, D., "Neutron Scattering Studies on the Vibrational Excitations and the Structure of Ordered Niobium Hydrides: The λ Phases," J. Phys. Condens. Matter **16**, 5205 (2004).

Hedden, R. C., Lee, H. J., Soles, C. L., Bauer, B. J., "Characterization of Pore Structure in a Nanoporous Low-Dielectric-Constant Thin Film by Neutron Porosimetry and X-Ray Porosimetry," Langmuir **20** (16), 6658 (2004).

Hiraka, H., Böni, P., Yamada, K., Park, S., Lee. S.-H., Shirane, G., "Characterization of Low-Energy Magnetic Excitations in Chromium," Phys. Rev. B. **70**, 144413 (2004).

Hiraka, H., Lee, S.-H., Gehring, P. M., Xu, G., Shirane, G., "Cold Neutron Study on the Diffuse Scattering and Phonon Excitations in the Relaxor $Pb(Mg_{1/3}Nb_{2/3})O_3$," Phys. Rev. B **70** (18), 184105 (2004).

Ho, D. L., Byrnes, W. M., Ma, W. P., Shi, Y., Callaway, D. J. E., Bu, Z. M., "Structure-Specific DNA-Induced Conformational Changes in *Taq* Polymerase Revealed by Small Angle Neutron Scattering," J. Biol. Chem. **279** (37), 39146 (2004).

Ho, D. L., Glinka, C. J., "New Insights into Hansen's Solubility Parameters," J. Polym. Sci., Part B: Polym. Phys. **42**, 4337 (2004).

Ho, D. L., Hammouda, B., Kline, S. R., "Unusual Phase Behavior in Mixtures of Poly(Ethylene Oxide) and Ethyl Alcohol," J. Polym. Sci., Part B: Polym. Phys., in press.

Hoelzel, M., Danilkin, S., Ehrenberg, H., Toebbens, D., Udovic, T. J., Fuess, H., Wipf, H., "Effects of High-Pressure Hydrogen Charging on the Structure of Austenitic Stainless Steels," Mater. Sci. Eng., A **384** (1-2), 255 (2004).

Hoelzel, M., Rajevac, V., Danilkin, S. A., Udovic, T. J., Wipf, H., Fuess, H., "Lattice Dynamics of High Pressure Hydrogenated Austenitic Stainless Steels," J. Phys.: Condens. Matter **17**, 3537 (2005).

Horkay, F., Basser, P. J., Hecht, A. M., Geissler, E., "Structural Investigation of a Neutralized Polyelectrolyte Gel and an Associating Neutron Hydrogel," Polymer **46** (12), 4242 (2005).

Horkay, F., Basser, P. J., Ho, D. L., Hecht, A. M., Geissler, E., "Calcium Induced Structural Changes in DNA Gels," J. Am. Chem. Soc., in press.

Huang, P. J., Wu, S. Y., Tsao, F. C., Yang, C. C., Chung, M. K., Li, W. H., Lynn, J. W., Ku, H. C., "Mn Ordering in Fully Oxygenated $Lu_{1-x}Sc_xMnO_3$ (x=0, 0.5 and 1)," J. App. Phys. **97**, 10H703 (2005).

Huang, Q., Foo, M. L., Lynn, J. W., Zandbergen, H. W., Lawes, G., Wang, Y., Toby, B. H., Ramirez, A. P., Ong, N. P., Cava, R. J., "Low Temperature Phase Transitions and Crystal Structure of $Na_{0.5}CoO_2$," J. Phys.: Condens. Matter **16**, 5803 (2004).

Huang, Q., Foo, M. L., Pascal, R. A., Lynn, J. W., Toby, B. H., He, T., Zandbergen, H. W., Cava, R. J., "Coupling Between Electronic and Structural Degrees of Freedom in the Triangular Lattice Conductor Na_xCoO_2," Phys. Rev. B **70** (18), 184110 (2004).

Huang, Q., Khaykovich, B., Chou, F. C., Cho, J. H., Lynn, J. W., Lee, Y. S., "Structural Transition in Na_xCoO_2 with *x* Near 0.75 due to Na Rearrangement," Phys. Rev. B **70**, 134115 (2004).

Huang, Q., Lynn, J. W., Toby, B. H., Foo, M.-L., Cava, R. J., "Characterization of the Structural Transition in $Na_{0.75}CoO_2$," J. Phys.: Condens. Matter **17**, 1831 (2005).

Hubbard, F. P., Santonicola, G., Kaler, E. W., Abbott, N. L., "Small-Angle Neutron Scattering from Mixtures of Sodium Dodecyl Sulfate and a Cationic, Bolaform, Surfactant Containing Azobenzene," Langmuir **21** (14), 6131 (2005).

Hücker, M., Kim, Y. J., Gu, G. D., Tranquada, J. M., Gaulin, B. D., Lynn, J. W., "Neutron Scattering Study of $La_{1.9}Ca_{1.1}Cu_2O_{6+\delta}$ and $La_{1.85}Sr_{0.15}CaCu_2O_{6+\delta}$," Phys. Rev. B **71**, 094510 (2005).

Hudson, B. S., Braden, D. A., Allis, D. G., Jenkins, T., Baronov, S., Middleton, C., Withnall, R., Brown, C. M., "The Crystalline Enol of 1, 3-Cyclohexanedione and its Complex with Benzene: Vibrational Spectra, Simulation of Structure and Dynamics and Evidence for Cooperative Hydrogen Bonding," J. Phys. Chem. A **108**, 7356 (2004).

Huffman, P. R., Arif, M., Dewey, M. S., Gentile, T. R., Gilliam, D. M., Jacobson, D. L., Nico, J. S., Thompson, A. K., "The Fundamental Neutron Physics Facilities at NIST," AIP Conf. Proc. **680**, 275 (2003).

Huffman, P. R., Jacobson, D. L., Schoen, K., Arif, M., Black, T. C., Snow, W. M., Werner, S. A. "Precision Neutron Interferometric Measurement of the *n*-^{3}He Coherent Neutron Scattering Length," Phys Rev. C **70**, 014004 (2004).

Hussey, D. S., Jacobson, D. L., Arif, M., Huffman, P. R., Williams, R. E., Cook, J. C., "New Neutron Imaging Facility at the NIST," Nucl. Instrum. Methods Phys. Res., Sect. A **542**, 9 (2005).

Hussey, D. S., Rich, D. R., Belov, A. S., Tong, X., Yang, H., Bailey, C., Keith, C. D., Hartfield, J., Hall, G. D. R., Black, T. C., Snow, W. M., Gentile, T. R., Chen, W. C., Jones, G. L., Wildman, E., "Polarized ^{3}He Gas Compression System Using Metastability- Exchange Optical Pumping," Rev. Sci. Instrum. **76** (5), 053503 (2005).

Idrobo, J. C., Öğüit, S., Yildirim, T., Klie, R., Browning, N., "Electronic and Superconducting Properties of Oxygen Ordered MgB_2 Compounds of the Form $Mg_2B_3O_4$," Phys. Rev. B **70**, 172503 (2004).

Ijiri, Y., Kelly, C. V., Borchers, J. A., Rhyne, J. J., Farrell, D. F., Majetich, S. A., "Detection of Spin Coupling in Iron Nanoparticles with Small Angle Neutron Scattering," App. Phys. Lett. **86**, 243102 (2005).

Ijiri, Y., Kelly, C. V., Borchers, J. A., Rhyne, J. J., Farrell, D. F., Majetich, S. A., "Surface and Size Effects on Small Angle Neutron Scattering of Iron Nanoparticles," Appl. Phys. Lett., in press.

Íñiguez, J., Yildirim, T., "First-Principles Study of Ti-Doped Sodium Alanate Surfaces," App. Phys. Lett. **86**, 103109 (2005).

Íñiguez, J., Yildirim, T., "Unusual Structural Tuning of Magnetism in Cuprate Perovskites," Phys. Rev. B **71**, 180415 (2005).

Íñiguez, J., Yildirim, T., Udovic, T. J., Sulic, M., Jensen, C. M., "Structure and Hydrogen Dynamics of Pure and Ti-Doped Sodium Alanate," Phys. Rev. B **70**, 060101 (2004).

Itakura, T., Bertram, W. K., Knott, R. B., "The Nanoscale Structural Response to a Natural Kaolinitic Clayey Soil Subjected to Uniaxial Compression," Appl. Clay Sci. **29**, 1 (2005).

Jacob, R. E., Teter, J., Saam, B., Chen, W. C., Gentile, T. R., "Low-Field Orientation Dependence of ^{3}He Relaxation in Spin-Exchange Cells," Phys. Rev. A **69**, 021401 (2004).

Jacobson, D. L., Allman, B. E., McMahon, P. J., Nugent, K. A., Paganin, D., Arif, M., Werner, S. A., "Thermal and Cold Neutron Phase-Contrast Radiography," Appl. Radiat. Isotop. **61** (4), 547 (2004).

Jeng, U. S., Hsu, C. H., Lin, T. L., Wu, C.-M., Chen, H.-L., Tai, L.-A., Hwang, K.-C., "Dispersion of Fullerenes in Phospholipids Bilayers and the Subsequent Phase Changes in the Host Bilayers," Physica B **357** (1-2), 193 (2005).

Jeong, H. K., Krych, W., Ramanan, H., Nair, S., Marand, E., Tsapatsis, "Fabrication of Polymer/Selective-Flake Nanocomposite Membranes and Their Use in Gas Separation," Chem. Mater. **16**, 3838 (2004).

Jones, C. Y., Wu, J., Li, L., Haile, S. M., "Hydrogen—Content in Doped and Undoped $BaPrO_3$—and $BaCeO_3$ by Cold Neutron Prompt-Gamma Activation Analysis," J. Appl. Phys. **97**, 114908 (2005).

Jones, C. Y., Luecke, W. E., Copland, E., "Neutron Diffraction Study of Oxygen Dissolution in α_2-Ti_3Al," Intermetallics, in press.

Jones, G. L., Baker, J., Chen, W. C., Collett, B., Cowan, J. A., Dias, M. F., Gentile, T. R., Hoffmann, C., Koetzle, T., Lee, W. T., Litrell, K., Miller, M., Schultz, A., Snow, W. M., Tong, X., Yan, H., Yue, A., "Continuously Operating Compact ^{3}He Based Neutron Spin Filter," Physica B **356** (1-4), 86 (2005).

Jones, R. L., Hu, T. J., Lin, E. K., Wu, W. L., Goldfarb, D. L., Angelopoulos, M., Trinque, B. C., Schmid, G. M., Stewart, M. D., Willson, C. G., "Formation of Deprotected Fuzzy Blobs in Chemically Amplified Resists," J. Polym. Sci., Part B: Polym. Phys. **42** (17), 3063 (2004).

Jorge, G. A., Capan, C., Ronning, F., Jaime, M., Kenzelmann, M., Gasparovic, G., Broholm, C., Shapiro, A. Y., Demianets, L. A., "Specific Heat at the Magnetic Order Transitions in $RbFe(MoO_4)_2$," Physica B **354** (1-4), 297 (2004).

Kaler, E. W., Herrington, K. L., Iampietro, D. J., Coldren, B. A., Jung, H. T., Zasadzinski, J. A., "Phase Behavior and Microstructure in Aqueous Mixtures of Cationic and Anionic Surfactants," Chapter 9, in *Mixed Surfactant Systems, Second Edition*, edited by Abe, M., Scamehorn, J. (Marcel Dekker, New York), p. 289 (2005).

Kalur, G. C., Raghavan, S. R., "Anionic Wormlike Micellar Fluids that Display Cloud Points: Rheology and Phase Behavior," J. Phys. Chem. B **109** (18), 8599 (2005).

Kang, H. J., Dai, P., Mook, H. A., Lynn, J. W., Kurita, Y., Komiya, S., Ando, Y., "Electronically Competing Phases and Their Magnetic Field Dependence in Electron-Doped Nonsuperconducting and Superconducting $Pr_{1.88}LaCe_{0.12}CuO_{4\pm\delta}$," Phys. Rev. B **71**, 214512 (2005).

Karunadasa, H., Huang, Q., Ueland, B. G., Lynn, J. W., Schiffer, P., Regan, K. A., Cava, R. J., "Honeycombs of Triangles and Magnetic Frustration in SrL_2O_4 (L=Gd, Dy, Ho, Er, Tm, Yb)," Phys. Rev. B **71**, 144414 (2005).

Kent, M. S., Yim, H., Sasaki, D. Y., Satija, S., Seo, Y. S., Majewski, J., "Adsorption of Myoglobin to Cu(II)-IDA and Ni(II)-IDA Functionalized Langmuir Monolayers: Study of the Protein Layer Structure During the Adsorption Process by Neutron and X-Ray Reflectivity," Langmuir **21**, 6815 (2005).

Kenzelmann, M., Batista, C. D., Chen, Y., Broholm, C., Reich, D. H., Park, S., Qiu, Y., "The S=1/2 Chain in a Staggered Field: High Energy Bound-Spinon State and the Effects of a Discrete Lattice," Phys. Rev. B **71**, 094411 (2005).

Kenzelmann, M., Harris, A. B., Jonas, S., Broholm, C., Schefer, J., Kim, S. B., Zhang, S. B., Sheong, S. W., Vajk, O. P., Lynn, J. W., "Magnetic Inversion Symmetry Breaking and Ferroelectricity in $TbMnO_3$," Phys. Rev. Lett., in press.

Kepa, H., Majkrzak, C. F., Sankowski, P., Kacman, P., Giebultowicz, T. M., "Neutron Diffraction and Reflectivity Studies of Eu Chalcogenide Based Superlattices," J. Alloys Compd., in press.

Kepa, H., Sankowski, P., Kacman, P., Majkrzak, C. F., Sipatov, A. Y., Giebultowicz, T. M., "Neutron Scattering Studies of the Spin Structure of Magnetic Semiconductor Superlattices," AIP Conf. Proc. **772** (1), 313 (2005).

Kim, M. H., Glinka, C. J., "Application of *In Situ* Vapor Sorption Small Angle Neutron Scattering (SANS) to Semi-Crystalline Polymers: Vapor Pathway and Structure Evolution in Semi-Crystalline Linear Polyethylene," J. Appl. Cryst., in press.

Kintzel Jr, E. J., Herwig, K. W., Peral, I., "Structure and Dynamics Within Monolayer Organic Films Using Neutron Scattering," *Proceedings of the 11th International Conference on Composites/Nanoengineering* ICCE-11, **361** (2004).

Kirby, B. J., Borchers, J. A., Rhyne, J. J., O'Donovan, K. V., Wojtowicz, T., Liu, X., Ge, Z., Shen, S., Furdyna, J. K., "Effects of Capping on the $Ga_{1-x}Mn_xAs$ Magnetic Depth Profile," Appl. Phys. Lett. **86** (7), 072506 (2005).

Kirstein, O., Prager, M., Dimeo, R. M., Desmedt, A., "Rotational Dynamics of Methyl Groups in m-Xylene," J. Chem. Phys. **122** (1), 014502 (2005).

Kiryukhin, V., Borissov, A., Ahn, J. S., Huang, Q., Lynn, J. W., Cheong, S. W., "Correlated and Uncorrelated Nanoscale Lattice Distortions in the Paramagnetic Phase of Magnetoresistive Manganites," Phys. Rev. B **70** (21), 214424 (2004).

Klupp, G., Kamarás, O. G., Nemes, N. M., Brown, C. M., Leao, J., "Distortion and Orientation of Fulleride Ions in A_4C_{60}," AIP Conf. Proc. **723** (1), 8 (2004).

Koga, T., Akashige, E., Reinstein, A., Bronner, M., Seo, Y. S., Shin, K., Rafailovich, M. H., Sokolov, J. C., Chu, B., Satija, S. K., "The Effect of Density Fluctuations in Supercritical Fluids: New Science and Technology for Polymer Thin Films," Physica B **357** (1-2), 73 (2005).

Koga, T., Ji, Y., Seo, Y. S., Gordon, C., Qu, F., Rafailovich, M. H., Sokolov, J. C., Satija, S. K., "Neutron Reflectivity Study of Glassy Polymer Brushes in Density Fluctuating Supercritical Carbon Dioxide," J. Polym. Sci., Part B: Polym. Phys. **42** (17), 3282 (2004).

Kreyssig, A., Stockert, O., Reznik, D., Woodward, F. M., Lynn, J. W., Bitterlich, H., Souptel, D., Behr, G., Loewenhaupt, M., "Magnetic Excitations of RNi_2B_2C Single Crystals with R=Tb and Ho," Physica C **408-410**, 100 (2004).

Krishnamurthy, L., Wagner, N. J., "The Influence of Wear Attractive Forces on the Microstructure and Rheology of Colloidal Dispersions," J. Rheol. **49** (2), 475 (2005).

Krueger, S., Perez-Salas, U. A., Gregurick, S. K., Kuzmanovic, D., "SANS from Proteins, Nucleic Acids, and Viruses," in *Neutron in Biology – Techniques and Applications*, edited by Fitter, J., Gutberlet, T., Katsaras, J. (Springer Biologica Physics Series, Springer Publishing, New York), in press.

Krueger, S., Ho, D., Tsai, A., "Small Angle Neutron Scattering as a Probe for Protein Aggregation at Many Length Scales," in *Misbehaving Proteins: Protein (Mis) Folding, Aggregation and Stability,* (Kluwer Academic Publishers, New York), in press.

Kučera, J., Zeisler, R., "Do We Need Radiochemical Separation in Activation Analysis?" J. Radioanal. Nucl. Chem. **262** (1), 255 (2004).

Kučera, J., Zeisler, R., "Low-Level Determination of Silicon in Biological Materials Using Radiochemical Neutron Activation Analysis," J. Radioanal. Nucl. Chem. **263** (3), 811 (2005).

Kulkarni, A. A., Sampath, S., Goland, A., Herman, H., Allen, A. J., Ilavsky, J., Gong, W. Q., Gopalan, S., "Plasma Spray Coatings for Producing Next-Generation Supported Membranes," Top. Catal. **32** (3-4), 241 (2005).

Kulkarni, A. A., Goland, A., Herman, H., Allen, A. J., Ilavsky, J., Long, G. G., De Carlo, F., "Advanced Microstructural Characterization of Plasma-Sprayed Zirconia Coatings Over Extended Length Scales," J. Therm. Spray Tech. **14** (2), 239 (2005).

Lamaze, G. P., Chen-Mayer, H. H., Soni, K. K., "Analysis of Thin Films and Surfaces by Cold Neutron Depth Profiling," App. Surf. Sci. **238** (1-4), 108 (2004).

Landrigan, P. J., Lioy, P. J., Thurston, G., Berkowitz, G., Chen, L. C., Chillrud, S. N., Gavett, S. H., Georgopoulos, P. G., Geyh, A. S., Levin, S., Perera, F., Rappaport, S. M., Small, C., the NIEHS World Trade Center Working Group, "Health and Environmental Consequences of the World Trade Center Disaster," Environ. Health Perspect. **112** (6), 731 (2004).

La-Orauttapong, D., Toulouse, J., Ye, Z. G., Chen, W., Erwin, R., Robertson, J. L., "Neutron Scattering Study of the Relaxor Ferroelectric $(1\text{-}x)Pb(Zn_{1/3}Nb_{2/3})O_{3\text{-}x}PbTiO_3$," Phys. Rev. B **67**, 34110 (2003).

Larochelle, S., Mehta, A., Lu, L., Mang, P. K., Vajk, O. P., Kaneko, N., Lynn, J. W., Zhou, L., Greven, M., "Structural and Magnetic Properties of the Single-Layer Manganese Oxide $La_{1\text{-}x}Sr_{1+x}MnO_4$," Phys. Rev. B **71** (2), 024435 (2005).

Law, M., Prask, H., Luzin, V., Gnaeupel-Herold, T., "Residual Stress Measurements in Gas Pipelines," *Proceedings of the TMS Annual Meeting,* (February 2005, San Francisco, CA), in press.

Lawes, G., Harris, A. B., Kimura, T., Rogadi, N., Cava, R. J., Aharony, A., Entin-Wohlman, O., Yildirim, T., Kenzelmann, M., Broholm, C., Ramirez, A. P., "Magnetically Driven Ferroelectric Order in $Ni_3V_2O_8$," Phys. Rev. Lett. **95**, 08705 (2005).

Lawes, G., Kenzelmann, M., Rogado, N., Kim, K. H., Jorge, G. A., Cava, R. J., Aharony, A., Entin-Wohlman, O., Harris, A. B., Yildirim, T., Huang, Q. Z., Park, S., Broholm, C., Ramirez, A. P., "Competing Phases on a Kagomé Staircase," Phys. Rev. Lett. **93** (34), 247201 (2004).

Lee Jr., C. T., Smith, K. A., Hatton, T. A., "Photocontrol of Protein Folding: The Interaction of Photosensitive Surfactants with Bovine Serum Albumin," Biochem. **44**, 524 (2004).

Lee, J. H., Gustin, J. P., Payne, G. F., Raghavan, S. R., "Vesicle-Biopolymer Gels: Networks of Surfactant Vesicles Connected by Associating Biopolymers," Langmuir **21**, 26 (2005).

Lee, J. S., Quirk, R. P., Foster, M. D., "Effect of Butadiene End-Capping of Arms in a Star Polystyrene on Solution Properties, Bulk Dynamics and Bulk Thermodynamic Interactions in Binary Blends," Macromol. **37**, 10199 (2004).

Lee, S.-H., Louca, D., Ueda, H., Park, S., Sato, T. J., Isobe, M., Ueda, Y., Rosenkranz, S., Zscack, P., Íñiguez, J., Qiu, Y., Osborn, R., "Orbital and Spin Chains in ZnV_2O_4," Phys. Rev. Lett. **93** (15), 156407 (2004).

Lelong, G., Price, D. L., Douy, A., Kline, S., Brady, J. W., Saboungi, M. L., "Molecular Dynamics of Confined Glucose Solutions," J. Chem. Phys. **122**, 164504 (2005).

Lettow, J. S., Lancaster, T. M., Glinka, C. J., Ying, J. Y., "Small Angle Neutron Scattering and Theoretical Investigation of Polythylene Oxide - Polypropylene Oxide - Polyethylene Oxide Stabilized in Oil-in-Water Microemulsions," Langmuir **21** (13), 5738 (2005).

Levin, I., Huang, Q. Z., Cook, L. P., Wong-Ng. W., "Nonquenchable Chemical Order-Disorder Phase Transition in Yttrium Oxyfluoride," Euro. J. Inorg. Chem. **1**, 87 (2005).

Levin, I., Vanderah, T. A., Amos, T. G., Maslar, J. E., "Structural Behavior and Raman Spectra of Perovskite-Like Solid Solutions $(1\text{-}x)LaMg_{0.5}Ti_{0.5}O_{3\text{-}x}La_{2/3}TiO_3$," Chem. Mater. **17**, 3273 (2005).

Lewis, M. J., Gaulin, B. D., Filion, L., Kallin, C., Berlinsky, A. J., Dabkowska, H. A., Qiu, Y., Copley, J. R. D., "Ordering and Spin Waves in $NaNiO_2$: A Stacked Quantum Ferromagnet," Phys. Rev. B **72**, 014408 (2005).

Li, J., Sleight, A. W., Jones, C. Y., Toby, B. H., "Trends in Negative Thermal Expansion Behavior for AMO_2 (A=Cu or Ag, M= Al, Sc, In, or La) Compounds with the Delafossite Structure," J. Solid State Chem. **178** (1), 285 (2005).

Li, J., Subramanian, M. A., Rosenfeld, H. D., Jones, C. Y., Toby, B. H., Sleight, A. W., "Clues to the Giant Dielectric Constant of $CaCu_3Ti_4O_{12}$ in the Defect Structure of $SrCu_3Ti_4O_{12}$," Chem. Mater. **16**, 5223 (2004).

Li, J., Yokochi, A. F. T., Sleight, A. W., "Oxygen Intercalation of Two Polymorphs of $CuScO_2$," Solid State Sci. **6**, 831 (2005).

Li, L., Vaidya, T., Sampath, S., Gouldstone, A., Luzin, V., Prask, H., "Residual Stress Analysis of Thermal Sprayed Molybdenum Deposit," Mater. Sci. Forum **490** (1), 607 (2005).

Lin, E. K., Jones, R. L., Barker, J. G., Bolton, P. J., Barclay, G. G., "Structural Characterization of Deep-Submicron Lithographic Structures Using Small-Angle Neutron Scattering," Proc. SPIE Int. Soc. Opt. Eng. **4689**, 541 (2003).

Lin, Q., Greenblatt, M., Croft, M., "Evolution of Structure and Magnetic Properties in Electron-Doped Double Perovskites, $Sr_{2\text{-}x}La_xMnWO_6$ $(0 \leq x \leq 1)$," J. Solid State Chem **178**, 1356 (2005).

Lindstrom, R. M., "An Improved Radiochemical Neutron Activation Analysis Procedure for Trace Mercury," J. Radioanal. Nucl. Chem. **263** (3), 787 (2005).

Lindstrom, R. M., "Beams and Facilities," Chapter 2, in *Handbook of Prompt-Gamma Activation Analysis*," edited by Molnár, G. L., (Kluwer Academic Publishers, Dordrecht), p. 31 (2004).

Lindstrom, R. M., Blaauw, M., Unterweger, M., "The Half-Lives of ^{24}Na, ^{42}K, and ^{198}Au," J. Radioanal. Nucl. Chem. **263** (2), 311 (2005).

Lindstrom R. M., Yonezawa, C., "Samples and Standards," Chapter 3, in *Handbook of Prompt-Gamma Activation Analysis*, edited by Molnár, G. L. (Kluwer Academic Publishers, Dordrecht), p. 59 (2004).

Lindstrom, R. M., Zeisler, R., Greenberg, R. R., "Accuracy and Uncertainty in Radioactivity Measurement for NAA," J. Radioanal. Nucl. Chem., in press.

Lin-Gibson, S., Jones, R. L., Washburn, N. R., Horkay, F., "Structure-Property Relationships of Photopolymerizable Poly(Ethylene Glycol) Dimethacrylate Hydrogels," Macromol. **38**, 2897 (2005).

Liu, L., Chen, S. H., Faraone, A., Yen, C. W., Mou, S. Y., "Pressure Dependence of Fragile-to-Strong Transition Temperature in Deeply Supercooled Confined Water," Phys. Rev. Lett., in press.

Liu, L., Faraone, A., Mou, C.–Y., Yen, C.–W., –Shen, S.–H., "Slow Dynamics of Supercooled Water Confined in Nanoporous Silica Materials," J. Phys.: Condens. Matter **16**, S5403 (2004).

Liu, L., Singh, M., John, V. T., McPherson, G. L., He, J., Agarwal, V., Bose, A., "Shear Induced Alignment and Nanowire Silica Synthesis in a Rigid Crystalline Surfactant Mesophase," J. Am. Chem. Soc. **126** (8), 2276 (2004).

Liu, S., Gonzalez, Y. I., Danino, D., Kaler, E. W., "Polymerization of Wormlike Micelles Induced by Hydrotropic Salt," Macromol. **38**, 2482 (2005).

Liu, Y., Chen, W. R., Chen, S. H., "Cluster Formation in Two Yukawa Fluids," J. Chem. Phys. **122**, 044507 (2005).

Liu, Y., Fratini, E., Baglioni, P., Chen, W. R., Chen, S. H., "An Effective Long-Range Attraction Between Protein Molecules in Solutions Studied by Small Angle Neutron Scattering," Phys. Rev. Lett., in press.

Llobet, A., Gardner, J. S., Moshopoulou, E. G., Mignot, J. M., Nicklas, M., Bao, W., Moreno, N. O., Pagliuso, P. G., Sarrao, J. L., Thompson, J. D., Goncharenko, I. N., "Magnetic Structure of $CeRhIn_5$ as a Function of Pressure and Temperature," Phys. Rev. B **69**, 024403 (2004).

Loizou, E., Butler, P., Porcar, L., Kesselman, E., Talmon, I., Dundigalla, A., Schmidt, G., "Large Scale Structures in Nanocomposite Hydrogels," Macromol. **38** (6), 2047 (2005).

Lonetti, B., Fratini, E., Chen, S. H., Baglioni, P., "Viscoelastic and Small Angle Neutron Scattering of Concentrated Protein Solutions," Phys. Chem. Chem. Phys. **6**, 1388 (2004).

Luzin, V., Gnäupel-Herold, T., Gordon, J. E., Prask, H. J., "Neutron Residual Stress Measurements on Rail Sections for Different Production Conditions," *ASME International Mechanical Engineering Congress* **3**, (2004).

Lynn, J. W., "Recent Neutron Results on Magnetic Superconductors and Related Systems," Physica B **354** (1-4), 246 (2004).

Maciejczyk, P. B., Zeisler, R., Hwang, J. S., Thurston, G. D., Chen, L. C., "Characterization of Size-Fractioned World Trade Center Dust and Estimation of Relative Dust Contribution to Ambient Concentrations," ACS Symp. Ser., in press.

Mackey, E. A., Anderson, D. L., Liposky, P. J., Lindstrom, R. M., Chen-Mayer, H. H., Lamaze, G. P., Simons, D. S., Thompson, P. E., "New Thermal Neutron Prompt Gamma-Ray Activation Analysis Instrument at the National Institute of Standards and Technology Center for Neutron Research," Nucl. Instrum. Methods B **226** (3), 426 (2004).

Mackey, E. A., Paul, R. L., Lindstrom, R. M., Anderson, D. L., "Sources of Uncertainty in Prompt Gamma-Ray Activation Analysis," J. Radioanal. Nucl. Chem. **265** (2), 273 (2005).

Majkrzak, C. F., Berk, N. F., Krueger, S., Perez-Salas, U. A., "Structural Investigations of Membranes of Interest in Biology," in *Neutrons in Biology- Techniques and Applications*, edited by Fitter, J., Gutberlet, T., Katsaras, J. (Springer Publishing), in press.

Majkrzak, C. F., O'Donovan, K. V., Berk, N. F., "Polarized Neutron Reflectometry," in *Neutron Scattering from Magnetic Materials*, edited by Chatterji, T., (Elsevier), in press.

Malwitz, M. M., Butler, P. D., Porcar, L., Angelette, D. P., Schmidt, G., "Orientation and Relaxation of Polymer-Clay Solutions Studied by Rheology and Small-Angle Neutron Scattering," J. Polym. Sci., Part B: Polym. Phys. **42**, 3102 (2004).

Malwitz, M. M., Dundigalla, A., Ferreiro, V., Butler, P. D., Henk, M. C., Schmidt, G., "Layered Structures of Shear-Oriented and Multilayered PEO-Silicate Nanocomposite Films," Phys. Chem. Chem. Phys. **6** (11), 2977 (2004).

Mamontov, E., "Comment on 'Quasielastic Neutron Scattering of Two-Dimensional Water in a Vermiculite Clay' [J. Chem. Phys. 113, 2873 (2003)] and 'A Neutron Spin-Echo Study of Confined Water' [J. Chem Phys. 115, 11299 (2001)]," J. Chem. Phys. **121** (18), 9194 (2004).

Mamontov, E., "Dynamics of Surface Water in ZrO_2 Studied by Quasielastic Neutron Scattering," J. Chem. Phys. **121**, 9087 (2004).

Mamontov, E., "High-Resolution Neutron-Scattering Study of Slow Dynamics of Surface Water Molecules in Zirconium Oxide," J. Chem. Phys. **123**, 024706 (2005).

Mamontov, E., Kumzerov, Y., A., Vakhrushev, S. B., "Translational Dynamics of Water in the Nano-Channels of Oriented Chrysotile Asbestos Fibers," Phys. Rev. E **71**, 061502 (2005).

Mamontov, E., Udovic, T. J., Isnard, O., Rush, J. J., "Neutron Scattering Study of Hydrogen Dynamics in $Pr_2Fe_{17}H_5$," Phys. Rev. B **70**, 214305 (2004).

Mang, P. K., Larochelle, S., Mehta, A., Javk, O. P., Erickson, A. S., Lu, L., Buyers, W. J. L., Marshall, A. F., Prokes, K., Greven, M., "Phase Decomposition and Chemical Inhomogenity in $Nd_{2-x}Ce_xCuO_{4\pm\delta}$," Phys. Rev. B **70**, 094507 (2004).

Martínez-Iñesta, M. M., Peral, I., Lobo, R. F., Proffen, T., "A Pair Distribution Function Analysis of Zeolite Beta," Microporous Mesoporous Mater. **77** (1), 55 (2004).

Martinez-Perez, M. L., Mompean, F. J., Ruiz-Hervias, J., Borlado, C. R., Atienza, J. M., Garcia-Hernadez, M., Elices, M., Gil-Sevillano, J., Peng, R. L., Buslaps, T., "Residual Stress Profiling in the Ferrite and Cementite Phases of Cold-Drawn Steel Rods by Synchrotron X-Ray and Neutron Diffraction," Acta Mater. **52** (18), 5303 (2004).

Mason, T. G., Lin, M. Y., "Density Profiles of Temperature Sensitive Microgel Particles," Phys. Rev. E **71**, 040801 (2005).

Masuda, T., Zheludev, A., Grenier, B., Imai, S., Uchinokura, K., Ressouche, E., Park, S., "Cooperative Ordering of Gapped and Gapless Spin Networks in $Cu_2Fe_2Ge_4O_{13}$," Phys. Rev. Lett. **93** (7), 077202 (2004).

Masuda, T., Zheludev, A., Uchinokura, K., Chung, J. H., Park, S., "Dynamics and Scaling in a Quantum Spin Chain Material with Bond Randomness," Phys. Rev. Lett. **93** (7), 077206 (2004).

McElhanon, J. R., Zifer, T., Kline, S. R., Wheeler, D. R., Loy, D. A., Jamison, G. A., Long, T. M., Rahimian, K., Simmons, B. A., "Thermally Cleavable Surfactants Based on Furanmaleimide Diels-Alder Adducts," Langmuir **21** (8), 3259 (2005).

McQueeney, R. J., Yethiraj, M., Montifrooij, W., Gardner, J. S., Metcalf, P., Honig, J. M., "Influence of the Verwey Transition on the Spin-Wave Dispersion of Magnetite," J. App. Phys. **97**, 10A902 (2005).

Mildner, D. F. R., "Resolution of Small-Angle Scattering with a Refractive Focusing Optic," J. Appl. Crystallogr. **38**, 488 (2005).

Miller, C. E., Majewski, J., Kjaer, K., Weygand, M., Faller, R., Satija, S., Kuhl, T. L., "Neutron and X-ray Scattering Studies of Cholera Toxin Interactions with Lipid Monolayers at the Air-Liquid Interface," Colloids Surf., B **40** (3-4), 159 (2005).

Morfin, I., Horkay, F., Basser, P. J., Bley, F., Hecht, A. M., Rochas, C., Geissler, E., "Absorption of Divalent Cations on DNA," Biophys. J. **87**, 1 (2004).

Mumm, H. P., Garcia, A., Grout, L., Howe, M., Parazzoli, L. P., Robertson, R. G. H., Sundqvist, K. M., Wilkerson, J. F., Freedman, S. J., Fujikawa, B. K., Lising, L. J., Dewey, M. S., Nico, J. S., Thompson, A. K., Chupp, T. E., Cooper, R. L., Coulter, K. P., Hwang, S. R., Welsh, R. C., Broussard, L. J., Trull, C. A., Wietfeldt, F. E., Jones, G. L., "emiT: An Apparatus to Test Time Reversal Invariance in Polarized Neutron Decay," Rev. Sci. Instrum. **75** (12), 5342 (2004).

Nair, S., Chowdhuri, Z., Peral, I., Neumann, D. A., Dickinson, L. C., Tompsett, G., Jeong, H. K., Tsapatsis, M., "Translational Dynamics of Water in a Nanoporous Layered Silicate," Phys. Rev. B **71**, 104301 (2005).

Nair, S., Dimeo, R. M., Neumann, D. A., Horsewill, A. J., Tsapatsis, M., "Methyl Rotational Tunneling Dynamics of *p*-xylene Confined in a Crystalline Zeolite Host," J. Chem. Phys. **121** (10), 4810 (2004).

Nico, J. S., Arif, M., Dewey, M. S., Gentile, T. R., Gilliam, D. M., Huffman, P. R., Jacobson, D. L., Thompson, A. K., "The Fundamental Neutron Physics Facilities at NIST," J. Res. Natl. Inst. Stand. Technol. **110**, 137 (2005).

Nieh, M. P., Kumar, S. K., Fernando, R. H., Colby, R. H., Katsaras, J., "Effect of the Hydrophilic Size on the Structural Phases of Aqueous Nonionic Gemini Surfactant Solutions," Langmuir **20**, 9061 (2004).

Nieh, M. P., Raghunathan, V. A., Glinka, C. J., Harroun, T. A., Katsaras, J., "Magnetically Alignable Phase of Phospholipid 'Bicelle' Mixtures is a Chiral Nematic Made Up of Worm-Like Micelles," Langmuir **20**, 7893 (2004).

Nieh, M. P., Raghunathan, V. A., Glinka, C. J., Harroun, T. A., Katsaras, J., "Structural Phase Behavior of High-Concentration, Alignable Biomimetic 'Bicelle' Membranes," Macromol. Symp. **219**, 135 (2005).

Nieh, M. P., Raghunathan, V. A., Kline, S. R., Harroun, T. A., Huang, C. Y., Pencer, J., Katsaras, J., "Spontaneously Formed Unilamellar Vesicles with Path- Dependent Size Distribution," Langmuir **21**, 6566 (2005).

Norman, A. I., Ho, D. L., Karim, A., Amis, E. J., "Phase Behavior of Block Co-Poly(Ethylene Oxide-Butylene Oxide), E(18)B(9) in Water, by Small Angle Neutron Scattering," J. Colloid Interface Sci. in press.

Odette, G. R., Yamamoto, T., Klingensmith, D., "On the Effect of Dose Rate on Irradiation Hardening of RPV Steels," Phil. Mag. **85** (4-7), 779 (2005).

Ollivier, J., Plazanet, M., Schober, H., Cook, J. C., "First Results with the Upgraded IN5 Disk Chopper Cold Time-of-Flight Spectrometer," Physica B **350**, 173 (2004).

Olsson, S., Hjörvarsson, B., "Effect of Biaxial Elastic Constraints on H-H Interaction in Ultrathin Vanadium," Phys. Rev. B **71**, 035414 (2005).

Otano-Rivera, W., Messier, R., Pilione, L. J., Santiago, J. J., Lamaze, G. P., "Effect of Al Additions and AlN Interlayers on the Stablization of cBN Sputtered Thin Films," Diamond & Relat. Mater. **13** (9), 1690 (2004).

Ouyang, Z. W., Wang, F. W., Huang, Q. Z., Liu, W. F., Liu, G. Y., Lynn, J. W., Liang, J. K., Rao, G. H., "Temperature Dependent Neutron Powder Diffraction Study of the Laves Phase Compound $TbCo_2$," J. Alloys Compd. **390** (1-2), 21 (2005).

Ouyang, Z. W., Wang, F. W., Huang, Q., Liu, W. F., Xiao, Y. G., Lynn, J. W., Rao, G. H., "Magnetic Structure, Magnetorestriction, and Magnetic Transitions of the Laves-Phase Compound $NdCo_2$," Phys. Rev. B **71** (6), 064405 (2005).

Ozbas, B., Rajagopal, K., Schneider, J. P., Pochan, D. J., "Semiflexible Chain Networks Formed via Folding and Self-Assembly of β-Hairpin Molecules," Phys. Rev. Lett. **93**, 268106 (2004).

Page, M., Warr, G. G., "Structure and Dynamics of Self-Assembling Aluminum Didodecyl Phosphate Organogels," J. Chem. Phys. **108**, 16983 (2004).

Page, S. A., Bowman, J. D., Carlini, R. D., Case, T., Chupp, T. E., Coulter, K. P., Dabaghyan, M., Desai, D., Freedman, S. J., Gentile, T. R., Gericke, M. T., Gillis, R. C., Greence, G. L., Hersman, F. W., Ino, T., Ishimoto, S., Jones, G. L., Lauss, B., Leushner, M. B., Losowski, B., Mahurin, R., Masuda, Y., Mitchell, G. S., Nann, H., Penttilä, S. I., Ramsay, W. D., Santra, S., Seo, P. N., Sharapov, E. I., Smith, T. B., Snow, W. M., Wilburn, W. S., Yuan, V., Zhu, H., "Measurement of Parity in np Capture: the NPD Gamma Experiment," J. Res. Natl. Inst. Stand. Technol. **110** (3), 195 (2005).

Paliwal, A., Asthagiri, D., Bossev, D. P. Paulaitis, M. E., "Pressure Denaturation of Staphylococcal Nuclease Studied by Neutron Small-Angle Scattering and Molecular Simulation," Biophys. **87**, 3479 (2004).

Pancras, J. P., Ondov, J. M., Zeisler, R., "Multi- Element Electrothermal AAS Determination of 11 Marker Elements in Fine Ambient Aerosol Slurry Samples Collected with SEAS-II," Analyt. Chim. Acta **538** (1-2), 303 (2005).

Park, M. J., Char, K., Bang, J., Lodge, T. P., "Order-Disorder Transition and Critical Micelle Temperature in Concentrated Block Copolymer Solutions," Macromol. **38** (6), 2449 (2005).

Paul, R. L., "Determination of Boron in Materials by Cold Neutron Prompt Gamma-Ray Activation Analysis," Analysis **130** (1), 99 (2005).

Paul, R. L., "Determination of Hydrogen in Semiconductors and Related Materials by Cold Neutron Prompt Gamma-Ray Activation Analysis," *Materials Research Society Proceedings*, in press.

Perahia, D., Jiao, X., Triphol, R., "From the Conformation of a Single Molecule to Physical Networks in Highly Interacting Polymers: A Small-Angle Neutron Study," J. Polym. Sci., Part B: Polym. Phys. **42**, 3165 (2004).

Peral, I., Curtis, J. E., Chakoumakos, B. C., Jones, C. Y., "Structure and Dynamics of Propylene Oxide and Trimethylene Oxide Clathrate Hydrates," Mater. Res. Soc. Symp. Proc. **840**, Q2.1 (2005).

Perego, R. C., Blaauw, M., "Incoherent Neutron-Scattering Determination of Hydrogen Content: Theory and Modeling," J. Appl. Phys. **97**, 123533 (2005).

Peterson, V. K., Neumann, D. A., Livingston, R. A., "Hydration of Tricalcium and Dicalcium Silicate Mixtures Studied Using Quasielastic Neutron Scattering," J. Phys. Chem. B, **109**, 14449 (2005).

Peterson, V. K., Neumann, D. A., Livingston, R. A., "Interactions of Hydrating Tricalcium and Dicalcium Silicate using Time-Resolved Quasielastic Neutron Scattering," Mater. Res. Soc., Symp. Proc. **840**, Q2.2 (2004).

Phair, J. W., Livingston, R. A., Brown, C. M., Benes, A. J., "Investigation of the State of Water in Hydrating Layered and Amorphous Sodium Disilicate (Alkali-Silica Reactants) by Quasi-Elastic Neutron Scattering," Chem. Mater. **16** (24), 5042 (2005).

Pivovar, A. M., Pivovar, B. S., "The Dynamic Behavior of Water Within Polymer Electrolyte Fuel Cell Membrane at Low Hydration Levels," J. Phys. Chem. B **109** (2), 785 (2005).

Pochan, D. J., Pakstis, L., Nowak, A. P., Deming, T. J., "Self-Assembled Polypeptide Hydrogels: Morphology and Cytotoxicity," Biomacrom., in press.

Porcar, L., Hamilton, W. A., Butler, P. D., Warr, G. G., "Relaxation of a Shear-Induced Lamellar Phase Measured with Time Resolved Small Angle Neutron Scattering," Physica B **350** (1-3), E963 (2004).

Porcar, L., Hamilton, W. A., Butler, P. D., Warr, G. G., "Topological Relaxation of a Shear-Induced Lamellar Phase to Sponge Equilibrium and the Energetics of Membrane Fusion," Phys. Rev. Lett. **93** (19), 198301 (2004).

Porcar, L., Warr, G. G., Hamilton, W. A., Butler, P. D., "Shear-Induced Collapse in a Lyotropic Lamellar Phase," Phys. Rev. Lett. **95**, 078302, (2005).

Prabhu, V. M., Amis, E. J., Bossev, D. P., Rosov, N., "Counterion Associative Behavior with Flexible Polyelectrolytes," J. Chem Phys. **121** (9), 4424 (2004).

Prabhu, V. M., Vogt, B. D., Wu, W.-L., Douglas, J. F., Lin, E. K., Satija, S. K., Goldfarb, D. L., Ito, H., "Direct Measurement of the Counterion Distribution Within Swollen Polyelectrolyte Films," Langmuir **21** (15), 6447 (2005).

Prince, E., Toby, B. H., "A Comparison of Methods for Modeling the Effect of Axial Divergence in Powder Diffraction," J. Appl. Phys., in press.

Qiu, Y., Broholm, C., Ishiwata, S., Azuma, M., Takano, M., Bewley, R., Buyers, W. J. L., "Spin-Trimer Antiferromagnetism in $La_4Cu_3MoO_{12}$," Phys. Rev. B. **71**, 214439 (2005).

Ramakrishnan, S., Gopalakrishnan, V., Zukoski, C. F., "Clustering and Mechanics in Dense Depletion and Thermal Gels," Langmuir, in press.

Rao, G. H., Liu, W. F., Huang, Q., Ouyang, Z. W., Wang, F. W., Xiao, Y. G., Lynn, J. W., Liang, J. K., "Magnetic Structure and Magnetization Process of $NdCo_{12-x}V_x$," Phys. Rev. B **71**, 144430 (2005).

Ratcliff II, W., Kiryukhin, V., Kenzelmann, M., Lee, S.-H., Erwin, R., Schefer, J., Hur, N., Park, S., Cheong, S.-W., "Magnetic Phase Diagram of the Colossal Magnetoelectric $DyMn_2O_5$," Phys. Rev. B, in press.

Reents-Budet, D., Bishop, R. L., Audet, C., Awe, J., Blackman, M. J., "Act Locally, Think Internationally: The Pottery of Baking Pot, Belize," in *Archeological Investigations in the Eastern Maya Lowlands: Papers of the 2004 Belize Archaeology Symposium*, edited by Awe, J., Morris, J., Jones, S., and Helmke, C. (Research Reports in Belizean Archaeology, Volume 2. Institute of Archaeology, Belize, Print Belize Limited, Belmopan), p. 365 (2005).

Regan, K. A., Huang, Q., Cava, R. J., "Isolated Spin 3/2 Plaquettes in Na_3RuO_4," J. Solid State Chem. **178** (6), 2104 (2005).

Reynolds, B. J., Ruegg, M. L., Balsara, N. P., Radke, C. J., Schaffer, T. D., Lin, M. Y., Shull, K. R., Lohse, D. J., "Thermodynamics of Polymer Blends Organized by Balanced Block Copolymer Surfactants Studied by Mean-Field Theories and Scattering," Macromol. **37**, 7401 (2005).

Rimer, J. D., Vlachos, D. G., Lobo, R. F., "Evolution of Self-Assembled Silica-Tetrapropylammonium Nanoparticles at Elevated Temperatures," J. Phys. Chem. B **109** (26), 12762 (2005).

Roh, J. H., Novikov, V. N., Gregory, R. B., Curtis, J. E., Chowdhuri, Z., Sokolov, A. P., "Onsets of Anharmonicity in Protein Dynamics," Phys. Rev. Lett. **95**, 038101 (2005).

Russo, D., Murarka, R. K., Copley, J. R. D., Head-Gordon, T., "Molecular View of Water Dynamics Near Model Peptides," J. Phys. Chem. B **109**, 12966 (2005).

Russo, D., Murarka, R. K., Hura, G., Verschell, E., Copley, J. R. D., Head-Gordon, T., "Evidence for Anomalous Hydration Dynamics Near a Model Hydrophobic Peptide," J. Phys. Chem. B **108**, 19885 (2004).

Ryu, D. Y., Lee, D. H., Jang, J., Kim, J. K., "Complex Phase Behavior of a Weakly Interacting Binary Polymer Blend," Macromol. **37**, 5851 (2004).

Sagi, E., Ofer, O., Keren, A., Gardner, J. S., "Quest for Frustration Driven Distortion in $Y_2Mo_2O_7$," Phys. Rev. Lett. **94**, 237202 (2005).

Sankowski, P., Kepa, H., Kacman, P., Sipatov, A. Y., Majkrzak, C. F., Giebultowicz, T. M., "Interlayer Coupling in EuS-Based Superlattices Deduced from Neutron Scattering Experiments," Acta Phys. Pol. A **105** (6), 607 (2004).

Santini, P., Caretta, S., Amoretti, G., Guidi, T., Caciuffo, R., Caneschi, A., Rovai, D., Qiu, Y., Copley, J. R. D., "Spin Dynamics and Tunneling of the Néel Vector in the Fe_{10} Magnetic Wheel," Phys. Rev. B **71**, 184405 (2005).

Sato, T., Lynn, J. W., Dabrowski, C. E., "Disorder-Induced Polaron Formation in the Magnetoresistive Perovskite $La_{0.54}Ba_{0.46}MnO_3$," Phys. Rev. Lett. **93** (26), 267204 (2004).

Schubert, B. A., Wagner, N. J., Kaler, E. W., Raghavan, S. R., "Shear-Induced Phase Separation in Solutions of Wormlike Micelles," Langmuir **20** (9), 3564 (2004).

Seah, M. P., Spencer, S. J., Bensebaa, F., Vickridge, I., Danzebrink, H., Krumrey, M., Gross, T., Oesterle, W., Wendler, E., Rheinländer, B., Azuma, Y., Kojima, I., Suzuki, N., Suzuki, M., Tanuma, S., Moon, D. W., Lee, H. J., Cho, H. M., Chen, H. Y., Wee, A. T. S., Osipowicz, T., Pan, J. S., Jordaan, W. A,. Hauert, R., Klotz, U., van der Marel, C., Verheijen, M., Tamminga, Y., Jeynes, C., Bailey, P., Biswas, S., Falke, U., Nguyen, N. V., Chandler-Horowitz, D., Ehrstein, J. R., Muller, D., Dura, J. A., "Critical Review of the Current Status of Thickness Measurements for Ultrathin SiO_2 on Si Part V: Results of a CCQM Pilot Study," Surf. Interface Anal. **36**, 1269 (2004).

Sears, E. L., Bishop, R. L., Blackman, M. J., "Las Figurillas de Cancuén: El Sugimiento de una Perspectiva Regional," *XVIII Simposio de Investigaciones Arqueológicas en Guatemala*, edited by Laporte, J. P., Arroyo, B., Mejía, H. E. (Museo Nacional de Arqueología y Etnología: Ministerio de Cultura y Deportes, Instituto de Antropología e Historia, Asociación Tikal, Foundation for the Advancement of Mesoamerican Studies, Inc.), p. 781 (2005).

Shamato, S., Yamada, N., Matsunaga, T., Proffen, T., Richardson, J. W., Chung, J. H., Egami, T., "Large Displacement of Germanium Atoms in Crystalline $Ge_2Sb_2Te_5$," Appl. Phys. Lett. **86**, 081904 (2005).

Sharma, P. K., Bhatia, S. R., "Effect of Anti-Inflammatories on Pluronic (R) F127: Micellar Assembly, Gelation and Partitioning," Inter. J. Pharm. **278** (2), 361 (2004).

Silverstein, M. S., Shach-Caplan, M., Bauer, B. J., Hedden, R. C., Lee, H. J., Landes, B. G., "Nanopore Formation in a Polyphenylene Low-*k* Dielectric," Macromol. **38** (10), 4301 (2005).

Singh, M., Ford, C., Agarwal, V., Fritz, G., Bose, A., John, V. T., McPherson, G. L., "Structural Evolution in Cationic Micelles Upon Incorporation of a Polar Organic Dopant," Langmuir **20** (23), 9931 (2004).

Singh, M., Tan, G., Agarwal, V., Fritz, G., Maskos, K., Bose, A., John, V., McPherson, G., "Structural Evolution of a Two Component Organogel," Langmuir **18**, 7392 (2004).

Sirota, E. B., "Physical Structure of Asphaltenes," Energy Fuels, in press.

Skripov, A. V., Soloninin, A. V., Buzlukov, A. L., Voyevodina, L. S., Cook, J. C., Udovic, T. J., Hemplemann, R., "Hydrogen Motion in C14-Type $HfCr_2H_x$: Quasielastic Neutron Scattering and NMR Studies," J. Phys.: Condens. Matter., in press.

Sokolov, A., "Dynamic Transition in Proteins and DNA: Role of the Solvent," in *Neutron and X-Ray Scattering as Probes of Multiscale Phenomena*, edited by Bhatia, S. R., Khalifah, P. G., Pochan, D. J., Radaelli, P. G., (Warrendale, PA), Mater. Res. Soc. Symp. Proc. **840**, Q2.5 (2005).

Sokolov, A. P., Gregory, R. B., "Internal Dynamics of Proteins and DNA: Analogy to Glass-Forming Systems," in *Neutrons in Biology-Techniques and Applications*, edited by Fitter, J., Gutberlet, T., Katsaras, J., (Springer Publishing), in press.

Soles, C. L., Douglas, J. F., Wu, W–L., "Dynamics of Thin Polymer Films: Recent Insights from Incoherent Neutron Scattering," J. Polym. Sci. B **42** (17), 3218 (2004).

Soles, C. L., Vogt, B. D., Jones, R. L., Prabhu, V. M., Wu, W.–L., Lin, E. K., Goldfarb, D. L., Angelopoulos, M., "Dynamics, Diffusion and Dissolution in Ultrathin Photoresist Films," in *Advances in Imaging Materials and Processes*," Proceedings of the 13th International Conference on Photopolymers, Mid-Hudson Section of Society of Plastics Engineers, (Brookfield, CT), p. 221 (2004).

Soriano, S., Dufour, C., Dumesnil, K., Borchers, J. A., Mangin, P., "Clamping Effects in the Al_2O_3(1120)/Nb(110)/Eu(110) Epitaxial System," Appl. Phys. Lett. **85** (20), 4636 (2004).

Soriano, S., Dumesnil, K., Dufour, C., Gourieux, T., Mangin, P., Borchers, J. A., Stunault, A., "Rotation of Magnetic Propagation Vectors Induced by Lattice Clamping in (110) Eu Films," Phys. Rev. B **71** 092409 (2005).

Soriano, S., Dumesnil, K., Dufour, C., Hennion, M., Borchers, J. A., Mangin, P., "Clamping Effect on the Magnetic Behavior of Europium Epitaxial Thin Films," J. Appl. Phys. **97**, 10K111 (2005).

Stancik, C. M., Lavoie, A. R., Achurra, P. A., Waymouth, R. M., Gast, A. P., "A Neutron Scattering Study of the Structure and Water Partitioning of Selectively Deuterated Copolymer Micelles," Langmuir **20** (21), 8975 (2004).

Stoltz, C., Ramesha, K., Piccoli, P., Toby, B. H., Eichhorn, B. W., "$A_{0.3}ZrNF_{1.3}$ Phases (A=Na, K) with Layered ZrNCl Type Structures by Anion Metathesis," Chem. Mater., in press.

Strzalka, J., Gibney, B. R., Satija, S., Blasie, J. K., "Specular Neutron Reflectivity and the Structure of Artificial Protein Maquettes Vectorially Oriented at Interfaces," Phys. Rev. E **70** (6), 061905 (2004).

Sturgeon, R. E., Willie, S. N., Yang, L., Greenberg, R., Spatz, R. O., Chen, Z., Scriver, C., Clancy, V., Lam, J. W., Thorrold, S., "Certification of a Fish Otolith Reference Material in Support of Quality Assurance for Trace Element Analysis," J. Analyt. Atomic Spectrom., in press.

Suescun, L., Jones, C. Y., Cardoso, C. A., Lynn, J. W., Toby, B. H., Araújo-Moreira, F. M., de Lima, O. F., Pardo, H., Mombrú, A. W., "Structural and Magnetic Study in $LaBaCoCuO_5$," Phys. Rev. B **71**, 144405 (2005).

Sung, L.-P., Vicini, S., Ho, D. L., Hedhli, L., Olmstead, C., Wood, K. A., "Effect of Microstructure of Fluorinated Acrylic Coatings on UV Degradation Testing," Polymer **45** (19), 6639 (2004).

Tang, F., Gnäupel-Herold, T., Prask, H. J., Anderson, I. E., "Residual Stresses and Stress Partitioning Measurements by Neutron Diffraction in Al/AlCuFe Composites," Mater. Sci. Eng. A. **399**, 99 (2005).

Tang, F., Anderson, I. E., Gnäupel-Herold, T., Prask, H. J., "Pure Al Matrix Composites Produced by Vacuum Hot Pressing: Tensile Properties and Strengthening Mechanisms," Mater. Sci. Eng. A **383**, 362 (2004).

Tang, F., Meeks, H., Spowart, J. E., Gnaeupel-Herold, T., Prask, H. J., Anderson, I., "Consolidation Effects on Tensile Properties of a Pure Al Matrix Composites," Mater. Sci. Eng. A, **386** (1-2), 192 (2004).

Thomas, J. J., Chen, J. J., Allen, A. J., Jennings, H. M., "Effects of Decalcification on the Microstructure and Surface Area of Cement and Tricalcium Silicate Pastes," Cem. Concr. Res. **34** (12), 2297 (2004).

Tian, J., Seery, T. A. P., Ho, D. L., Weiss, R. A., "Physically Crosslinked Alkyl Acrylamide Hydrogels: A SANS Analysis of the Microstructure," Macromol. **37**, 10001 (2004).

Toby, B. H., "The Classification of Powder Diffraction Data," in *International Tables for Crystallography, Volume G: Definition and Exchange of Crystallographic Data*, edited by Hall, S., McMahon, B. (IUCr, Springer), in press.

Toby, B. H., "Powder Dictionary," in *International Tables for Crystallography Volume G: Definition and Exchange of Crystallographic Data,* edited by Hall, S., McMahon, B. (IUCr, Springer), in press.

Toney, M. F., Borchers, J. A., O'Donovan, K. V., Majkrzak, C. F., Marguilies, D. T., Fullerton, E. E., "Magnetization Profile in Antiferromagnetically Coupled Magnetic Recording Media," App. Phys. Lett. **86**, 162506 (2005).

Tremsin, A. S., Feller, W. B., Downing, R. G., "Efficiency Optimization of Microchannel Plate (MCP) Neutron Imaging Detectors. I. Square Channels with ^{10}B Doping," Nucl. Instrum. Meth. Phys. Res. A **539**, 278 (2005).

Tremsin, A. S., Feller, W. B., Downing, R. G., Mildner, D. F. R., "The Efficiency of Thermal Neutron Detection and Collimation with Microchannel Plates of Square and Circular Geometry," IEEE Trans Nucl. Sci., in press.

Trouw, F., Martin, J. D., Goettler, S. J., Udovic, T. J., Iton, L. E., "Inelastic Neutron Scattering Study of the Trimethylammonium Templating Cations in the Crystalline and Vitreous States of the Sodalite-Type Copper-Zinc Chloride Halozeotype CZX-1," J. Phys. Chem. B, in press.

Vajda, P., André, G., Udovic, T. J., Erwin, R. W., Huang, Q., "Magnetic Structure of β-ErD_2: Long-Range and Short-Range Order from Powder Neutron Diffraction," Phys. Rev. B **71** (6), 054419 (2005).

Vajk, O. P., Kenzelmann, M., Lynn, J. W., Kim, S. B., Cheong, S.-W., "Magnetic Order and Spin Dynamics in Ferrolectric $HoMnO_3$," Phys. Rev. Lett. **94** (8), 087601 (2005).

van Duijn, J., Kim, K. H., Hur, N., Adroja, D., Adams, M. A., Huang, Q. Z., Jaime, M., Cheing, S. W., Broholm, C., Perring, T. G., "Inhomogeneous Level Splitting in $Pr_{2-x}Bi_xRu_2O_7$," Phys. Rev. Lett. **94**, 177201 (2005).

Voge, G., Fosser, K., Waldow, D., Briber, R. Halasa, A., "Effect of Random and Block R., Halasa, A., "Effect of Random and Block Copolymer Additives on a Homopolymer Blend Studied by Small-Angle Neutron Scattering," J. Polym. Sci. B **42** (17), 3191 (2004).

Vogt, B. D., Lee, H.-J., Prabhu, V. M., Delongchamp, D. M., Lin, E. K., Wu, W.-L., "X-Ray and Neutron Reflectivity Measurements of Moisture Transport Through Model Multilayered Barrier Films for Flexible Displays," J. Appl. Phys. **97**, 114509 (2005).

Vogt, B. D., Pai, R. A., Lee, H. J., Hedden, R. C., Soles, C. L., Wu, W. L., Lin, E. K., Bauer, B. J., Watkins, J. J., "Characterization of Ordered Mesoporous Silica Films Using Small- Angle Neutron Scattering and X-Ray Porosimetry," Chem. Mater. **17** (6), 1398 (2005).

Vogt, B. D., Prabhu, V. M., Soles, S. L., Satija, S. K., Lin, E. K., Wu, W. I, "Control of Moisture at Buried Polymer/ Alumina Interfaces Through Substrate Surface Modification," Langmuir **21**, 2460 (2005).

Vogt, B. D., Soles, C. L., Prabhu, V. M, Jones, R. L., Wu, W.-L., Lin, E. K., Goldfarb, D. L., Angelopoulos, M., "Measurements of Water Distribution in Thin Lithographic Films," Proc. SPIE Int. Soc. Opt. Eng. **5376**, 56 (2004).

Vogt, B. D., Soles, C. L., Wang, C.-Y., Prabhu, V. M., McGuiggen, V., Douglas, J. F., Lin, E. K., Wu, W.-L., Satija, S., Goldfarb, D. L., Angelopoulos, M., "Water Immersion of Model Photoresists: Interfacial Influence Concentration and Surface Morphology," J. Microlith. Microfab. Microsyst. **4** (1), 013003 (2005).

Wagner, N. J., Bender, J. W., "The Role of Nanoscale Forces in Colloid Dispersion Rheology," MRS Bull. **29** (2), 100 (2004).

Wakimoto, S., Lee, S.-H., Gehring, P. M., Birgeneau, R. J., Shirane, G., "Neutron Scattering Study of Soft Phonons and Diffuse Scattering in Insulating $La_{1.95}Sr_{0.05}O_4$," J. Phys. Soc. Jpn. **73** (12), 3413 (2004).

Wang, H., "Time resolved Small- Angle Neutron Scattering Study of Polyethylene Crystallization from Solution," J. Polym. Sci. B **42** (17), 3133 (2004).

Wang, H., Zhou, W., Ho, D. L., Winey, K. I., Fisher, J. E., Glinka, C. J., Hobbie, E. K., "Dispersing Single-Walled Carbon Nanotubes with Surfactants: A Small Angle Neutron Scattering Study," Nano Lett. **4** (9), 1789 (2004).

Was, G. S., Hash, M., Odette, R. G., "Hardening and Microstructure Evolution in Proton-Irradiated Model Commercial Pressure-Vessel Steels," Phil. Mag. **85** (4-7), 703 (2005).

Wiebe, C. R., Gardner, J. S., Kim, S.-J., Luke, G. M., Wills, A. S., Gaulin, B. D., Greedan, J. E., Swainson, I., Qiu, Y., Jones, C. Y., "Magnetic Ordering in the Spin-Ice Candidate Ho_2RuO_7," Phys. Rev. Lett. **93** (7), 076403 (2004).

Wietfeldt, F. E., Fisher, B. M., Trull., C., Jones, G. L., Collet, B., Goldin, L., Yerozolimsky, B. G., Wilson, R., Balshov, S., Mostovoy, Yu., Komives, A., Leuschner, M., Byrne, J., Bateman, F. B., Dewey, M. S., Nico, J. S., Thompson, A. K., "A Method for an Improved Measurement of the Electron-Antineutrino Correlation in Free Neutron Beta Decay," Nuc. Instrum. Meth. Phys. Res. A **545**, 181 (2005).

Wietfeldt, F. E., Gentile, T. R., "A New Method for Precision Cold Neutron Polarimetry Using ^3He Spin Filter," J. Res. Natl. Inst. Stand. Technol. **110**, 305 (2005).

Wietfeldt, F. E., Trull, C., Anderman, R., Bateman, F. B., Dewey, M. S., Komives, A., Thompson, A. K., Balashov, S., Mostovoy, Y., "A Backscatter-Suppressed Beta Spectrometer for Neutron Decay Studies," Nuc. Instrum. Meth. Phys. Res. A **538** (1-3), 574 (2005).

Wilson, S. D., Dai, P., Adroja, D. T., Lee, S. H., Chung, J. H., Lynn, J. W, Butch, N. P., Maple, M. B., " Quantum Critical Scaling and the Origin of Non- Fermi- Liquid Behavior in $Sc_{1-x}U_xPd_3$," Phys. Rev. Lett. **94** (5), 56402 (2005).

Wolff, M., Frick, B., Magerl, A., Zabel, H., "Flow Cell for Neutron Spectroscopy," Phys. Chem. Chem. Phys. **7**, 1262 (2005).

Wong-Ng, W., Huang, Q., Cook, L. P., Levin, I., Kaduk, J. A., Mighell, A. D., Suh, J., "Crystal Chemistry and Crystallography of the Aurivillius Phase $Bi_5AgNb_4O_{18}$," J. Solid State Chem. **177** (10), 3359 (2004).

Woodward, F. M., Lynn, J. W., Stone, M. B., Mahendiran, R., Schiffer, P., Mitchell, J. F., Argyriou, D. N., Chapon, L. C., "Field-Induced Avalanche to the Ferromagnetic State in the Phase-Separated Ground State of Manganites," Phys. Rev. B **70** (17), 174433 (2004).

Wu, H., Davies, P. K., "Non-Stoichiometric 1:2 Ordered Perovskites in the $Ba(Li_{1/4}Nb_{3/4})O_3$-$Ba(Li_{2/5}W_{3/5})O_3$ System," J. Solid State Chem. **177**, 3469 (2004).

Wu, H., Davies, P. K., "Ordered Perovskites in the $A^{2+}(Li_{1/4}Nb_{3/4})O_3$-$A^{2+}(Li_{2/5}W_{3/5})O_3$ (A^{2+} = Sr, Ca) Systems," J. Solid State Chem. **177**, 4305 (2004).

Wu, J., Lynn, J. W., Glinka, C. J., Burley, J., Zheng, H., Mitchell, J. F., Leighton, C., "Inter-Granular Giant Magnetoresistance in a Spontaneously Phase Separated Perovskite Oxide," Phys. Rev. Lett. **94** (3), 037201 (2005).

Wu, S., Huang, P., Tsao, F., Yang, C., Chung, M., Li, W.-H., Lynn, J. W., Liu, R., "Crystal Structure and Ferrimagnetism in $(La_{0.5}Ba_{0.5})(Mn_{0.5}Ru_{0.5})O_3$," J. Appl. Phys., in press.

Xu, B., Lynn, G. W., Guo, J., Melinchenko, Y. B., Wignall, G. D., McClain, J. B., DeSimone, J. M., Johnson, C. S., "NMR and SANS Studies of Aggregation and Microemulsion Formation by Phosphorus Fluorosurfactants in Liquid and Supercritical Carbon Dioxide," J. Phys. Chem. **109**, 10261 (2005).

Xu, G., Aeppli, G., Broholm, C., DiTusa, J. F., Ito, T., Oka, K., Takagi, H., "Mesoscopic Phase Coherence in a Quantum Spin Fluid," Nature, in press.

Xu, G., Gehring, P. M., Ghosh, V. J., Shirane, G., "High *q*-resolution Neutron Scattering Technique Using Triple-Axis Spectrometers," Acta. Crystallogr. A**60**, 598 (2004).

Xu, T., Hawker, C. J., Russell, T. P., "Interfacial Interaction Dependence of Microdomain Orientation in Diblock Copolymer Thin Films," Macromol. **38** (7), 2802 (2005).

Yamaura, K., Huang, Q., Moldovan, M., Young, D. P., Sato, A., Baba, Y., Nagai, T., Matsui, Y., Takayama-Muromachi, E., "High-Pressure Synthesis, Crystal Structure Determination, and a Ca Substitution Study of the Metallic Rhodium Oxide $NaRh_2O_4$," Chem. Mater. **17** (2), 359 (2005).

Yamaura, K., Huang, Q., Young, D. P., Takayama-Murmachi, E., "Crystal Structure and Magnetic Properties of the Trilayered Perovskite $Sr_4Rh_3O_{10}$: A New Member of the Strontium Rhodate Family," Chem. Mater. **16**, 3424 (2004).

Yang, X., Toby, B. H., Camblor, M. A., Lee, Y., Olson, D. H., "Propene Adsorption Sites in Zeolite ITQ-12: A Combined Synchrontron X-Ray and Neutron Diffraction Study," J. Phys. Chem. B **109**, 7849 (2005).

Yethiraj, M., Christen, D. K., Gapud, A. A., Paul, D. McK., Crowe, S., Dewhurst, C. D., Cubitt, R., Porcar, L., Gurevich, A., "Temperature and Field Dependence of the Flux-Line Lattice Symmetry in V_3Si," Phys. Rev. B., in press.

Yildirim, T., Ciraci, S., "Titanium- Decorated Carbon Nanotubes as a Potential High Capacity Hydrogen Storage Medium," Phys. Rev. Lett. **94**, 177501 (2005).

Yildirim, T., Íñiguez, J., Ciraci, S., "Molecular and Dissociative Adsorption of Multiple Hydrogen Molecules on Transition Metal Decorated C_{60}," Phys. Rev. B, in press.

Yim, H., Kent, M. S., Satija, S., Mendez, S., Balamurugan, S. S., Balamurugan, S., Lopez, G. P., "Study of the Conformational Change of Poly(N-Isopropylacrymide)-Grafted Chains in Water with Neutron Reflection: Molecular Weight Dependence at High Grafting Density," J. Polym. Sci. **42** (17), 3302 (2004).

Yoonessi, M., Toghiani, H., Daulton, T. L., Lin, J. S., Pittman, C. U., "Clay Determination in Clay/ Poly(Dicyclopentadiene) Nanocomposites Quantified by Small Angle Neutron Scattering and High- Resolution Transmission Electron Microscopy," Macromol. **38**, 818 (2005).

Youm, S. G., Sohn, D., Paeng, K., Choi, Y. W., Park, S., Seo, Y. S., Satija, S. K., Kim, B. G., Kim, S., Park, S. Y., "Supramolecular Ordering of Tripod Dyes at the Air/ Water Interface," Langmuir **21** (13), 5647 (2005).

Yue, A. F., Papandrew, A. B., Delaire, O., Fultz, B., Chowdhuri, Z., Dimeo, R. M., Neumann, D. A., "Vibrations of Micro- eV Energies in Nanocrystalline Microstructures," Phys. Rev. Lett. **93** (20), 205501 (2004).

Yue, B., Huang, C.-Y., Nieh, M.–P., Glinka, C. J., Katsaras, J., "Highly Stable Phospholipid Unilamellar Vesicles from Spontaneous Vesiculation: A DLS and SANS Study," J. Phys. Chem. B **109** (1), 609 (2005).

Yue, B., Huang, C.-Y, Nieh, M.–P., Glinka, C. J., Katasaras, J., "Spontaneously Forming Unilamellar Phospholipid Vesicles," Macromol. Symp. **219**, 123 (2005).

Yurekli, K., Krishnamoorti, R., "Thermodynamic Interactions in Blends of Poly(4Tert-butyl-styrene) and Polyisoprene by Small Angle Neutron Scattering," J. Polym. Sci. B **42** (17), 3204 (2004).

Yurekli, K., Mitchell, C. A., Krishnamoorti, R., "Small Angle Neutron Scattering from Surfactant Assisted Aqueous Dispersions of Carbon Nanotubes," J. Am. Chem. Soc. **126**, 9902 (2004).

Zaliznyak, I. A., Lee, S.-H., "Magnetic Neutron Scattering," Chapter 1, in *Modern Techniques for: Characterizing Magnetic Materials*, edited by Zhu, Y. (Springer, Heidelberg, New York), p. 3 (2004).

Zawisza, I., Burgess, I., Szymanski, G., Lipkowski, J., Majewski, J., Satija, S., "Electrochemical, Neutron Reflectivity and *in Situ* PM-FT-IRRAS Studies of a Monolayer of *n*-octadecanol at a Au (111) Electrode Surface," Electrochimica Acta **49** (22-23), 3651 (2004).

Zeisler, R., Clark, S. B., Parry, S. J., Chai Zhifang, Choppin, G. R., Danesi, P. R., Heller, Zeisler, S. F., Rossbach, M., Williamson, C., "Manpower Requirements and Education in Nuclear Science: An International Perspective," J. Radioanal. Nucl. Chem. **263** (1), 103 (2005).

Zeisler, R., Greenberg, R. R., "The Use of INAA in the Development and Certification of NIST SRMs," *Proceedings of the International Symposium on Research Reactor and Neutron Science*, (April, 2005, Daejeon, Korea), p. 338 (2005).

Zeisler, R., Lindstrom, R. M., Greenberg, R. R., "Instrumental Neutron Activation Analysis; A Valuable Link in Chemical Metrology," J. Radioanal. Nucl. Chem. **263** (2), 315 (2005).

Zhao, L., Robinson, L., Paul R. L., Greenberg, R. R., Miao, S., "Determination of Carbon, Nitrogen, and Phosphorus in Cattail (Typha Latifolia) by Cold Neutron Prompt Gamma Activation Analysis," J. Radioanal. Nucl. Chem. **263** (3), 805 (2005).

Zhou, J., Deyhim, A., Krueger, S., Gregurick, S. K., "LORES: Low Resolution Shape Program for the Calculation of Small-Angle Scattering Profiles for Biological Macromolecules in Solution," Comp. Phys. Comm., in press.

Instruments and Contacts

HIGH RESOLUTION POWDER DIFFRACTOMETER (BT-1):

J.K. Stalick, (301) 975-6223, *judith.stalick@nist.gov*

Q.Z. Huang, (301) 975-6164, *qing@nist.gov*

B.H. Toby, (301) 975-4297, *brian.toby@nist.gov*

DARTS, RESIDUAL STRESS AND TEXTURE DIFFRACTOMETER (BT-8):

T. Gnaeupel-Herold, (301) 975-5380, *tg-h@nist.gov*

V. Luzin, (301) 975-5303, *luzin@nist.gov*

30-M SANS INSTRUMENT (NG-7):

L. Porcar, (301) 975-5049, *lionel.porcar@nist.gov*

P.D. Butler, (301) 975-2028, *butler@nist.gov*

J.G. Barker, (301) 975-6732, *john.barker@nist.gov*

J. Krzywon, (301) 975-6650, *jeffery.krzywon@nist.gov*

30-M SANS INSTRUMENT (NG-3) (CHRNS):

B. Hammouda, (301) 975-3961, *hammouda@nist.gov*

S.R. Kline, (301) 975-6243, *steven.kline@nist.gov*

D. Ho, (301) 975-6422, *derek.ho@nist.gov*

B. Greenwald, (301) 975-5797, *bryan.greenwald@nist.gov*

USANS, PERFECT CRYSTAL SANS (BT-5) (CHRNS):

J.G. Barker, (301) 975-6732, *john.barker@nist.gov*

M.-H. Kim, (301) 975-6469, *man-ho.kim@nist.gov*

P.D. Butler, (301) 975-2028, *butler@nist.gov*

COLD NEUTRON REFLECTOMETER-VERTICAL SAMPLE-POLARIZED BEAM OPTION (NG-1):

C.F. Majkrzak, (301) 975-5251, *cmajkrzak@nist.gov*

J.A. Dura, (301) 975-6251, *jdura@nist.gov*

ADVANCED NEUTRON DIFFRACTOMETER/ REFLECTOMETER (NG-1):

U. Perez-Salas, (301) 975-8395, *ula@nist.gov*

K. O'Donovan, (301) 975-8380, *kevin.odonovan@nist.gov*

COLD NEUTRON REFLECTOMETER-HORIZONTAL SAMPLE (NG-7):

S.K. Satija, (301) 975-5250, *satija@nist.gov*

S. Basu, (301) 975-5192, *saibal.basu@nist.gov*

DOUBLE-FOCUSING TRIPLE-AXIS SPECTROMETER (BT-7):

Y. Chen, (301) 975-6442, *ying.chen@nist.gov*

J.W. Lynn, (301) 975-6246, *jeff.lynn@nist.gov*

TRIPLE-AXIS SPECTROMETER (BT-9):

W. Ratcliff, (301) 975-4316, *william.ratcliff@nist.gov*

R.W. Erwin, (301) 975-6245, *rerwin@nist.gov*

J.W. Lynn, (301) 975-6246, *jeff.lynn@nist.gov*

SPINS, SPIN-POLARIZED TRIPLE-AXIS SPECTROMETER (NG-5) (CHRNS):

J.-H. Chung, (301) 975-8369, *jae-ho.chung @nist.gov*

H.-J. Kang, (301) 975-4863, *hye.kang@nist.gov*

FANS, FILTER-ANALYZER NEUTRON SPECTROMETER (BT-4):

T.J. Udovic, (301) 975-6241, *udovic@nist.gov*

J. Leao, (301) 975-8867, *juscelino.leao@nist.gov*

DCS, DISK-CHOPPER TIME-OF-FLIGHT SPECTROMETER (NG-4) (CHRNS):

J.R.D. Copley, (301) 975-5133, *jcopley@nist.gov*

Y. Qiu, (301) 975-3274, *yiming.qiu@nist.gov*

C.M. Brown, (301) 975-5134, *craig.brown@nist.gov*

HFBS, HIGH-FLUX BACKSCATTERING SPECTROMETER (NG-2) (CHRNS):

E. Mamontov, (301) 975-6232, *mamontov@nist.gov*

V. Garcia Sakai, (301) 975-4404, *vicky@nist.gov*

NSE, NEUTRON SPIN ECHO SPECTROMETER (NG-5) (CHRNS):

A. Faraone (301) 975-5254, *antonio.faraone@nist.gov*

PROMPT-GAMMA NEUTRON ACTIVATION ANALYSIS (NG-7):

R.M. Lindstrom, (301) 975-6281, *dick.lindstrom@nist.gov*

R.L. Paul, (301) 975-6287, *rpaul@nist.gov*

THERMAL NEUTRON PROMPT-GAMMA ACTIVATION ANALYSIS (VT-5):

E.A. Mackey, (301) 975-5149, *liz.mackey@nist.gov*

OTHER ACTIVATION ANALYSIS FACILITIES:

R.R. Greenberg, (301) 975-6285, *rgreenberg@nist.gov*

COLD NEUTRON DEPTH PROFILING (NG-0):

G. Downing, (301) 975-3782, *gregory.downing@nist.gov*

NEUTRON INTERFEROMETER (NG-7):

M. Arif, (301) 975-6303, *muhammad.arif@nist.gov*

D. Jacobson, (301) 975-6207, *jacobson@nist.gov*

NEUTRON IMAGING FACILITY (BT-2):

M. Arif, (301) 975-6303, *muhammad.arif@nist.gov*

D. Jacobson, (301) 975-6207, *jacobson@nist.gov*

FUNDAMENTAL NEUTRON PHYSICS STATION (NG-6):

NG-6M: M.S. Dewey, (301) 975-4843, *mdewey@nist.gov*

NG-6U: H.P. Mumm, (301) 975-8355, *pieter.mumm@nist.gov*

NG-6: J. Nico, (301) 975-4663, *nico@nist.gov*

THEORY AND MODELING:

T. Yildirim, (301) 975-6228, *taner@nist.gov*

N.F. Berk, (301) 975-6224, *nfb@nist.gov*

SAMPLE ENVIRONMENT:

J. Leao, (301) 975-8867, *juscelino.leao@nist.gov*

D.C. Dender, (301) 975-6225, *dender@nist.gov*

NIST CENTER FOR NEUTRON RESEARCH

For copies of or information on this report, contact:

Ronald L. Cappelletti
301-975-6221
ron.cappelletti@nist.gov

For additional information on the facility, contact:

Patrick D. Gallagher
301-975-6210
patrick.gallagher@nist.gov

Dan A. Neumann
301-975-5252
dan.neumann@nist.gov

To obtain guidelines for preparing proposals to conduct research at the facility, contact:

William A. Kamitakahara
301-975-6878
william.kamitakahara@nist.gov

Location of all contacts:

NIST Center for Neutron Research
National Institute of Standards and Technology
100 Bureau Drive, Mail Stop 8562
Gaithersburg, MD 20899

Copies of this report and other information are available electronically. Please visit our website.

www.ncnr.nist.gov

NIST CENTER FOR NEUTRON RESEARCH
National Institute of Standards and Technology
100 Bureau Drive, MS 8562
Gaithersburg, MD 20899-8562

www.ncnr.nist.gov/

NIST
National Institute of Standards and Technology
Technology Administration, U.S. Department of Commerce